MICRO-ENVIRONMENTAL CHARACTERISTICS OF SERPENTINITE-HOSTED HABITATS: IMPLICATIONS FOR MICROBIAL ECOLOGY AND LIFE DETECTION

By

Osama M. Alian

A DISSERTATION

Submitted to
Michigan State University
in partial fulfillment of the requirements
for the degree of

Microbiology and Molecular Genetics – Doctor of Philosophy

2024

ABSTRACT

Microbial communities inhabit spaces in soils and rock from the surface extending deep into Earth. Though these environments seem homogeneous, they record inherent complexity in the system, incorporating hydrology, mineralogy, biology, and ecological succession. A challenge to understanding rock-hosted microbial ecosystems is describing this complexity and its relationship to resident microbial communities. Highly sensitive tools have been developed over the past decade to describe the physical and biogeochemical environment in rock pore spaces, as well as microbes and their functions in natural ecosystems. This is key for microbes in extreme environments that are can't be studied in pure culture. Rock-hosted habitats associated with serpentinization, the aqueous alteration of ultramafic rock, are an exciting avenue to explore as they've been present throughout Earth's history, are abundant in the solar system, and create energy and organic molecules that may fuel microbial growth.

Chapter 2 describes the subsampling and molecular, biological and mineralogical analyses of a large hydrothermal vent chimney structure from the Lost City Hydrothermal Field (LCHF) near the Mid-Atlantic Ridge. LCHF is strongly influenced by serpentinization, resulting in high pH, methane and hydrogen rich fluids. Although the chimney structures contain three minerals, aragonite, brucite and calcite, their distribution provided highlight which parts of the structure were directly in contact with alkaline hydrothermal fluids. Using these minerals as proxies for discrete hydrothermal regions, correlations were drawn between microbes, genes and minerals, making a coarse map of the domains of taxa and their metabolisms across a complicated marine extreme environment.

In chapter 3, LCHF chimneys samples were embedded in resin and sectioned for multi-modal analyses using Raman microspectroscopy, laser-ablation ICP-MS, and fluorescence

confocal microscopy. This localized relationships between microbial biofilms, pore spaces, and the microenvironment. We identified an abundance of microbial biofilms in brucite-lined pore channels, indicating contact with and adaptation to vent fluids. Further, the work showed that these channels were enriched in trace metals near biofilms critical to metabolism in chimney structures. Microscopy complemented by metagenomic analyses of biofilms showed active metal cycling pathways responsive to nearby metals with a possible biotic mechanism for their deposition through efflux systems.

Chapter 4 looked at a different type of serpentinite-hosted ecosystem within an ophiolite complex in Northern California. Forming in the Earth's upper mantle, ultramafic ophiolites are enriched in heavy metals such as Ni, Cr, and Co. Here, metal toxicity rather than limitation plays a key role in the ecosystem's organization. As these rocks weather into serpentine soils they host unique endemic fauna. The trace metal content of groundwater, rocks, and soils were compared to the diversity and function of microbial populations. Analysis showed Ni, Cr, and Co increase with depth, and high concentrations of Ni and Cr in high pH groundwater. Examining amplicon sequence data showed no correlations to Ni, Cr or Co but an adapted community overall. Analysis of metagenomic and metatranscriptomic data showed metal efflux systems abundant within the system. These data point to the adaptation of serpentinite-hosted microbiota to Ni and Cr rich environments, and additional resource demands imposed by this stressor.

This work provides important knowledge necessary to better understand micro-habitats in rock-hosted environments influenced by serpentinization. These data help to illuminate the microbial ecology of modern-day ecosystems and may guide future cultivation efforts while at same time providing an important point of comparison to models of the early evolution of life on Earth in places like the LCHF, and the potential for life elsewhere.

To Sofia, Adam and Jasmine – not the secrets of the universe nor the treasures of the Earth could replace the love you've given me through this beautiful challenge.

ACKNOWLEDGEMENTS

This work was carried out with the support and guidance of a village spanning the globe. Dr. Matt Schrenk, I cannot thank you enough, from the bottom of my heart. My PhD has endured a pandemic, expeditions to sea and countless travels that were made possible by your support and a fervent push to go beyond my comfort zones, intellectually and professionally. I'm grateful beyond words at the freedom you've given me to explore my scientific curiosities and develop the confidence to pursue them, and the incredible and consistent kindness you've shown when life happens. You exemplify good mentorship, and excellent humanity and I sincerely thank you. Ms. Heather Miller, Dr. Lindsay Putman, Ms. Katie Quinlan, Ms. Nicole Smith, Ms. Amy Vodopyanov, Ms. Maria Berry, Ms. Leah Knoor, Ms. Ella Cardoza, Mr. Dylan Mankel, Ms. Mio Hogan, Ms. Césarine Graham, and Ms. Sarah Gonzalez – you made the lab a wonderful place to be at all hours of the day, and it was not just a place to work but also a place I looked forward to being and having all manner of conversations, laughs and lots of coffee. You've taught me how to be a good lab mate, a better student and a better teacher and I'll carry our lessons and endless jokes with me onto the next adventure.

I would like to extend a thank you to the Lost City team, Dr. William Brazelton, Dr. Susan Lang, and Dr. Karmina Aquino for a constant stream of lessons and ideas from those who know these sites best. Truly, the shoulders of giants and it was a privilege to sail and work with you and catch the oceanography and Lost City bug. A special thank you to Dr. Alexis Templeton, Mr. Eric Ellison and Ms. Jessica Hankins for spending an ungodly amount of time over many years helping me workout technical curiosities and teaching me hands on Raman spectroscopy and theory. An extra thank you goes out to the Q-BEAM team at MSU, Dr. Tom O'Halloran, Dr. Keith MacRenaris, Dr. Aaron Sue and Dr. Soo Ahn for allowing me the space to

try unproven things with expensive machines and I look forward to the future work we'll continue to do together.

Thanks to the doctors and friends that preceded me through grad school and the ones that continue their journey, Dr. Hunter Dulay, Dr. Kati Ford, Dr. Sebastian Krause, Dr. Aiko Turmo, Dr. Kristin Jacob, Dr. Rachel Harris, Dr. Kristin Yoshimura, Ms. Alexi Schnur, Ms. Kirsten Fentzke, Mr. Keyi Cheng, Mr. Alex Aaring and Mr. Aaron Mau – our regular coffee and tea hours, conversations, intersections around the world, and laughs kept me level headed throughout our time together and I'm grateful that even though our friendships span oceans and continents, we continue this adventure unperturbed by distance or time.

No thank you will ever suffice for my family, my dad Dr. Mohammad Alian, my mom Mrs. Samia Hegazi – you've always believed in me even when I didn't and your sacrifices have never gone unnoticed. Thank you for your encouragement, your trust, your support and most importantly your unconditional love.

To everyone, the most sincere and deepest thank you.

TABLE OF CONTENTS

CHAPTER 1 – INTRODUCTION

While much of the biosphere we are familiar with on the surface of Earth occurs over a relatively narrow temperature range, with primary productivity and energy directly or indirectly fueled by photosynthesis, a significant portion of Earth's biodiversity exists outside these conditions in what are considered extreme environments. Microbial activities test our understanding of "normal" and occur over broad ranges of temperature, pressure, salinity, and many other factors (*1*). These extreme environments provide information about biological versatility, and clues to the evolution and adaptation of organisms over geologic time and have been a focus of diverse studies since the earliest evidence of extremophiles were noted.

Several central challenges limit the growth of organisms in any environment, including access to raw materials, liquid water, energy, and the biochemical machinery to carry out necessary reactions over a prescribed set of conditions (*1*, *2*). As a result, organisms have evolved the capacity to acquire and concentrate environmental materials such as N_2, NH_3, dissolved inorganic and recalcitrant carbon, phosphorous, and trace metals. Organisms have evolved to harness energy by both mediating chemical red-ox reactions, or from solar radiation using photosynthetic light-harvesting pigments. As other examples, microbes have evolved to change the fluidity of their cell membranes, enhance the stability of critical biomolecules, or produce compatible cytoplasmic solutes to adapt to the environmental extremes that they encounter (*3*). Some studies have argued that access to sufficient energy flux is necessary to invest in these adaptations, such as biomolecular repair and material acquisition, which help to prevent the instability of biological structures and biochemical processes (*4*). These descriptions are further clouded by ongoing evolution, and the propensity of microorganisms to horizontally exchange genetic elements between lineages, making their origin and evolutionary history

difficult to piece together (*5*). Loss factors may also play a role in extreme environments, including transport away from optimal niches, cell death, predation, and viral lysis, and countless other processes that function over large timescales.

In the past two decades, studies on Earth have expanded our understanding of the breadth and depth of the biosphere, uncovering subterranean habitats at least 4 km beneath the continents and 2 km beneath the seafloor rife with microbes (*6*). In parallel, investigations of Mars and icy Ocean Worlds of the outer solar system have indicated the presence of liquid water in subsurface environments or hydrothermal plumes actively venting into space highlighting the possibility that these planets and moons may also be habitable (*7–9*). Prominent in both scenarios are a series of water-rock reactions known as serpentinization, which involves the aqueous alteration of primitive, iron-rich minerals (mafic and ultramafic rocks) characteristic of the Earth's mantle as well as undifferentiated materials in the outer solar system, and possibly beyond (*10*, *11*). Indeed, on Earth serpentinization has been shown to support life in 1 km deep groundwater in ancient oceanic crust in Oman , in mud volcanoes originating from >10 km depth in the Mariana forearc, and in exhumed mantle material along the Mid-Atlantic Ridge (*12–15*). Particularly important for the purposes of this work is the potential role that serpentinization and the possibility of abiotic organosynthesis played in the origins and early evolution of life, providing the minerals and reactive substrates necessary for prebiotic chemistry to take shape (*16*). The mineral products of serpentinization have been identified on the surface of Mars and have been proposed to be capable of supporting life in aquifers beneath the Martian surface (*17*, *18*). The fluid chemistry of the subsurface ocean on Saturn's moon Enceladus has also been proposed to be alkaline and hydrogen and methane-rich, associated with pervasive serpentinization and hydrothermal activity as measured by the Cassini probe fly-by (*19*, *20*).

As described above, to understand the full range of the biosphere on Earth, both now and in the past, and the potential for life elsewhere, it is critical to understand the constraints imposed by serpentinization. Central among these considerations are hyperalkaline pH values, commonly in excess of 12 and in some cases approaching 13 that create unique ultrabasic environments worldwide (*21*). The high pH imposes challenges related to maintaining a proton motive force to drive the electron transport chain and affects the stability of biological macromolecules such as RNA (*22*). A less obvious consequence of high pH, in combination with the divalent cations released through serpentinization is the near complete mineralization of dissolved inorganic carbon into different carbonate minerals forming under different combined temperature and pH regimes. As an adaptation to DIC limitation, microorganisms have been putatively shown to mobilize solid carbonate forms or to use alternative carbon sources such as formate and methane, found in serpentinizing environments (*23*, *24*). Finally, serpentinization generally leads to highly reducing conditions, depleted in oxidants. The presence of copious fuels (e.g., H_2, CH_4, formate) and low oxidant concentrations may limit the energy available for both growth and adaptation to environmental extremes. One topic that has not yet been considered is the role that trace metals may play in serpentinizing systems, as they are critical for many origins-of-life models, and anaerobes generally have high soluble trace metal demands (*25, 26*). Trace metals are generally poorly soluble in alkaline solutions, but at the same time ultramafic rocks and their weathering products (e.g., soils) may be highly enriched in different heavy metals. This thesis explores the continuum of relationships between metal demands and abundance in marine and terrestrial serpentinizing habitats.

While the description above highlights the broad range of conditions that encompass the biosphere, it does not dissect the key differences between laboratory and field studies. For

example, while some parameters like temperature and pressure propagate relatively evenly through environmental matrices, others, such as porosity, solutes, energy, and elemental distributions may vary at microscopic scales. This is particularly important for rock-hosted environments associated with serpentinization, as the parent ultramafic rocks have very low permeability, with volume expansion during serpentinization contributing to fracturing and the formation of flow paths (*27*). At the same time, mixing of cation rich high pH fluids with dissolved inorganic carbon (DIC) mineralizes fractures with carbonate minerals and cuts off permeability as flow paths are backfilled with precipitation products. Dynamics in the environment also influence conditions in space and time and therefore contribute environmental stress that leads to adaptive strategies, such as the accumulation of energy storage molecules or the strategic formation of biofilms described below. In the laboratory, this heterogeneity is largely ameliorated in the test tube, through shaking incubation, and by targeting the exponential phase of growth usually with well-studied model microorganisms amenable to culturing. However, in nature this may manifest as habitable microenvironments within a largely inhospitable macro-system. One example of this are brine pockets that form within sea ice that allow water to remain liquid well below 0°C, and that concentrate organic compounds and nutrients as the ice freezes, where microbes are found attached to solid inclusions such as detritus or precipitates (*28, 29*). Fractures within weathering oceanic crust or in bedrock can localize biofilm formation in areas of relatively high permeability while enabling access to compounds in the underlying rock (*30*). Another example are the close relationships within microbial consortia necessary to degrade recalcitrant compounds that may be bioenergetically challenging. The sulfate-methane transition zone (SMTZ) in marine sediments is one such well-studied example of where syntrophic relationships between sulfate reducing bacteria and methanotrophic archaea

are believed to facilitate the energetically unfavorable reaction of anaerobic methane oxidation (*31–34*). Microbes have also been shown to metabolically divide labor, even in the tricarboxylic acid (TCA) cycle where cooperativity amongst individuals contributing to the whole of the cycle decreases individual cellular energy costs but requires close physical associations for metabolite and nutrient transfer in order for the cycle to be complete and resources shared amongst the group (*35, 36*). Microbes have also been shown to directly participate in the transfer of electrons either between individuals or between minerals using "conductive" pili (*37–40*). These examples accentuate the need to understand conditions at the scale of individual microbial cells, whose growth and survival may be dictated by access to local resources or protection against environmental stressors.

Several tools have been developed in recent years to study the variability and distribution of individual microbial cells under carefully controlled conditions. Techniques involving metabolic labeling with either radio- or stable isotopes, or using amino acid analogs and click chemistry have been used to pinpoint the activity of individuals within a community. At the same time tools such as embedding and Focused Ion Milling (FIM), Nanoscale Secondary Ion Mass Spectrometry (nano-SIMS), and High-Resolution Transmission Electron Microscopy (HR-TEM) have been used to describe micro-environmental distributions at exceptionally high resolution. Synchrotron-based approaches such as Scanning Transmission X-ray Microscopy (STXM) and X-ray Absorption Near Edge Spectroscopy (XANES) have allowed researchers to examine the oxidation state of metals and their relationship to biological structures (*41–43*). A particular challenge continues to be merging biological and geochemical approaches with appropriate sample handling and scales of resolution, while maintaining accuracy and replicability. This challenge has spurred the development of multi-modal imaging approaches that can be used to

generate co-registered biological and geochemical data sets. This serves to reconcile what is understood from controlled benchtop experiments with what is observed *in situ*, identifying features or patterns that are either difficult to reproduce in the lab environment or technically challenging to measure due to technical limitations. Often, the best available methods, whether biological or geochemical, rely on bulk analyses which are biased towards large signals that are sufficiently distributed through the sample to allow for detection. These methods usually require extensive sample preparation and homogenization, which also destroys any spatial context to targets of interest, in addition to diluting any smaller possibly locally high signals into the larger sample.

In parallel, molecular biological approaches have also been refined to understand the complexity of microbial populations, even if in bulk, with breadth and depth. Enabled by high throughput sequencing techniques, shotgun metagenomic approaches has progressed from requiring large amounts of material to detecting the smallest genetic fingerprints for further study (*44–46*). Ultimately this is dictated by cell population sizes and DNA yield from the specific sample, which has also seen a larger blooming of optimization methods, and commercially available tools. The ability to use metagenomics and other high throughput approaches in natural systems has allowed for the circumvention of the canonical requirement for cultivation. One tool enabling this progress has been the use of multiple displacement amplification (MDA), which has allowed researchers to work with vanishingly small amounts of sample material. This has enabled the use of cell sorting with flow cytometry followed by single cell genomics and allowed for the discrimination and detailed analysis of distinct populations within complex microbial communities. The combination of different sequencing approaches has also enabled the reconstruction and comparison of distinct populations. For example, commonly used short read

sequencing approaches on the Illumina platform can be coupled to long read approaches with Nanopore or PacBio instruments to generate high quality genome reconstructions. Likewise, chromatin association mapping has enabled the reconstruction of distinct, closely related populations and genomic comparisons. A key challenge with all these approaches is the vast uncharted landscape of biodiversity that still exists in nature, often referred to as microbial dark matter, as well as the limitations of gene annotation, which are largely biased towards biomedical investigations. While we've been able to accumulate a vast environmental census of microbial populations and functions, much remains unknown about how they function both alone and in communities under different stress conditions and in a dynamic environment. The census is essentially a snapshot at time of sampling that has been analyzed after extensive processing and statistical filtering. Nonetheless, enormous recent advances in both direct imaging and genomics have changed our perspective on microbial ecology. It is likely that with the more widespread use of these tools, new innovations will emerge that further push the boundaries of our understanding.

Beyond adaptations at the sub-cellular level, microorganisms are physiological machines adapted to their external medium, enabling their success in diverse environments. The development of multi-cellular biofilms drastically alters the physical, chemical, and biological properties of the immediate environment with larger effects possible on global biogeochemical cycles (*47*). At the cost of increased investment of energy and raw materials, production of Extracellular Polymeric Substances (EPS) can influence the diffusion kinetics of molecular stressors such as antibiotics or oxygen radicals, and even immobilize toxic compounds extracellularly such as with trace metals (*48*, *49*). EPS also aid in anchoring organisms in favorable niches, such as the air-water interface, solid surfaces, or to remain static in the face of

intense advective forces or strong fluid flows (*50*, *51*). Multi-cellular biofilms may also facilitate cell-cell interactions that may further enable organisms to overcome energetic barriers via syntrophy or to share resources or in the case of conductive pili transferring electrons to distant electron acceptors, including solid substrates as previously described. Biofilms are also hotbeds of biological activity. Owing to the proximity of nearby cells, biofilms have been shown to sustain elevated rates of horizontal gene exchange that may allow the proliferation of traits like antibiotic or metal resistance throughout a community (*52*). The combination of evolutionary processes and physico-chemical gradients can also force the diversification of populations into different phenotypes within a biofilm which has been observed in the differentiation of susceptible and persistent populations in antibiotic resistant biofilms as well as the activity of populations of Shewanella in response to oxygen (*53*, *54*). This has even been observed in hydrothermal chimneys associated with serpentinization, where transposases account for a significant portion of the metagenome, and which host a multitude of variants of essential genes such as nitrogenase (*55*). While these examples provide insight into how biofilm formation impacts habitability, they are also valuable from the standpoint of life detection in extreme environments at the fringe of the biosphere. Multi-cellular aggregation may be easier to observe and distinguish from non-biological structures. Biofilm influences upon mineral weathering, precipitation, and elemental/isotopic distributions may all leave distinctive and robust signatures. An especially prominent example of this are the stromatolites/microbialites that serve as the first evidence of photosynthetic life in the fossil record (*56*). Across a wide range of habitats, the biofilm phenotype serves to expand habitable conditions, enhance survivability, and potentially enable life detection in diverse natural environments, particularly extreme environments of the biosphere.

Hydrothermal systems, where buoyant fluid heated by Earth's geothermal gradient, magmatic intrusions, water-rock reactions, or the decay of radiogenic elements provide chemical energy in the form of redox disequilibria that fuel chemolithoautotrophic microbial communities. Biological communities around hydrothermal vents are some of the most prolific on Earth, capable of rapid growth rates and large body sizes even in the absence of light, in stark contrast to much of the deep-sea (*57*). An enormous body of literature related to extremophiles and the limits of life has emerged from studies of hydrothermal fluid flow and plumes, vent macrofauna, and surface features such as biofilms (*58*). However, these fluids emerge from vent chimney structures and cracks in the seafloor which connect to a much larger potentially habitable biosphere. These features are not only prevalent in submarine environments but occur on the continents as well, where they manifest as geysers and springs, with Yellowstone National Park serving as a prominent example. These biospheres though considered extreme now, were likely much more common on Early Earth, where their temperature and redox gradients coupled with their reactive physical features are thought to have provided the convergence of factors for the earliest origin of life to take shape, ranging from RNA oligomerization to stand-alone metabolic cycles, amino acid, and membrane formation (*59–64*). This has made hydrothermal vents ripe systems for hypothesis testing and for understanding their potential in identifying habitability constraints and biosignatures for use in the hunt for life beyond Earth.

Serpentinization-influenced environments represent a distinct subset of hydrothermal systems, where the reactions between circulating water and reduced minerals in ultramafic rocks create highly reducing, hydrogen-rich, high pH chemistries. Exothermic heat from serpentinization may contribute to hydrothermal circulation in serpentinites, however geothermal gradients and/or cooling magmatic intrusions also play significant roles. The reducing conditions

and mineral catalysts associated with serpentinization have also been shown to facilitate the abiogenic synthesis of small organic compounds (*65–67*). These simple organic compounds can fuel subsurface microbial communities (*68*). At the same time, in contrast to magmatically-driven high temperature hydrothermal systems that produce the hallmark black smokers, serpentinization-influenced fluids are relatively metal-poor due to their insolubility at high pH.

In addition to representing some of the most extreme endmembers of the modern-day biosphere, serpentinization-associated environments were likely even more prevalent on the early Earth and may have contributed heavily to early biological evolution. One of several models of the origins and early evolution of life on Earth relies upon the model of microcompartments within hydrothermal vent chimneys that serve as an energetic divide driving the first metabolic systems. These models converge upon the fact that deeply branching organisms and the last universal common ancestor (LUCA) share traits with the organisms present in modern day hydrothermal systems (*69*). These models also speculate that metal adorned pore spaces within hydrothermal chimneys can serve as primitive barriers between the external and internal environments that can catalyze prebiotic reactions.

Beyond theories about the origins of life, the scant evidence of early life on Earth, prior to the advent of oxygenic photosynthesis, also converges upon the importance of hydrothermal systems. Putative microfossils in 3.5 Ga rocks from Western Australia preserve chemical and microscopic evidence of early life at a site interpreted to be a hydrothermal environment (*70*). Even further back into geologic history, iron sheaths and carbonate chemistry suggest early life associated with hydrothermal systems to 4.0 Ga (*71*). Modern systems remain dynamic and mineralizing and provide a window into how active microbial ecosystems could have been preserved in the geologic record. Hydrothermal vents near the Lost City represent active and

extinct vent structures dating to at least 120,000 years old (*72*, *73*). Some of the closest analogs to Lost City along the mid-ocean ridges are extinct systems such as Ghost City and Old City that preserve evidence of ancient hydrothermal ecosystems (*74–76*). On the continents active serpentine seeps exist in geologic settings as old as 480 million years before present, speaking to the longevity of these systems (*77*, *78*). As such, it is important to understand relationships between microbes and minerals in these ecosystems, including their impact upon elemental and isotopic distributions, to guide an accurate interpretation of these ancient Earth materials.

This work has several important implications for the interdisciplinary field of Astrobiology. Specifically, it addresses the adaptation of organisms to the myriad of habitats on Earth, particularly extreme environments that may be analogs to other planets and moons. Additionally, it considers habitability from a holistic perspective, incorporating not only commonly measured parameters like liquid water and energy, but also the availability and distribution of trace metals. Understanding the nuances of habitability may serve as an important guide for where best to look for life on other worlds and further constrain its definition to practical and realistic ranges. Finally, the detailed examination of microbe-mineral interactions, including those associated with biofilms, may help to understand the distinctive signatures of life that may originate in these systems, and potentially become preserved in the rock record. This is important both to interpreting microfossils from the early Earth, and for the exploration of extraterrestrial environments where similar minerals can be found and may still harbor evidence of life were it to have occurred beyond Earth.

Fully understanding how life functions and has evolved in serpentinizing hydrothermal systems is not only important to the biology of extant organisms, but to the possibility if life elsewhere in universe. Undifferentiated materials like the ultramafic rocks of Earth's mantle are

widespread on other planets, moons, and even asteroids of our solar system (*79*). These are the parent materials that on Earth, differentiated and evolved in continents and oceans. Evidence of serpentinization and serpentine minerals exists at and below the surface of Mars, where liquid water has existed in the past and may still be present today (*80–82*). Serpentinization is also predicted to influence the fluid chemistry of subsurface oceans on Saturn's moon Enceladus, based on evidence in cryovolcanic plumes ejected into its orbit, and has spurred greater interest in understanding the chemistry that can be detected using orbital remote-sensing or instruments making *in situ* measurements (*19*, *83*).

Although it is still a field of active study, there are several evolutionary adaptations that have been uncovered that describe how life has become well suited to serpentinizing ecosystems. From one perspective, it is important to understand the habitability of serpentinite-hosted environments on modern-day Earth to understand the limits of the biosphere. How does the balance of energy to facilitate biological structure and function play against the demands of the environment? Reduced compounds such as hydrogen and methane may be plentiful in serpentinizing environments, however oxidants to harness these fuels may be in vanishingly short supply. Microbes in serpentinites make use of these copious "geo-fuels" by coupling their oxidation to available electron donors such as intermediate sulfur compounds. When sulfur is unavailable, low energy metabolisms such as methanogenesis and acetogenesis become prevalent (*84*, *85*). Raw materials, including carbon, nitrogen, phosphorus, and trace metals may also be in short supply. While dissolved inorganic carbon in the form of the carbonate anion may be limiting, a variety of small organic compounds (e.g., methane, formate, acetate), some of which are produced through abiotic processes may be used instead. Prior studies have shown that CO_2 concentrating mechanisms are associated with high pH adaptation, and there is even

evidence that organisms are able to liberate carbon from the abundant carbonate mineral phases that are abundant in serpentinizing systems, although the mechanisms for this remain unclear (*23*, *86*). Nitrogen assimilation is similarly an important component of ecosystem function, and incredibly diverse nitrogenases exist even within taxonomically limited populations (*55*, *87*, *88*). Recent comparisons of serpentinizing systems have shown the importance of phosphorous scavenging strategies as a globally important feature of life in these environments (*89*). Trace metal distribution and availability has not yet explicitly been addressed in these ecosystems and the metabolic accounting of energy and input products may be an oversimplification of the natural system, which involves mineral interfaces, cell-cell interactions, fluid flow, and evolutionary processes and a dynamic interlinkage between all three. A holistic model of life in hydrothermal systems more generally, and serpentinites specifically is necessary to fully understand the habitability potential of these systems and the bridge between biogenic and abiogenic processes.

Considering physiological adaptations beyond food and energy are important for understanding survival in serpentinizing environments. A common observation across serpentinizing ecosystems is their incredibly low taxonomic diversity, sometimes consisting of only a few primary phylotypes (*23*, *55*, *90*). This low diversity is not only a characteristic of individual sites of serpentinization, but a global feature of microbial communities found at serpentinites overall. For example, a lineage of proteobacteria related to the Hydrogenophagales, called Serpentinomonas, is a widespread constituent of serpentinizing systems. As another example, the microbial communities of the Lost City Hydrothermal Field (LCHF) and Prony Hydrothermal Field are remarkably similar, despite their presence in different ocean basins (*91*). Studies of these systems are still ongoing and challenging due to the low number of cultivated

isolates. However there have been insights into how individuals and communities in these systems are specifically adapted to the hyperalkaline environments. For example, ion transporters, particularly those that use Ca^{2+} or Na^{+} are abundant and highly expressed in these systems and isolates of Serpentinomonas also possess archaeal V-type ATPases that enable their ability to generate energy at extremely high pH (*23*, *86*). As mentioned earlier, the challenges of low taxonomic diversity may be ameliorated by rampant gene exchange and functional and / or metabolic diversification and partnerships. A recent study of a groundwater well network in a serpentinizing aquifer of northern California showed that the combined effects of low dispersal and extreme conditions cancel each other out in terms of evolutionary diversification; similar observations have been made in a comparison of deep crustal rocks of the North American, Eurasian, and African continents (*92*, *93*). Maximum efficiency in the microbial world may be necessary in the face of minimal survival at the lowest cost. On geological timescales, this may be the norm rather than the exception.

Finally, studies of serpentinizing ecosystems are important as they bridge the divide between abiotic and biotic processes. Organosynthesis reactions may have fed the earliest life forms on Earth and may continue to be retained in serpentinite ecosystems to this day. However, to make these extraordinary connections it is critical the samples are examined with scrutiny and with consideration to the spatial context and heterogeneity that these dynamics rely upon. The ability to study biological processes in these systems provides an excellent challenge to life detection strategies looking for biosignatures. These approaches can be used to better understand the sparse record of biological processes on a poorly differentiated early Earth, and primitive or stalled systems on other planets and moons. Biofilms, formed within a rock matrix may be an especially useful target for this endeavor as they may develop into larger, potentially

recognizable morphologies. Microbial activities within biofilms may also serve to alter elemental or isotopic signature by modifying mineral substrates, or by catalyzing mineral nucleation. These effects may be recorded in the inorganic geochemical record, even well after the organic biomass has been consumed or degraded.

One critical challenge for astrobiological investigations, whether related to the early Earth or extraterrestrial systems, are access to samples. The few fossilized hydrothermal ecosystems that remain from Earth's Archean Eon are highly altered and contain little recognizable biomass. Likewise, while extraterrestrial sample return is important to NASA's overall mission and a driving force behind the contemporary Mars Sample Return program, remote sensing and analysis is much more likely, affordable and iterative in the short-term. Consequently, the analytical approaches that can be utilized with modern ecosystems in the laboratory setting will undoubtedly need to be adapted for usefulness in these complex strategic exploration objectives. However, they can provide perspective about where to look (habitability), what to look for (morphological and chemical biosignatures), and how to look (discriminating biotic from abiotic processes). The development of instrumentation and strategies for current and upcoming missions (e.g., Europa Clipper, Dragonfly, Rosalind Franklin Rover) should be carefully matched and tested against validated signatures of life. In addition to being astrobiology analogs, extreme environments provide an ideal testing ground for these approaches prior to launch. Further, interpretation of data streams stemming from space explorations has been and will continue to be an ongoing effort for decades to come. Therefore, insights provided by the study of extreme environments on Earth will continue to inform these studies well into the future.

Even on the modern-day Earth, the study of extreme environments has provided profound insights into the extent of the biosphere and the range of biological diversity. These records are important to understanding the co-evolution of Earth and life, but also the functioning of biochemical cycles, and novel biochemistries that may be useful in biotechnology. This begins with a holistic, biologically accurate accounting of habitability in these systems, like what has been accomplished for land plants and animals, or phytoplankton in the open ocean and underpinned much of our modern understanding of global cycles. Considering trace metal distributions is one aspect of habitability, but many more facets will ultimately need to be considered. Holistic models of habitability and niche space will be critical for better understanding Earth's microbiomes in a changing world, and the possibility for life elsewhere. Additionally, high resolution and complementary analytical approaches will be necessary to decipher the complexities of natural systems, particularly those at the fringes of the biosphere where biological and abiological processes meet. The search strategies used to query these spaces will also prove valuable in considering even more complicated and exciting spaces from the early Earth to beyond.

CHAPTER 2 - MICROBIAL COMMUNITY DIFFERENTIATION IN VENT CHIMNEYS OF THE LOST CITY HYDROTHERMAL FIELD REFLECTS HABITAT HETEROGENEITY

Abstract

Oceanic hydrothermal vent systems contain some of the oldest habitat types on Earth, while also serving as analogs for potential extraterrestrial environments. The Lost City Hydrothermal Field (LCHF) near the Mid-Atlantic Ridge is one such environment, unique in the superposition of heated hydrothermal fluids and the influence of water-rock reactions influenced by serpentinization. Microbial communities within LCHF have been studied for insights into their functional adaptations to the warm, alkaline, and dissolved inorganic carbon-limited environment. Metagenomic and mineralogical data collected during a recent expedition to Lost City was analyzed to document the associations between microbial populations and physical, chemical and biological characteristics of the hydrothermal vent chimney structures. Subsamples within the vent chimneys show distinct mineralogical compositions that correspond to specific physical-chemical conditions. Bacterial 16S rRNA gene sequences show a high degree of putative strain level microdiversity within the relatively dominant genera *Desulfotomaculum, Sulfurovum, Thiomicrorhabdus,* and the recently described *Serpentinicella*, which likely represent a large core of the overall LCHF vent bacterial community. This microdiversity relates to the compositional fraction of aragonite, brucite, and calcite minerals within chimney samples rather than the composition of nearby vent fluids. Chimney communities show little overlap with deep seawater, hydrothermal fluids, or previously analyzed subsurface core samples, demonstrating a highly specialized population in each habitat. Shotgun metagenomic analysis revealed that W/Mo uptake and metabolism to be the most highly sensitive to their environment

by their correlation with mineral proxies. These data hint at microenvironmental complexity missed by standard bulk analyses and indicative of discrete conditions at the interface between cells and chimney material. The findings of this study underscore the need to more closely examine microbe-mineral interactions in natural environments, critically informing not just population-level distributions but also the functional underpinnings of these carefully structured extremophile microbial communities.

Introduction

Deep-sea hydrothermal vents are some of the most dynamic environments in Earth's biosphere. These unique ecosystems form when energy-rich hydrothermal fluids, produced by processes beneath the seafloor, mix and react with cold, oxic seawater (*97*, *98*). Specific niches within hydrothermal vent habitats harbor some of harshest conditions known to support life, with extreme temperatures (>120°C), pressures (> 50 MPa) and pH (from 3-10) (*99*, *100*). Vent chimneys represent a distinctive habitat within marine hydrothermal ecosystems, serving as conduits for subsurface fluids to be released into the deep sea and as a rich source of energy in the form of chemical disequilibria (*101, 102*). The inhabitants of vent ecosystems redefine our understanding of biological resilience and the boundaries of habitability in extreme settings. Vent microbial communities often exhibit low taxonomic diversity, containing organisms with physiologies adapted to the physical-chemical conditions found at these sites (*103–106*). Within the porous walls of hydrothermal chimneys, stark thermal and chemical gradients similar to what is found in the subseafloor develop over distances as short as a few centimeters (*107*). Although the microbiological features of vent chimneys have been previously studied at larger scales, limited research has been conducted on the characteristics of small scale micro-environments within the chimney walls and how they influence microbial community structures and functions,

in part due to difficulty of sampling remote locations along the mid-ocean ridges, and challenges of downstream analysis (*108*). Prior studies have delineated microbial distributions at broad scales, highlighting differences between regions like the inner and outer portions of chimneys or between various vent environments. However, the nuanced distribution and abundance of these communities across microscopic regions with varying local conditions, such as along flow channels and pore spaces, remains to be fully understood (*109–111*).

Sulfide-hosted hydrothermal systems, driven by active magmatism, are among the best studied extreme environments since their discovery in the 1970s. These systems are teeming with uniquely adapted microbial and macrofaunal communities, some of which endure the highest temperatures known to life (*112–114*). A mixture of seawater derived nutrients and oxidants, combined with metals and volatiles from magmatic processes, sustain high microbial metabolic activity within these vibrant ecosystems (*37*, *115*). In contrast, hydrothermal systems influenced by serpentinization, a process whereby water reacts with ultramafic rocks of the upper mantle, are metal deficient, with scant dissolved inorganic carbon and high pH resulting from water-rock reactions (*100*). The carbonate structures at such sites, like those at the Lost City Hydrothermal Field, consist primarily of three minerals; aragonite ($CaCO_3$), brucite ($Mg(OH)_2$) and calcite ($CaCO_3$). These minerals form sequentially at specific temperature and pH ranges as the serpentinization-influenced fluids originating from the subsurface react with seawater (*116*, *117*). Studies of younger actively venting structures from LCHF indicate a major control of vent fluid and seawater mixing on the resulting mineralogy and geochemistry of the chimneys showing brucite-calcite as the preferred mineral assemblages precipitating from vent dominated solutions found in interior chimney structures, with limited seawater mixing (*118*, *119*). In contrast, the chimney exterior is a seawater dominated environment with primarily aragonite and secondary

calcite. These differences are further highlighted by stable isotopic signatures suggesting higher formation temperatures in the brucite-calcite regions and $^{87}Sr/^{86}Sr$ ratios in aragonite that are much closer to seawater than primary calcite. As venting significantly decreases and the chimneys become extinct, structures become dominated by much larger fractions of calcite infilling than either aragonite or brucite, a function of calcite being the most stable at the lowest temperatures at the site (*72*). Taken together, these minerals can be utilized as proxies for environmental conditions within chimney structures where brucite represents the hottest and youngest chimneys, aragonite appears with increasing seawater intrusion, and the largest calcite fractions indicates terminal stages as vents become extinct.

The fragile nature of the carbonate chimneys and difficulty culturing representative microbial populations have meant that much of our understanding of the LCHF chimneys is based upon observational analyses. The carbonate chimneys at LCHF host dense microbial populations, reaching 10^9 cells per gram, enrobed in extensive exopolymeric biofilms. Although the serpentinization-influenced hydrothermal fluids provide key energy sources such as methane, hydrogen and formate, they are generally depleted in oxidants to use these fuels. Additionally, serpentinizing environments are largely deficient in trace metals that may be critical to enzymatic functions (*85, 120*). The presence of dense microbial biofilms within the LCHF chimneys hint at sufficient trace metal concentrations to sustain metabolism in either the fluids or the carbonate matrix or an adaptation to utilize alternate metabolic cofactors.

Metal limitations can greatly impact microbial physiology and the functional organization of microbial communities. Metal cofactors are required for various metabolic processes, including methane and nitrogen cycling, and the most basic cell functions, such as electron transport. Metals are especially critical to key steps in anaerobic metabolism that under

thermophilic conditions can require nearly double (hundreds of ppm and ppb levels) the trace metal amounts for mesophilic conditions (*121*). Lost City vent fluids and carbonates contain generally lower metal concentrations than seawater, with higher levels found with increased seawater mixing (*100*). When analyzed at a bulk scale, chimney trace elements are generally below instrument detection levels or are at minimal concentrations depending on the element of interest (*100*). The concentrations of these metals can vary over time with changes in the underlying venting chemistry, influenced further by the temperature and pH variations that drive carbonate formation and elemental adsorption (*122, 123*). Marine microbes inhabit a wide range of metal-scarce environments and evolved various adaptive strategies for their sequestration, or using alternative cofactors altogether (*124–128*). These communities may also engage in cooperative strategies, including the concentration of different metal species and their extracellular efflux to nearby cells (*33, 129*). Effective utilization of these trace metals by microbes depends on the existence of localized microenvironments and mixing regions with enough energy and rate-limiting elements at the mineral-microbe interface (*130, 131*). Sharing of these resources might be part of a community strategy to overcome the limitations of individual cells.

Our understanding of carbonate chimney composition, formation, and evolution has advanced significantly in recent years, allowing for better geochemical constraints on chimney micro-environments. This study delves into the diversity and differentiation of microbial populations within the Lost City chimneys and how they relate to physical-chemical features and chimney evolution. We highlight how specific taxa and genes are distributed within the chimney structures using the key indicator minerals brucite, aragonite and calcite as proxies for localized conditions. Together, our findings point to the intricate interplay between geochemistry and

biochemistry within these structures, identifying small scale environmental characteristics that may influence the unique microbial community structure within the Lost City and define some of the key metabolic pathways prevalent in those differing communities.

Materials and Methods

Sample Collection

Hydrothermal chimney and fluid samples were collected using the R/V Atlantis and ROV Jason II during expedition AT42-01 in September and October 2018. Microbial cells in hydrothermal fluids and seawater were collected onto Sterivex 0.2 mm filtration cartridges (Millipore) with ROV Jason II or Niskin bottles mounted to a CTD rosette, as previously described (*85*, *132*). Ambient lab air samples were collected from the R/V *Atlantis* shipboard laboratory and at the University of Utah during chimney sample DNA extraction procedures, as has been reported in other studies (*85*, *132*). Chimney samples were collected by slurp sampling from the ROV or via grab sampling and placed in onboard boxes unique to each sample. Tools for sampling were sterilized by both autoclaving as well as flaming with 70% ethanol. Subsamples of various sizes and masses were collected from the primary larger samples shipboard and either stored in sterile Falcon tubes or sterile Whirlpaks to preserve sample integrity. Each individual sample is associated with a unique longform Jason dive ID to track associated parallel analyses performed. Collected samples were catalogued to record location information, depth, pH and temperature where measured and any collection notes during sampling. Samples destined for genomics work were immediately frozen at -80℃ on the ship and transferred by dry ice to the University of Utah for DNA extraction.

X-ray Diffraction Mineralogy Analysis

The mineralogy of the samples was determined using a Bruker AXS D8 Advance Powder X-ray Diffractomer (Bruker Corporation, Billerica, USA) at the Institute of Geochemistry and Petrology, ETH Zurich. The XRD was equipped with a LynxEye detector and a CuKα source. The analyses were carried out using a scan range of 5-90° 2θ, a step size of 0.02, and a scan time of 0.8 seconds per step. The mineral phases were identified using the ICDD PDF-2 database (International Center for Diffraction Data, USA) and the ICDD Sieve+ automatic peak search software. Weight proportions of the identified minerals were obtained using a full-profile Rietveld refinement method via Siroquant version 3.0 (Seitronics, Australia). Detailed mineralogical studies were carried out by Aquino et al. and can be found here (*133, 134*)

DNA Extraction and Sequencing

Extractions of DNA from chimney biofilm samples were conducted with the FastDNA SPIN kit (MP Biomedical) according to the manufacturer's instructions, followed by washing in Amicon Ultra (Millipore) filter units with 65ºC Tris-EDTA buffer. Extractions of DNA from hydrothermal fluid samples and seawater samples were conducted as described previously (*85, 132*) and the full extraction protocol is available on protocols.io (DOI: dx.doi.org/10.17504/protocols.io.bykqpuvw). All DNA preparations were purified with magnetic beads prior to sequencing (*135*).

Sequencing of 16S rRNA gene amplicons was conducted by the Michigan State University genomics core facility. The V4 region of the 16S rRNA gene was amplified with universal dual-indexed Illumina fusion primers (515F/806R) as described elsewhere (12). Amplicon concentrations were normalized and pooled using an Invitrogen SequalPrep DNA Normalization Plate. After library quality control (QC) and quantitation, the pool was loaded on

an Illumina MiSeq v2 flow cell and sequenced using a standard 500 cycle reagent kit. Base calling was performed by Illumina Real Time Analysis (RTA) software v1.18.54. Output of RTA was demultiplexed and converted to FASTq files using Illumina Bcl2fastq v1.8.4.

Chimney biofilm metagenome libraries were constructed with size-selected, sonicated DNA fragments of 500-700 bp with the NEBnext Ultra DNA II library kit for Illumina (E7645S). Paired-end sequencing (2 × 150 bp) of metagenomic libraries was conducted at the University of Utah High-Throughput Genomics Core Facility at the Huntsman Cancer Institute with an Illumina NovaSeq 6000 platform.

Metagenomic sequencing assembly and annotation

Metagenomic analyses were conducted as described previously for a similar study (*85*) and summarized here. Adapters and low-quality bases were removed from metagenomes with bbduk and seq-qc (*136*, *137*). A pooled, co-assembly of all 16 chimney biofilm metagenomes was conducted with Megahit v1.1.1 (*138*). Genes were predicted with Prodigal v2.6.3 in meta mode (*139*). Predicted protein sequences were queried against the KEGG release 83.2 prokaryotes database with Diamond v0.9.14 (*140*). Unassembled sequences were mapped to the pooled Megahit assembly with Bowtie2 v2.3.2 (*141*). Binning of metagenome-assembled genomes (MAGs) from the pooled assembly was conducted with BinSanity using the Binsanity-lc workflow v0.2.6.2 and a minimum contig size of 3 kb (*142*). MAGs were assigned taxonomic classifications with GTDB-Tk v1.5.1 (reference data version r202; (*143*)). Completeness and contamination of MAGs were estimated with CheckM v1.0.5 (*144*). The coverage for each predicted protein and KEGG annotation feature was calculated as transcripts (or fragments) per million (TPM) with count_features v1.3.0, part of our seq-annot package (*85*, *137*). TPM is a proportional unit (multiplied by one million for convenience) that is normalized to the length of

each predicted protein sequence as well as to the total library size. The coverage of each MAG was calculated as the weighted sum of the normalized, proportional coverages (in TPM) of its member contigs. The contig coverages were obtained by mapping all unassembled reads against each MAG with Bowtie2 and then calculating the average coverage per position of each contig with the genomecov command (with the option -pc) in bedtools v2.30.0 (*145*). Normalized coverages in units of TPM were calculated by dividing the average coverage per position by the total number of read pairs for that library.

Processing and Statistical Analyses of Amplicon and Metagenomic Data

16S rRNA gene amplicon sequences were processed with cutadapt v. 1.15 and DADA2 v. 1.10.1, as in previous studies (*85*, *132*). This protocol includes quality trimming and filtering of reads, removal of chimeras, and inference of amplicon sequence variants (ASVs). Taxonomic classification of all ASVs was performed with DADA2 using the SILVA reference alignment (SSURefv132) and taxonomy outline. Sequences from the same sequencing run were analyzed together with DADA2, and the resulting ASVs from separate sequencing runs were merged with phyloseq (*146*). The merged set of ASVs included sequences from chimney biofilms (present study), hydrothermal fluids (*85*), seawater(*85*, *132*, *147*), seafloor rock drill cores (*132*), ambient lab air (present study and (*85*, *132*)), and extraction blanks (present study and (*85*, *132*)). Potential contaminants were removed from the merged set of ASVs with the decontam package using both the "prevalence" and "frequency" modes, as previously reported (*85*). A total of 53 ASVs representing 1,856 sequence counts were removed from chimney biofilm samples with this approach. In addition, ASVs with taxonomic assignments matching those identified as common contaminants of subsurface sequence datasets (*148*) were removed from downstream

analyses, resulting in the removal of an additional 422 ASVs. Finally, ASVs from chloroplasts and mitochondria were filtered from the data set based on taxonomic assignment.

16S rRNA data was imported and analyzed using the R studio environment version 4.2.2, primarily utilizing the Phyloseq package (*146, 149*). Samples were normalized to the median sequence depth and transformed to proportional abundance for simplifying comparative analysis. MAGs with > 50% completion and < 10% contamination were retained for further bin analysis, resulting in 151 bins ranging in completion from 50.72% - 100%, and 0% - 9.94% contamination. Source-tracking to identify potential sources and sinks of sequences was carried out using the R package FEAST (*150*). Samples of seawater (collected via CTD casts during the 2018 Lost City expedition as well as IODP Expedition 357) and drilling fluid samples were classified as putative sources, while plume, biofilm and vent fluids were categorized as sinks to test potentially significant interaction between each of these proximal environments both in situ and during sample processing (*147*). FEAST outputs assigned a fractional contribution between labeled sources and sinks, categorizing unknown contributions as their own category. Pearson correlation tests were carried out in the R environment using the ltm package and the rcor.test() function for ASV-mineralogy matrix and genes-mineralogy matrix (*151*). A correction for multiple tests was carried out using the R package qvalue and qvalue() function (*152, 153*). Significant correlation scores ($p < 0.05$ and $q < 0.05$) were retained as the most statistically significant output for further analysis. Accordingly, three groups for correlations were analyzed within these constraints, aragonite (ARA), brucite (BRU) and calcite (CAL).

Metagenome Assembled Genomes or MAGs were tested for their mineralogical correlations by both simple linear Pearson correlation and in a pairwise matrix as before by using their calculated sequence coverage (in TPM), restricting analysis to bins with over 90%

completion and less than 10% contamination. Bin metabolic potential was assessed by the presence of KEGG metabolic modules for carbon fixation, nitrogen cycling, methane cycling and sulfur cycling, in addition to a selected subset of metal cycling or environmental processing genes (*154*). Analysis was confined to complete KEGG pathway modules in the whole of the dataset as they related to metabolic processes of interest above.

Results

Broad Vent and Community Characteristics

A total of 25 discrete chimney samples were collected from seven sites across the Lost City hydrothermal system at depths between 729 and 875 meters below sea level (**table 1**). Of the total, 24 samples in this study were analyzed for mineralogical composition (aragonite, brucite and calcite weight percent). Aragonite and brucite were the dominant components, but sample lithologies were a combination of all three. Temperature, pH and chemistry of associated hydrothermal fluids were concurrently measured during the same expedition, indicating temperatures at the site up to 96°C, *in situ* pH up to 10, and trends in chemistry consistent with mixtures of H_2-rich hydrothermal fluids with ambient deep seawater (*85*, *155*).

Examining chimney microbial communities through their ASV composition reveals only moderate clustering of samples collected from the same chimney, as in the case of Marker 3 samples (**figure 1)**. This heterogeneity is in line with historical observations of physical differences in venting dynamics and mineral composition even across short distances within one chimney structure (*13*, *100*, *156*). Microbial species richness is also variable among samples from the same chimney; with MKR3 and MKR8 samples having some the lowest richness estimates (**figure 2**). Nearly 50% of all sequences in the dataset are dominated by just 50 ASVs spanning 14 genera (**figure 3**, **table 2**) and a large contingent of genera in some samples account

for nearly 40% of all amplicons. Omitting unassigned genera, the largest contributing taxa also show high numbers of unique ASVs, with the largest being *Thiomicrorhabdus* at 111 ASVs indicating a large contribution of sequence diversity from relatively few taxa, consistent with earlier studies (*55*).

A contributing factor to dissimilarity within and between sites was hypothesized to be the varying degrees of imprinting by the background seawater microbial community. In this scenario, the least active vents may be more impacted by a seawater microbial imprint while the most active vents host what could resemble a core hydrothermal chimney community. To test this, source-sink dynamics were analyzed with the chimney samples and seawater samples collected in and around the Atlantis Massif (**figure 4**). These seawater samples gathered away from the venting environment were potential sources, and chimney biofilms, hydrothermal fluids, and hydrothermal plumes mixing with seawater were classified as sinks. Hydrothermal plume samples showed observable contributions from seawater, as expected, but chimney biofilms showed little if any contributions from seawater. Only three of the 24 chimney samples contained assignable fractions of seawater populations, ranging from 0.02 – 0.20, indicating a distinct biological community in the chimneys from its surroundings as sampled within our dataset.

Correlations between Mineralogy, Taxa, and Genes

Minerals were used as an indicator of environmental conditions influencing microbial community changes. A significant inverse correlation was noted between aragonite and brucite mass fractions (**figure 5**). Of 10,416 microbial taxa identified, 86 showed significant correlations with these minerals. Taxa achieving statistical significance ($p<0.05$, $q<0.05$) were grouped into ARA, BRU and CAL categories based on their associated mineral. Detailed information about

these groups is available in **table A.1**, and their relative abundances in samples in **figure A.1**. Several of the ASVs comprise significant fractions of the samples, upwards of 15% of total relative abundance, making them abundant and possibly critical members of their respective communities.

Clusters that had a positive correlation to aragonite (ARA) included 7 ASVs, 3 Proteobacteria and the one each of Acidobacteria, Actinobacteria, Bacteroidetes, and Chloroflexi. The highest correlated ASV of this group (R = 0.75) belonged to Acidobacteria *Thermoanaerobaculaceae* Subgroup 10. Clusters with a positive brucite (BRU) correlation score contained 4 ASVs, a *Lewinella*, a Chloroflexi, and a Patescibacteria order MSBL5, and an unclassified bacterial sequence. The highest positive correlation score to brucite was *Lewinella* and the unknown (ASV 32052 in our dataset, R = 0.66). Clusters positively correlated to calcite (CAL) contained 68 ASVs, the largest number of all three groups and the highest correlation score of all with *Sulfurovum* (R = 0.82). 21 of the scored sequences belonged to Proteobacteria. 4 archaeal sequences were identified, 3 of which were *ANME-1b* sequences, and 1 archaeal *Candidatus Nitrosopumilus*. Interestingly, one ASV of the recently identified *Candidatus Desulforudis* had a significant association with calcite. Within this group, 11 unknown bacterial sequences were moderate to very strongly correlated with calcite.

Metagenomic sequencing identified 7,452 different protein functions classified by the KEGG orthology. Our analysis focused on genes related to carbon, methane, nitrogen and sulfur metabolisms, as well as selected trace metal cycling pathways, with analysis restricted to pathways where all genes were found. Three carbon fixation pathways comprised of a total of 12 genes showed distinct correlations to underlying mineralogy (**table 3**).

The Calvin-Benson-Bassham cycle showed only positive correlations to brucite in the steps for the conversion of glycerate-3-phosphate to 1,3-biphopshoglycerate and from glyceraldehyde-3P to glycerone-P through *pgk* (K00927), and *tpiA* (K01803) enzyme genes (**figure 6**). The Wood-Ljungdahl pathway showed no positive correlations, with carbon fixation to acetyl-CoA through formate showing negative aragonite correlations with *fdhA* (K05299) and *acsB* (K14138). The TCA and rTCA cycles showed some opposing relationships to aragonite and brucite respectively. In the TCA cycle, *gltA* (K01647), *sucA* (K00164), *sdhB*/*frdB* (K00240), and *sdhC*/*frdC* (K00241) positively correlated to aragonite.

Pathways associated with methane cycling show differentiated patterns of correlation (**figure 7, table 4**). *acs* (K01895), *cdhC* (K00193), and *cdhD* (K00194) are correlated with brucite while *hdrA2* (K03388) correlates with calcite. *cdhE* (K00197) displays a strong negative correlation aragonite. Methane oxidation shows no positive correlations, with *pmoC-amoC* showing a negative brucite correlation. Formaldehyde assimilation to the serine pathway shows a mixed series of correlations, with *AGXT* (K00830), *hprA* (K00018), and *mtkA* (K14067) correlated with aragonite with *mtkB* (K08692) negatively correlated to brucite. Conversion of glycerate-2-phosphate to phosphoenolpyruvate mediated by the *echA* (K01689) gene was correlated with brucite.

Nitrogen cycling only demonstrated correlations in nitrification and denitrification arms (**figure 8, table 6**). Ammonia conversion to hydroxylamine using *pmoC-amoC* (K10946) showed negative brucite correlation. *pmoB-amoB* (K10945) shows a strong negative brucite correlation. Denitrification from nitrate to nitrogen is aragonite correlated *nirK* (K00368) showing significant negative brucite correlation.

Sulfur cycling showed aragonite correlations with *cysD* (K00957), and a strongly negative brucite correlation with *cysNC* (K00955) within assimilatory sulfate reduction (**figure 10, table 5**). A strong brucite correlation was found for *cysK* (K01738) with an equally strong negative correlation to aragonite for utilization of sulfide in forming or maintaining the cysteine pool. Components necessary for the SOX system of thiosulfate oxidation and dissimilatory sulfate reduction showed no notable correlations.

A selection of genes related to trace metal transport systems were examined for any mineral associations (**table 7**). All the identified genes exhibited negative correlations to aragonite, except for *wtpB* (K15496) showing a negative correlation to brucite and all genes were related to tungsten transport.

Metagenomic Bins and Correlated Genes

The sequence coverages (i.e. relative abundances) of 6 MAG bins (with greater than 90% completion and less than 10% contamination) exhibited correlations with mineralogy (**figure 10**), but only one bin (Desulfobulbales_Bin048) achieved q-value significance ($q < 0.05$). Two bins, taxonomically associated with the orders Chromatiales and Thiotrichales, were moderately correlated with aragonite, and four bins of Desulfobulbales, Caulobacterales, and two Methylococcales were correlated with calcite. No MAGs were definitively associated with brucite. Broadly, aragonite-correlated bins contained more genes related to dissimilatory sulfate reduction, thiosulfate oxidation, and copper/zinc transport with the absence of many of our selected nitrogen, carbon and methane cycling genes. In Chromatiales_Bin108 all selected genes for dissimilatory sulfate reduction, molybdenum transport and zinc transport were found. Only one gene related to assimilatory sulfate reduction, *cysC*, and three genes for thiosulfate oxidation, *soxB*, *soxY* and *soxZ* were present. Two nickel/peptide permease transporters and one

nickel/peptide ATP-binding protein were also found. Thiotrichales_Bin148 showed a similar pattern, with partial presence of genes in sulfate and thiosulfate cycling. Additionally, modules for copper transport, heme export and tungstate transport were complete. Notably in both bins, there were no nitrogen cycling, Wood-Ljungdahl, or methanogenesis genes from our selected list.

The four calcite-correlated bins included MAGs affiliated with Desulfobubales, Caulobacterales and Methylococcales. Calcite-correlated bins contained more genes related to assimilatory sulfate reduction, denitrification, carbon and methane cycling, and cobalt or nickel transporters. Desulfobulbales_Bin048 contained all genes for dissimilatory sulfate reduction and zinc transport. Partial Wood-Ljungdahl and carbon fixation was found with the presence of *acsB, acsE, cooS, fdhA* and *cdhE. hdrA2* was the only gene of methanogenesis identified, one *cbiN* for cobalt/nickel transport, and one nickel/peptide permease gene. Caulobacterales_Bin084 contained key genes for denitrification and methanogenesis. Only two sulfite reductase genes, *cysD* and *cysNC*, were found, some genes for heme export and nickel/peptide transport, with none identified for the remaining blocks. Both Methylococcales bins showed similar gene absence for dissimilatory and presence for assimilatory sulfate reduction and several of the metal cycling modules. However, Methylococcales_Bin126 contained two of the SOX system genes, *soxY* and *soxZ*, and several cobalt transport genes not found in its sister bin.

Discussion

Our study aimed to use mineralogy as a proxy for varying microenvironmental conditions and investigate the changes in associated microbial communities living within hydrothermal chimneys at the LCHF. The three dominant minerals at the site, aragonite, brucite and calcite, represent physical snapshots of *in situ* temperature, pH and venting conditions. Younger

chimneys with active and robust flow are dominated by brucite and primary calcite, expected to be stable with hydrothermal venting temperatures over 60℃, while lower temperature chimneys are composed of greater aragonite concentrations, and inactive chimneys are dominated again by calcite as temperatures drop below 15℃ (*100*). The presence of an inverse relationship in samples between aragonite and brucite (**figure 5)** further highlights this distinct relationship, though the exact geochemical parameters of vent evolution are beyond the scope of this particular study and have been investigated by other recent studies (*118, 119, 155*).

This pattern provides a measurable physical environmental gradient against which to analyze the correlations of different microbial taxa and genes, with the hypothesis that this gradient may represent a selective filter for microbial communities directly associated with variables such as substrate limitation, or metabolic / biochemical adaptation. While correlation is not causation, examining microbial distribution through the lens of these mineral proxies provides a window into the complex and dynamic chimney environment and a potential target for more sophisticated microscale analyses. Community analysis as a function of abundance across the site only captures the community composition at the instant of sampling, and cannot on the surface inform us of all the dynamics that led to the contemporary community composition. Bulk analysis by nature takes advantage of a processed sample that inherently mixes slightly different environments and microbial residents. In a site like Lost City, no two samples are exactly alike, and we are faced with a classical ecology challenge in defining strategies by a large number of species utilizing different substrates under extremely challenging conditions (*157*). The first problem, longevity of the environment, means a slow evolution of chimney conditions over timescales longer than typical microbial growth rates, ranging from decades to tens of thousands of years, as demonstrated by differently aged active and inactive

Lost City chimneys (*100*). The second problem concerns microbial turnover dynamics, which, when combined with our first problem, results in not only a slowly evolving environment conducive to microbial coevolution but also a timespan sufficient for extensive microbial mixing and community succession. This complexity hinders the accurate identification of primary colonizers or keystone species, as the community may become increasingly heterogenous and potentially unrepresentative of its original composition in what is a particularly unique and extreme environment. This is further complicated when considering highly variable rates of microbial activity, dormancy, intercellular cooperation, inhibition, or horizontal gene transfer imparting a mosaic of functions (*92*, *158–161*). The resultant challenge then becomes delineating a finite set of variables suitable across the relevant environmental age that some numbers of microbes are most sensitive or responsive to, allowing a differentiation between many of the cosmopolitan microbes found commonly, and the more unique environmentally restricted individuals. Our results conservatively focus on the most correlated genes and microbes to explore the most potentially responsive relationships within a highly complex biogeochemical system. Potentially, there are many co-associations within our dataset to further explore, and this analysis represents a new perspective to consider with respect to the longevity and slow evolving environmental conditions at Lost City.

Chimney microbial communities generally differ from surrounding fluids. Source tracking analysis shows that the microbial communities detected within the vents, compared with fluid samples from the surrounding marine and subsurface fluid environment, differ significantly. We initially hypothesized that due to different degrees of intermixing between exterior and interior conditions of the chimneys, there would be ample opportunity for marine microbes to colonize chimneys of decreased venting status. This does not appear to be the case at

least within this dataset as analyzed and FEAST could not ascertain the putative source of community members from within the samples we selected, compared to vent fluid and plume samples showing some contribution from seawater and subsurface fluid sources. This is consistent with previous observations of limited environmental intermixing within both the Lost City serpentinite subsurface and the venting edifices (*132*). Taxa correlated with aragonite and calcite carbonate mineralogy share similarity with some of the commonly found in other endemic marine sediment communities. Their presence indicates a degree of exchange between those proximal communities as the carbonate vents grow. Some microbes in our dataset are notable in their previously observed links to the microbiomes of sea sponges, corals and shell bearing fauna where they can stabilize or contribute to the mineralization of their carbonate structures, such as *Robiginitomaculum.* Others are associated with hydrocarbon degradation in the Mid-Atlantic Ridge, along with *Woeseia* (*162–166*), which may suggest a relatively accessible supply of carbon substrates that would otherwise not be plentiful in the most anoxic interior regions of the vents.

While aragonite is relatively stable as hydrothermal venting subsides, increased calcite (wt%) represents the final stage of the vent lifecycle due to its increased formation at much lower temperatures. An enhanced degree of diversity and richness thus would be expected in vents with high calcite concentration owing to the moderation of extreme conditions, and an increased availability of substrates and cofactors either from their availability in seawater or their increased solubility due to more neutral pH and lower ambient temperatures. Additionally, species feeding off of preformed organic matter originally produced by chemolithoautotrophs may facilitate the colonization of the mineral substrate by secondary consumers, akin to successional processes documented in other environments (*167, 168*). A strong

Candidatus_Nitrosopumilus correlation to calcite may be indicative of this gradient as known autotrophic ammonia oxidizers that are highly dependent on organic matter and physiologically vary accordingly between bathypelagic and hadal zones of the ocean (*169–171*). The identification of a correlated *Sulfurovum* firmly within the calcite associated category may be evidence of at least some taxa adapted to moderate hydrothermal conditions including exposure to oxygenated seawater. Previous studies examining Lost City *Sulfurovum* suggested a mixotrophic lifestyle or the capability of inhabiting a transition zone between the anoxic interior and exterior of the vent (*84*). Our results support this given the increased abundance of the taxa associated with the presence of calcite, and the overall distribution through the vent may indeed show it colonizing an intermediate region. *Candidatus Desulforudis*, initially discovered kilometers into Earth's crust and subsequently found in another terrestrial serpentinite-hosted site, suggests potential interconnections between subsurface environments and the possibility of an ecological niche along the venting pathway or a subsurface-driven dispersal mechanism (*172*, *173*). *Sulfurovum* and multiple other hydrothermally associated taxa have been frequently identified in marine sediments to varying extents further highlighting some shared similarity between different environments (*174–177*).

Secreted components of cells, in addition to the cells themselves have been known to be nucleation sites for carbonate precipitation and have been hypothesized to contribute to the formation of some parts of other similar hydrothermal vent systems (*178–180*). There is a high likelihood that carbon metabolism increases carbonate mineralization either through carbonic anhydrase (catalyzing bidirectional formation of bicarbonate from CO_2 and water) or urease (catalyzing urea breakdown to CO_2 and ammonia) activity (*181–183*). Precipitation would thus naturally increase with greater CO_2 sequestration and could contribute to the associated bloom of

microbial diversity with both aragonite and calcite. The increased activity could plausibly increase biomineralization and further indicate more carbon cycling. Intriguingly, this would partly explain why the top genera in our dataset dominate the site, particularly with so many unique ASVs. The largest constituent, *Thiomicrorhabdus* (111 ASVs), is known to contain carbonic anhydrase activity, and although it is not correlated with specific minerals in our dataset, it is widely dispersed and occupies much of the carbonate-bearing substrate within the site (*73*, *184*). The same can be found for *Desulfotomaculum* (50 unique ASVs), *Sulfurovum* (74 ASVs) and *Woeseia* (85 ASVs), and if the pattern hold true, would place them within intermediate regions of the vent at Lost City and associated with much wider habitat ranges in the marine sediment. This large number of ASVs specifically associated with the most abundant taxa indicates a microdiversity arising from long lived and relatively stable populations within the site. The higher resolution provided with ASV analysis highlights the possible existence of nuanced ecotypes across an evolving habitat range that preserves the overall persistence and resilience of the population, similar to environments with seasonal cycles (*185–187*). Though Lost City doesn't experience seasonality, the venting environment does change over the lifetime of the vent and this microdiversity could be a byproduct of this change in addition to possibly influencing the makeup of the local microbial environment over time as an adaptation to an incredibly challenging environment (*188*).

Brucite relationships as a window into the most extreme metabolic adaptations. The very limited number of taxa correlated with brucite, including the absence of any high-quality MAGs, may be indicative of the more extreme environmental conditions associated with brucite stability. Aragonite and brucite show an inverse correlation, and similarly some taxa mirror this by displaying distinct inverse correlations between the two minerals creating the appearance of a

distinct difference in habitat ranges for the correlated taxa. The identified *Lewinella* has been observed to particularly be much prevalent and diverse in anaerobic and saline environments, including bioreactors (*189*). An MSBL5 order ASV correlated with brucite is notable of because of its identification in hypersaline and other serpentinizing environments such as the Prony Bay Hydrothermal System (*91*). Several other MSBL5 ASVs were identified associated with calcite and when considering the formation of primary calcite alongside brucite early in vent formation, and their association with other serpentinizing sites there is a distinct possibility of the order's range falling within the interior of the vent brucite/calcite regions. A similar pattern can be identified for ASVs of class Parcubacteria, known to exist in hyperalkaline and hadal environments, where there is a single brucite associated taxa, and two calcite associated taxa in our dataset (*190, 191*).

Gene correlations highlight metabolic differentiation within vent chimneys and inform community adaptations. Within vent chimneys, gene correlations shed light on the metabolic differentiation among resident microbes. By mapping correlated genes within their respective pathways, we gain insights into the dominant metabolic strategies employed by these microorganisms. The presence of variable gene counts cannot be reasonably attributed to a single cause but may indicate several underlying factors driving differential abundance. One potential explanation is that different species possessing different and variable genes copy numbers may form correlations when they preferentially inhabit regions with distinct mineral compositions or constitute a significant portion of the microbial population. Such microbes may also over represent key metabolic pathways with a high abundance of gene copies. This scenario suggests the existence of specialized populations adapted to specific environmental ranges as already suggested by our amplicon sequence data and the high number of ASVs within different taxa.

Substrate availability also plays a pivotal role, influencing either an increase in gene abundance within specialized microbial populations over time or reflecting inherent limitation *in situ*. Limited and essential substrates necessitate the heightened production of uptake and use components, leading to increased gene abundances associated with these processes.

In addition to substrate limitations, the stability of metabolic pathways, both partial and complete, can further influence differential gene counts and constrain potential metabolisms. The extreme conditions within chimney interiors, characterized by high temperatures and high pH levels, demand microbial adaptation, driving the continuous production and maintenance of conformationally and functionally stable enzymes across this challenging environmental regime. This adaptation might partly explain their mirroring of inverse correlations between aragonite and brucite, as well as the consistent negative correlations observed among certain genes with no positive correlations.

Considering brucite as a reliable indicator of the hottest and highest pH regions within the chimney, while aragonite represents fewer extreme areas resembling to an extent neighboring marine environments, our data suggests a metabolic differentiation between these two regions. Carbon fixation strategies in brucite hint at reliance on the Calvin-Benson-Bassham, rTCA, and Wood-Ljungdahl pathways, with the last inferred the negative aragonite correlation of two key pathway steps. Interestingly, two correlated genes associated with the Calvin cycle (*pgk*, *tpiA*), downstream from CO_2 fixation through RuBisCO, also overlap in function with glycolysis which could result in their alternative use in that pathway over CBB in some organisms. Although previous evidence demonstrates that these genes can be transcribed together as a cluster, the extent and nature of this activity remain unexplored in our study (*192*). Whether there is a gene clustering phenomenon associated with this, or other extreme environment sites is unclear but

would make sense in facilitating the rapid and efficient sequestration of carbon dioxide into the cycle, while creating a functional redundancy with other energy harvesting pathways for example. Lost City and other high temperature sites are known as hotbeds for horizontal gene transfer (HGT) between microbes, and in addition to any possible gene clustering, high rates of HGT would permit the transfer of these overlapping gene components (*193*).

The overall negative relationship between components of the Wood-Ljungdahl pathway and aragonite is not surprising. The strong negative aragonite correlation observed in the Western branch of the cycle could be inferred to possibly be a brucite relationship and indicates the biologically sufficient availability of CO_2 and formate substrates in that environment. If we presume a brucite relationship, then there is a strong preference for forming and utilizing formate, and the production of acetyl-CoA. Notably, 5,10-methylene THF and THF are crucial products for carbon cycling and as an intermediate linked to methane cycling. Their downstream relationships with a hypothesized brucite correlation appear to bookend the importance of their formation given their upstream correlations.

While we identified components of the TCA and rTCA cycles, the former exhibited more correlations with aragonite. Initial use of acetyl-CoA by *gltA* correlated with aragonite, but also strongly negatively correlated with brucite. The rate-limiting step of the TCA cycle involves the conversion of isocitrate to 2-oxoglutarate/α-ketoglutarate, and this products conversion to succinyl-CoA correlates with aragonite, and negatively with brucite. The positive correlations observed for *sdhB* / *sdhC* may represent an adaptation for maintaining TCA cycle products, particularly fumarate, under stressful conditions which aligns with the moderate hydrothermal conditions associated with high aragonite content (*194*). Here, we presume that similar correlations in a common and critical cycle as this may indicate the overall correlation, and why

their placement with the strong negative and positive correlations firmly placing them in an aragonite relation. Though only two correlated products were identified, the rTCA cycle may show the reverse relationship. The two *fumA* and *fumB* brucite correlated and aragonite anticorrelated genes for conversion of malate to fumarate further underline importance of fumarate. Two genes independently correlated to brucite may be underpinned by the specific stability of a final two subunit product over a larger single enzyme, but it is unclear why. The large subunit of citryl-CoA synthetase encoded by *ccsA*, highly correlating with brucite, participates in the specific ATP-dependent conversion of citrate to citryl-CoA, and has resemblance to succinyl-CoA synthetase with a high degree of ATP sensitivity (*195*). An inhibitory effect by succinyl-CoA synthetase may cause discontinuation of the rTCA cycle and would explain why an increased abundance of *ccsA* would help drive the conversion process forward against a possible inhibitory threshold. The strong negative and positive correlations here point towards the likely association of the overall cycle with brucite abundances.

Methanogenesis appears primarily brucite-correlated at three key steps: conversion of acetyl-CoA to 5-Methyl-THM(S)PT, formation of coenzymes B/M and the regeneration of methyl-CoM from methanol. Conversion of acetyl-CoA to 5-methyl-THM(S)PT is primarily facilitated by the archaeal carbon monoxide dehydrogenase, detected by subunit archaeal genes *cdhC, cdhD* and *cdhE*, the last showing high negative to aragonite, linking it to brucite. The *cdh* genes detected may exhibit a related correlation to brucite and could further indicate a link for further exploration between the carbonyl branch of the Wood-Ljungdahl pathway and methanogenesis and/or acetogenesis in an archaeal community within the brucite pathways of the vents. In the production of coenzymes M and B, there is a significant and mixed correlation of *hdrA2* to calcite. This gene has been heavily studied in ANME microbes and generally are

transcribed as a clustered complex, utilizing H_2 as an electron donor as they carry out methanogenesis (*196*). Methane oxidation trends towards aragonite correlation based on the strong negative brucite correlation of *pmoC-amoC*. An aragonite relationship may indicate gene prevalence at an older stage of mature vent activity, leaving methanotrophy as a regional function isolated from the primarily reducing conditions at the vent core just based on the aragonite relationship. Formaldehyde assimilation correlations show a possible zonation between methanotrophs, with the ribulose monophosphate pathway to D-fructose-6P associated with type I methanotrophs showing no clear correlations, while type II methanotrophs utilizing the serine pathway of formaldehyde assimilation, generally correlates with aragonite and possibly prevalent in a more intermediate environment, showing strong negative correlations to brucite (*197*).

Nitrogen metabolism splits neatly between nitrogen ammonia oxidation and denitrification in primarily aragonite regions. Ammonia and methane oxidation demonstrate linkage in multiple ecosystems and in some instances competitive inhibition at higher temperatures (*198*). Likely, nitrogen fixation dominates internally within vents driven by LCMS, with nitrification and denitrification taking place to varying degrees across an increasingly diverse community towards vent exteriors (*55*).

The most sensitive sulfur cycling genes related to sulfate assimilation, with several convergences indicate a sulfate cycling system correlated with aragonite. The only positively brucite correlated gene was *cysK*, cysteine synthase A. CysK, while canonically involved in cysteine biosynthesis, is sensitive to sulfur starvation and its abundance increases as a result. Notably, its transcription increases with high pH and zinc (*199–201*).

Trace metal availability and sensitivity can influence key metabolic cofactors. Many of the genes selected rely on metal cofactors for the catalytic centers of their products, the largest

category being Fe-S centers with variable overall correlations across the site. We identified no strong correlations with iron transporters or related genes, possibly indicating no iron limitations at the site. All the identified genes related to tungsten or tungsten / molybdenum transport and three out of four show a brucite relationship indicating at least a sensitivity within those communities for their use. We could conclude that where those metal associated genes show relationships is indicative of a response to those metal limitations and a significant energetic expenditure for their uptake. Previous studies examining the distribution of trace metals between biofilm and vent matrix showed 83% of iron detected was concentrated within the biofilms, and the remainder in the vent matrix, in addition to high levels of tungsten accumulation in the hydrothermal environment (*202*, *203*). Lost City is considered iron poor with concentrations below detection limits, with a large number of other metal concentrations (Mn, Ni, Co, Cu, and Mo) either in single digit ppm concentrations or below detection levels in active vents (*100*). The correlations point to a possibly increased utilization of tungsten and / or molybdenum within the brucite matrix consistent with earlier studies of chimney geochemistry at the LCHF and the solubility of metals at high pH (*100*). This suggests that, in this context, there may be more nuanced spatial limitations to overcome for the biofilm growth and colonization.

Lost City highlights the complexity of in situ microenvironments and their microbial residents. Our research focused on finding a reliable physical indicator to track changes in the microenvironment of different chimneys at Lost City. We chose mineralogy as this indicator, revealing a clear gradient linked to the chimneys' formation and evolution. This approach allowed us to pinpoint crucial patterns that are sensitive to this gradient. Initially, chimney vents are rich in brucite, reflecting the hot, anoxic fluids from the serpentinizing system below. In this harsh setting, only a few organisms persist, relying on mutually beneficial

relationships to make the most of the available methane, hydrogen, and limited dissolved bioavailable carbon. As the vents mature, they develop a balance of aragonite and brucite, with brucite diminishing with decreased temperature. This shift leads to a more permissive environment, supporting a wider variety of microbes and metabolic processes, as evidenced by changes in carbon fixation, methane, nitrogen, and sulfur cycling profiles. In the absence of cultured isolates, this kind of multi-disciplinary approach allowed us to dissect how microbial communities are structured within the chimneys and to identify their potential constraints. Lost City-type environments are believed to have been widespread on early Earth. Studying the structure of microbial communities in these environments can reveal how they function, and how the potentially ancient metabolic strategies they harbor evolved within the changing chemistry of the system. The origins of proto-metabolism on Earth may have occurred in conditions like those at Lost City (*62*, *95*, *204*). This implies that the advantages and limitations of this environmental setting have persisted for billions of years, with current organisms highly adapted to them. By further pinpointing, measuring, and defining the conditions these microbes thrive under, we can gain a clearer understanding of how microbial life endures in other harsh environments.

Acknowledgements

We extend our gratitude for the careful cooperation, advice and help of the captain and crew of the R/V Atlantis, ROV Jason and the scientific party aboard for expedition AT42-01. We are especially grateful for the technical support provided by Dr. Julia McGonigle for the preparation and processing of samples for sequencing. Support for this work was provided by NSF awards OCE-1536702 / 1536405 / 153962, the Swiss National Science Foundation project 200021-163187, Joint Institute for the Study of the Atmosphere and the Ocean (JISAO) / NOAA Cooperative Agreement NA15OAR4320063 Contribution 2021-1132, the Deep Carbon

Observatory, NASA Astrobiology Institute, Michigan Space Grant Consortium, and the Philippine Department of Science and Technology – Science Education Institute (DOST-SEI).

Tables

Table 1 - Subsamples included in this study, their location, label used for analysis, and mineralogical content for aragonite, brucite, and calcite in weight percent.

Sample	Jason Sample ID	Location	Location Label	Type	Depth (m)	Latitude	Longitude	Aragonite (wt%)	Brucite (wt%)	Calcite (wt%)
LC02867	J.1107.16Sept.1708	Marker 3	MKR3	Active Chimney	729.67	30.1205243	-42.1243348	30	66	3
LC02870 A/C	J.1107.16Sept.1723	Marker 3	MKR3	Active Chimney	729.69	30.1205071	-42.1243435	20	78	2
LC02876	J.1107.16Sept.1714	Marker 3	MKR3	Active Chimney	729.7	30.1205091	-42.1243436	35	61	4
LC02881	J.1107.16Sept.1713	Marker 3	MKR3	Active Chimney	729.68	30.1205119	-42.1243414	50	49	1
LC02923	J.1108.17Sept.2301	Marker 6	MKR6	Active Chimney	797.97	30.1245919	-42.1193596	65	34	1
LC02928	J.1108.17Sept.2002	Calypso	CAL	Active Chimney	797.95	30.1245946	-42.1193284	23	54	22
LC02934	J.1108.17.Sept.2223	Venting Wall	VW	Venting Wall	795.19	30.1246195	-42.1193754	94	6	1
LC02938	J.1108.17Sept.1338	Calypso	CAL	Active Chimney	797.44	30.1242902	-42.1193738	26	71	2
LC02954	J.1109.Sep19.0756	Sombrero	SOM	Active Chimney	761.71	30.1240556	-42.1195502	96	4	1
LC02958	J.1109.Sep19.1033	Carbonate Veins	CV	Inactive Vein	741.1	30.1249291	-42.1188567	13	59	28
LC02964	J.1109.Sep19.1011	Carbonate Veins	CV	Inactive Vein	740.89	30.1249447	-42.1188485	29	42	29
LC02967	J.1109.Sep19.1016	Carbonate Veins	CV	Inactive Vein	740.9	30.1249298	-42.1188394	47	24	29
LC02981	J.1110.20Sep.0611	Marker 8	MKR8	Active Chimney	801.21	30.1204738	-42.1249175	30	68	1
LC02985	J.1110.20Sep.0609	Marker 8	MKR8	Active Chimney	801.21	30.1204738	-42.1249175	34	63	2
LC02990	J.1110.20Sep.0817	Marker 8	MKR8	Inactive Vein	871.44	30.1203248	-42.1257789	14	61	25
LC02993 B/D	J.1110.20Sep.0838	Marker 8 Vein	M8V	Inactive Vein	874.96	30.1202751	-42.1256963	38	18	33
LC02998	J.1111.21Sep.0938	Marker 8 Vein	M8V	Inactive Vein	788.23	30.1177429	-42.1247982	94	1	6
LC03001	J.1111.20Sep.2240	Sombrero	SOM	Active Chimney	762.11	30.119726	-42.124407	62	32	6
LC03005	J.1111.20Sep.2214	Sombrero	SOM	Active Chimney	762.08	30.1197175	-42.1243882	68	24	9
LC03008	J.1112.22sSep.0113	Marker 6	MKR6	Active Chimney	777.05	30.1207253	-42.1241496	87	12	2
LC03012	J.1112.22Sep.0110	Marker 6	MKR6	Active Chimney	777.16	30.1207231	-42.1241433	51	49	1

Table 2 - Representative table of the most abundant genera sequenced from the vents in order of decreasing total percent relative abundance, and including the number of ASVs found in our dataset.

Genus	**# Unique ASVs**	**% Abundance**
Thiomicrorhabdus	111	8.9
Desulfotomaculum	50	8.3
Roseobacter_clade_NAC11-7_lineage	17	7.9
Sulfurovum	74	7.1
Marine_Methylotrophic_Group_2	37	3.5
Sulfurospirillum	15	2.8
Cocleimonas	33	2.6
Serpentinicella	20	2.3
pItb-vmat-59	24	2
Moritella	4	1.7
Marine_Methylotrophic_Group_3	19	1.7
Sva0996_marine_group	70	1.4
IheB2-23	47	1.3
Desulfobulbus	9	0.9
Actibacter	18	0.8
Methanosalsum	7	0.7
Sedimenticola	4	0.4
Lutimonas	6	0.4
Woeseia	85	0.4
Ruegeria	2	0.4
Desulfurivibrio	3	0.4
Filomicrobium	46	0.4
Litoreibacter	3	0.3
Cenarchaeum	2	0.3
Photobacterium	4	0.3

Table 3 - Selected significantly correlated ($p < 0.05$, $q < 0.05$) genes sorted by their metabolic relationship to carbon cycling, methane cycling, sulfur cycling and nitrogen cycling. Each gene characterized by its Kegg ID displays the Pearson correlation score. Negative correlations where found are included. For gene products where a Uniprot entry was found including metal cofactor information, the cofactor(s) is identified.

KEGG ID	Mineral Correlation(s)	Correlation Score	Gene	Metal Cofactor
Carbon Cycling				
K00927	Brucite	0.73	*pgk*	Mg
K01803	Brucite	0.68	*tpiA*	-
K14138	Aragonite	-0.72	*acsB*	Ni
K05299	Aragonite	-0.71	*fdhA*	Fe, Mo
K00164	Aragonite Brucite	0.72 -0.70	*sucA*	-
K00240	Aragonite	0.69	*sdhB/frdB*	Fe
K00241	Aragonite Brucite	0.70 -0.68	*sdhC/frdC*	-
K01647	Aragonite Brucite	0.67 -0.68	*gltA*	Fe
K15232	Aragonite Brucite	-0.68 0.68	*ccsA*	-
K01677	Aragonite Brucite	-0.72 0.72	*fumA*	Fe
K01678	Aragonite Brucite	-0.74 0.72	*fumB*	Fe
K00177	Aragonite	-0.67	*korC*	-
Methane Cycling				
K01895	Aragonite Brucite	-0.72 0.71	*acs*	Mg, Mn
K00193	Aragonite Brucite	-0.73 0.73	*cdhC*	Fe, Ni
K00194	Aragonite Brucite	-0.76 0.70	*cdhD*	Fe
K00197	Aragonite	-0.75	*cdhE*	Fe
K03388	Aragonite Calcite	-0.70 0.74	*hdrA2*	Fe
K10946	Brucite	-0.72	*pmoC-amoC*	-
K00830	Aragonite Brucite	0.68 -0.72	*AGXT*	-
K01689	Brucite	0.67	*echA*	Mg
K08692	Brucite	-0.72	*mtkB*	Mg
K14067	Aragonite Brucite	0.71 -0.75	*mtkA*	Mg
K01622	Aragonite	-0.70	*K01622*	Zn
Sulfur Cycling				
K00955	Brucite	-0.76	*cysNC*	Mg
K00957	Aragonite Brucite	0.70 -0.82	*cysD*	Mg
K01738	Aragonite Brucite	-0.69 0.74	*cysK*	-
Nitrogen Cycling				
K10946	Brucite	-0.72	*pmoC-amoC*	-
K00368	Aragonite Brucite	0.76 -0.73	*nirK*	Cu
Metals				
K05773	Aragonite	-0.72	*tupB*	W
K06857	Aragonite	-0.73	*tupC*	W
K15496	Brucite	-0.70	*wtpB*	Mo/W
K15497	Aragonite	-0.67	*wtpC*	Mo/W

Table 4 - Presence and absence of selected genes related to metabolic and metal cycling in bins correlated with aragonite and calcite. Bins 90% complete with <10% contamination were selected and presented here at the taxonomic order level.

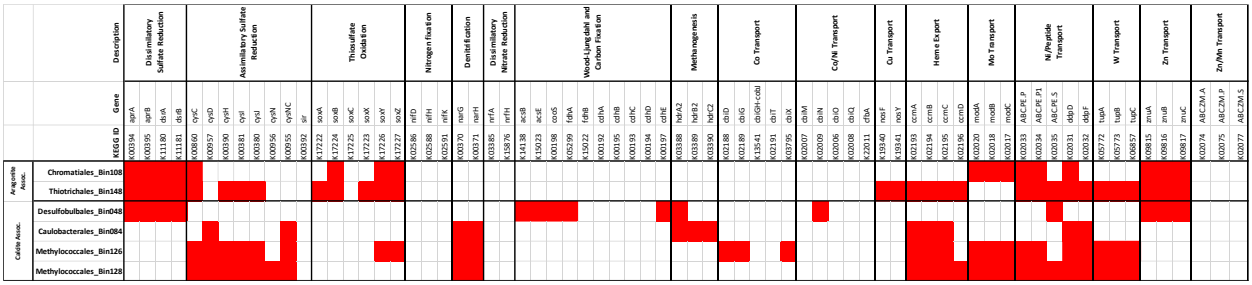

Figures

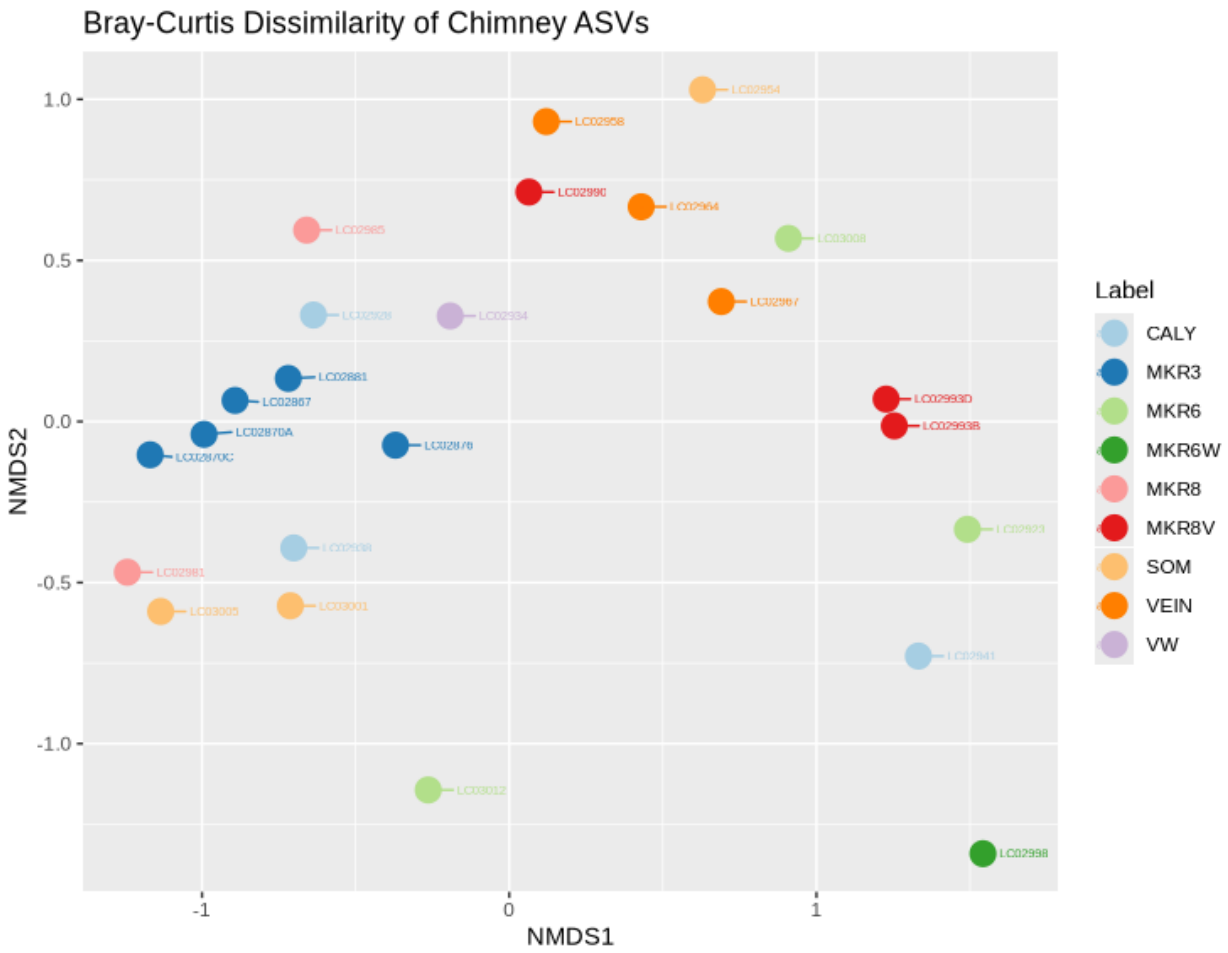

Figure 1 - Bray-Curtis dissimilarity NMDS of the microbial composition between samples from Lost City vents. Circles are individual samples colored according to their respective locations.

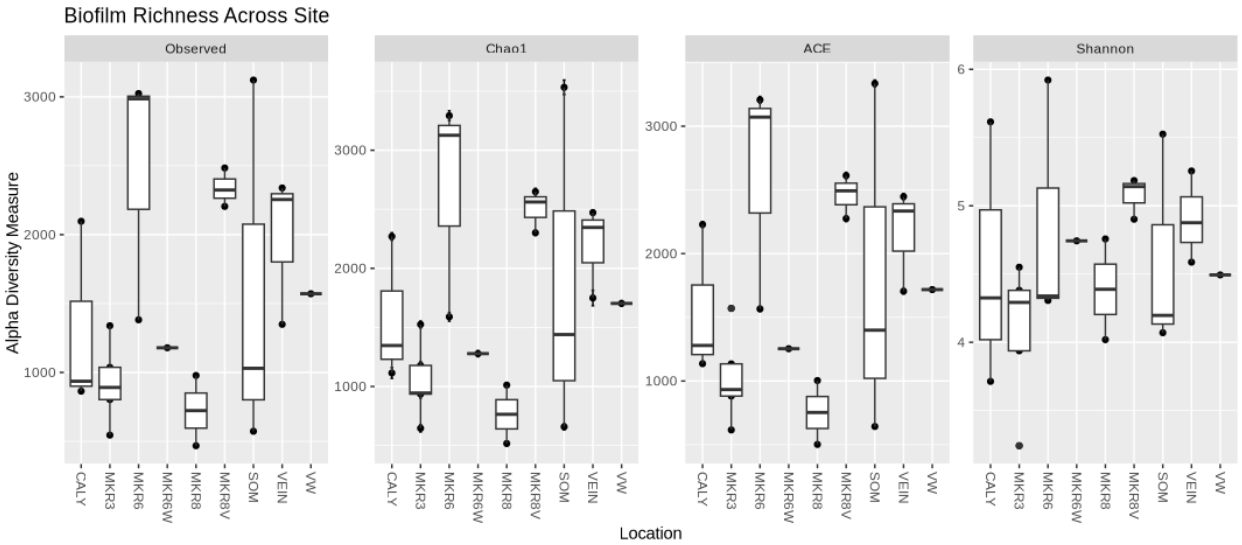

Figure 2 - Community richness / alpha-diversity comparing observed, Chao1, ACE, and Shannon indices for each location based on the untrimmed ASV counts.

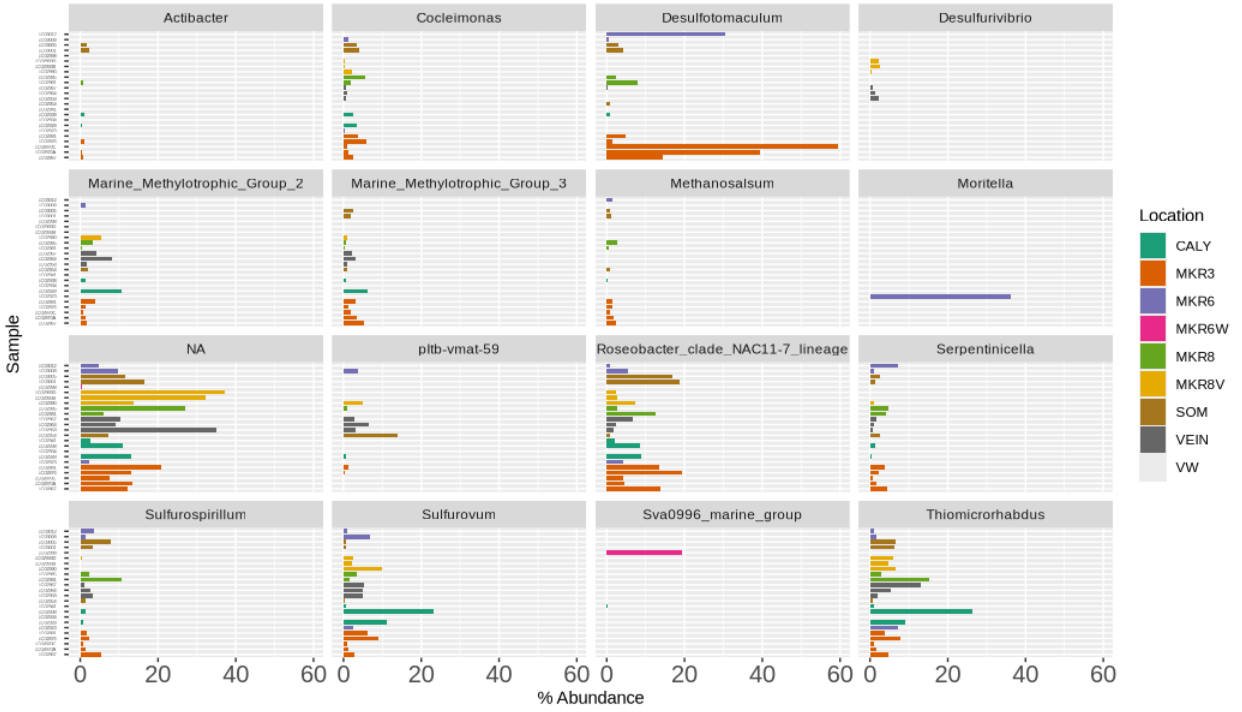

Figure 3 - Percent relative abundance of the top 50 ASVs' genera from chimney biofilms by genus within each sample.

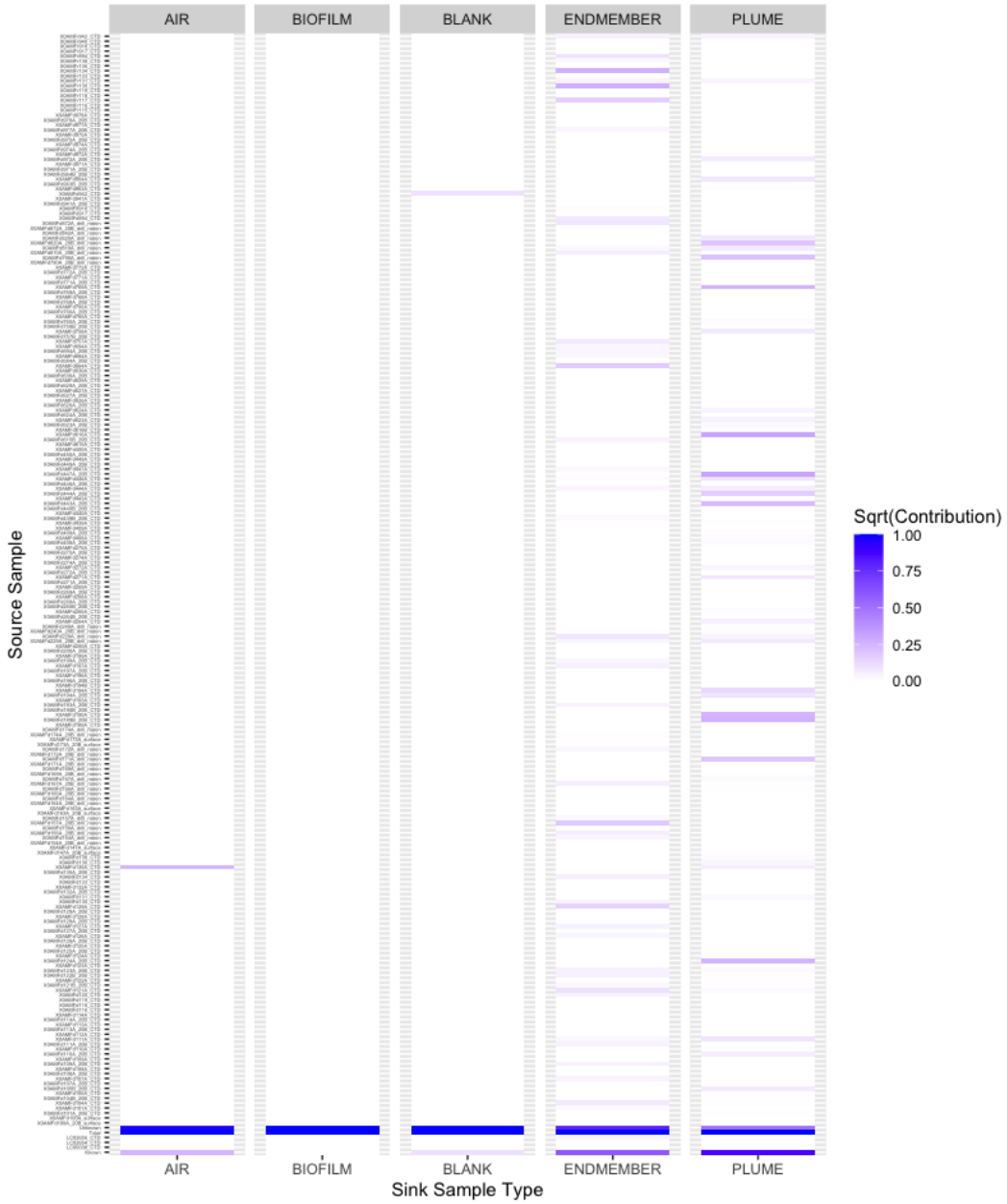

Figure 4 - FEAST derived source-tracking of microbial community members. Each row represents a single source for consideration, primarily fluid sampling historically from across the Atlantis Massif and vent end member fluids from the 2018 expedition. Columns are consolidated sample types for testing as sinks of microbes. In order: air samples were taken during sampling and DNA extraction for cross-contamination tracking. Biofilm samples represent the crushed and DNA extracted carbonate samples from the 2018 expedition. Blank samples were used during DNA extraction and sequenced accordingly. Endmember samples were fluid samples taken directly from the venting chimneys at Lost City. Plume samples were putative Lost City plumes sampled via CTD and represent an intermixing between sea and vent environments. Where a row or source is calculated to contribute to the sink sample, the area is shaded relative to the intensity of the contribution. One source is labeled as unknown, representing the relative contribution from an unknown sink we do not have in our dataset.

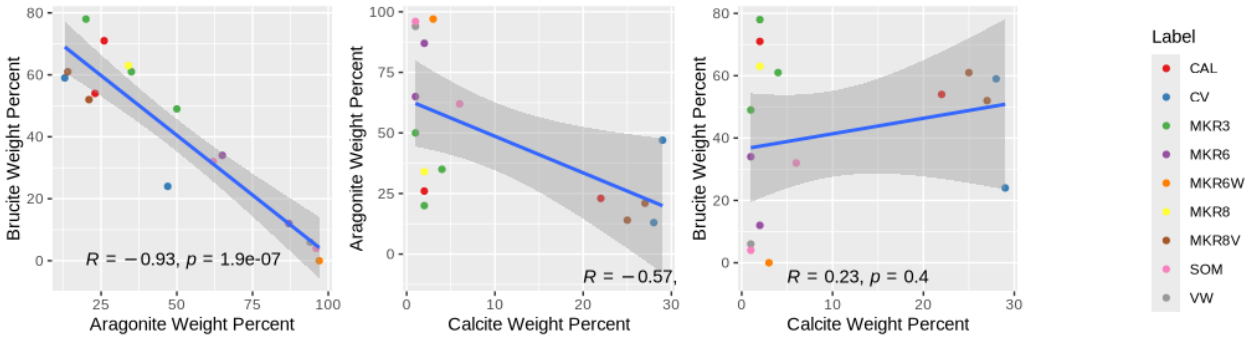

Figure 5 - Linear correlation between the different mineralogy weight percents of samples, colored by location. From left to right: brucite weight percent to aragonite weight percent, calcite weight percent to aragonite weight percent, and brucite weight percent to calcite weight percent.

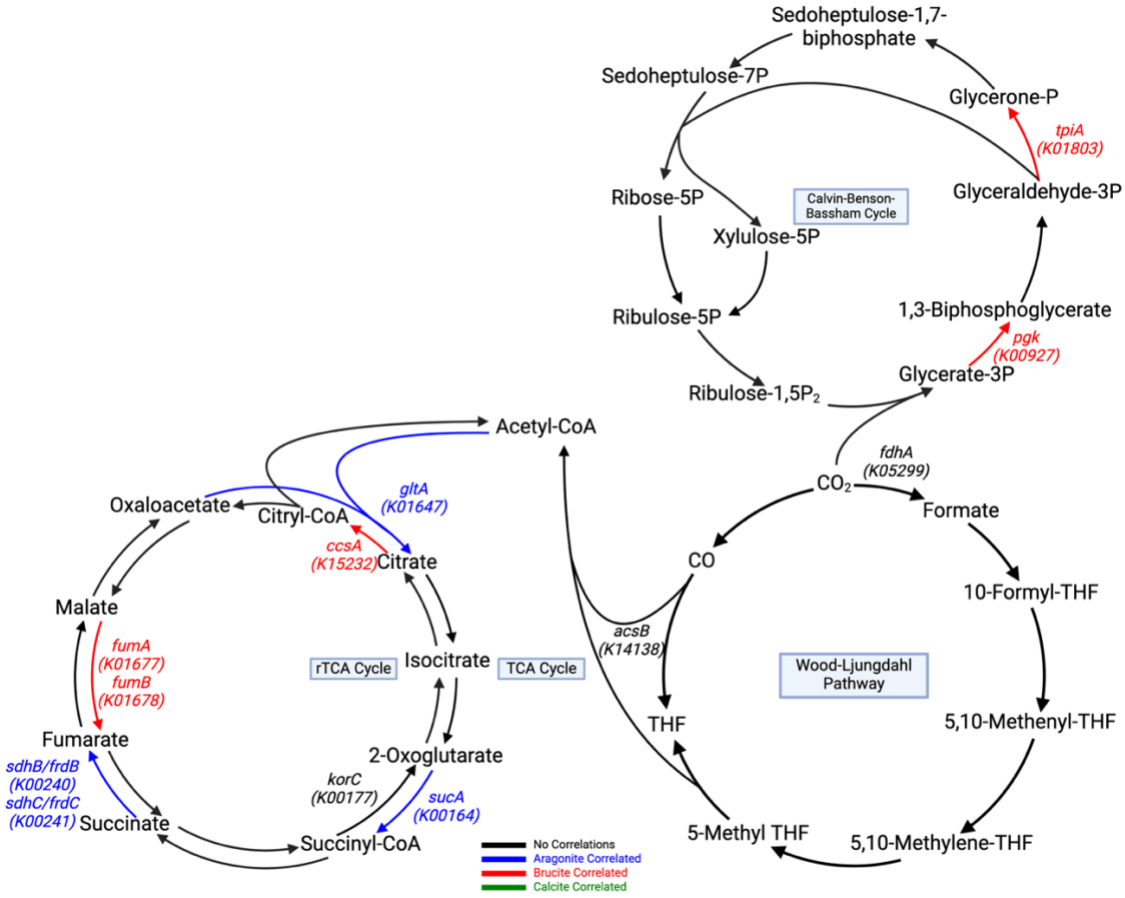

Figure 6 - Carbon fixation pathways assembled from correlated genes with a Kegg ID color coded to their respective positive mineral correlate. Calvin-Benson-Bassham Cycle, rTCA and Wood-Ljungdahl pathways show generalized brucite association, or in the case of Wood-Ljungdahl, a negative aragonite correlation at key steps. The TCA cycle contains pathway steps correlated with aragonite. Created with BioRender.com.

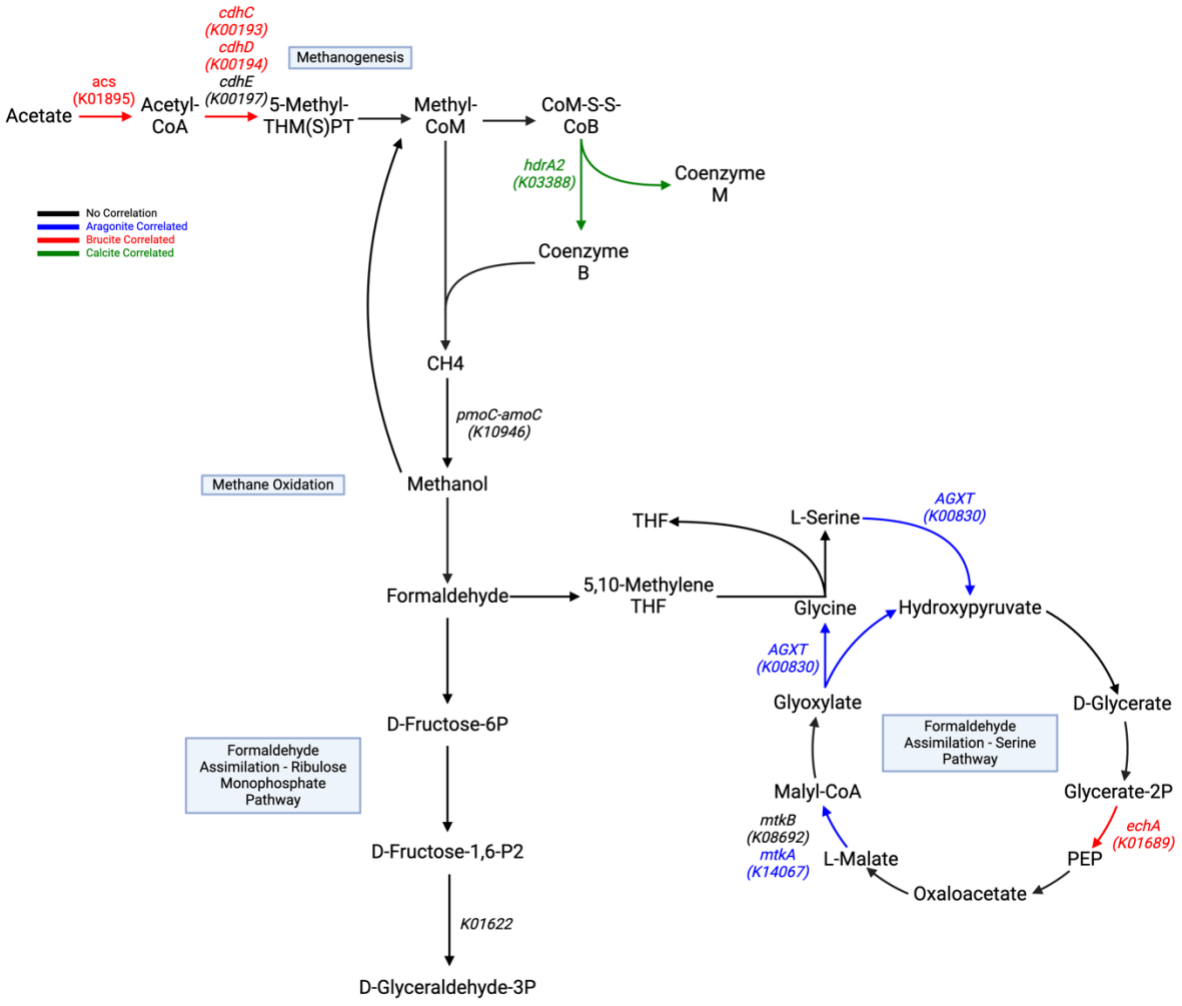

Figure 7 - Different directions of methane cycling show trending correlations to different minerals. Methanogenesis component genes correlate highly to brucite and calcite, while methane oxidation and formaldehyde assimilation through the serine pathway are broadly correlate to aragonite. Formaldehyde assimilation through the ribulose phosphate pathway has some mixed correlations primarily to brucite and calcite. Created with BioRender.com.

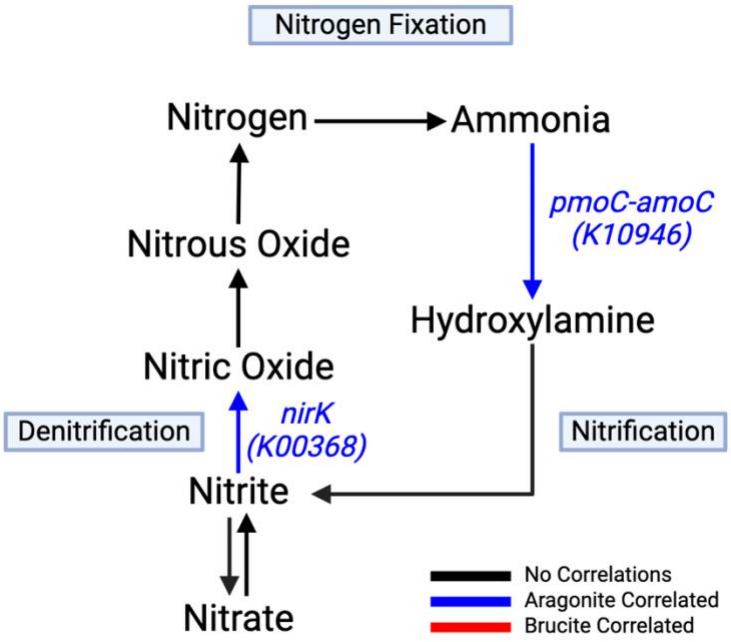

Figure 8 - Nitrification and denitrification arms strongly correlate to aragonite. Conversion of nitrate to nitrite by the napA (K02567) gene product shows strong negative correlation to brucite. Created with BioRender.com

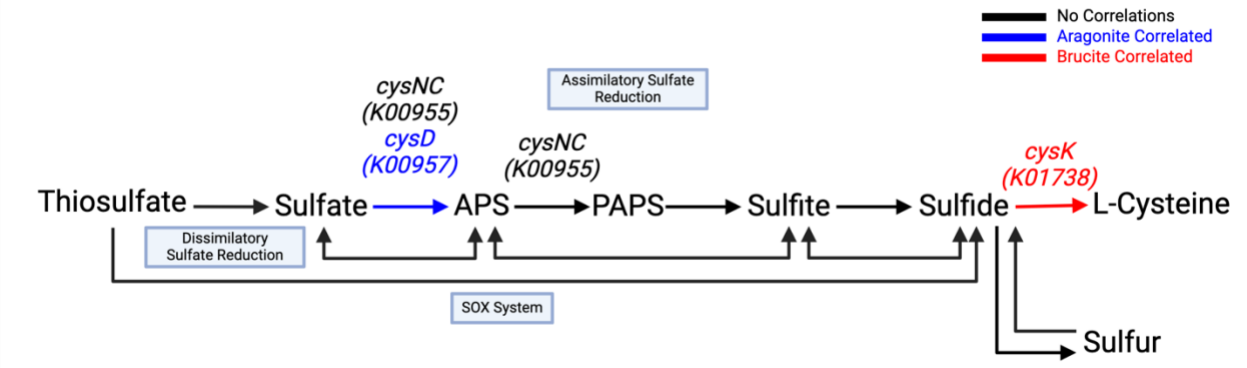

Figure 9 - Sulfur cycling through assimilatory sulfate reduction is favored in the aragonite environment. Utilization of sulfide for cysteine biosynthesis is highly correlated to brucite via the cysK (K01738) gene product. Created with BioRender.com.

CHAPTER 3 - MICROBIAL HOTSPOTS ASSOCIATED WITH TRACE METAL DISTRIBUTIONS IN VENTS AT THE LOST CITY HYDROTHERMAL FIELD

Abstract

Hydrothermal vents are commonly thought of as rich sources of metals in the deep-sea, visible as metal-enriched plumes, and considered as a potentially exploitable source of heavy metals necessary for the myriad of technologies in use today. However, highly alkaline environments associated with serpentinization such as the Lost City Hydrothermal Field (LCHF), the Prony Bay Hydrothermal Field, and similar, extinct sites near mid-ocean ridges are metal depleted. This depletion may inherently limit microbial growth and metabolism even in seemingly energetically rich systems. In this study the identity and distribution of heavy metals in carbonate hydrothermal vent chimneys from the LCHF was investigated using microscopic and spectroscopic approaches. The coordinated direct observations were complemented with analyses of shotgun metagenomic data from the same sample suite, focusing on genes involved in metal acquisition and transport. Microscopic and spectroscopic observations showed that the microbial cells and biofilms were concentrated along brucite lined channels within the porous chimney structures, suggesting that they were recently exposed to circulating hydrothermal fluids. Additionally, investigation of these regions using Laser-Ablation ICP-MS showed that heavy metals were typically much more concentrated in these areas, even if they were below detection limits in hydrothermal fluids and in bulk scale analyses of solids. An analysis of the metal transport and storage genes showed similar trends pointing to the potential for a robust microbial metal cycling component at the vent-fluid interface not reflected anywhere else in the chimney matrix. While it is unclear whether the microbial biofilms sequester metals from the environment or are attracted to areas of metal deposition, these data suggest a strong link

between trace metal occurrence and microbial distributions. These data are important to consider in terms of understanding microbial physiology and ecology in this enigmatic ecosystem, with further implications for models related to the origins and early evolution of life in Lost City type environments.

Introduction

Trace Metals are an Essential Component of Biological Processes

The essence of biology is the ability to catalyze reactions faster and more efficiently than they would otherwise occur. To overcome the energetic barriers to do this, life has evolved and conserved very structured processes, harnessing energy and resources to maintain order in the face of disorder. Enzymes are the catalytic drivers for these key biochemical reactions and are dependent on transition metals at their reaction centers. Metal components of enzymes primarily function as cofactors for oxidation-reduction reactions to take place, facilitating the transfer of electrons during key biochemical processes of anabolism and catabolism, the central processes of all life. Proteins and catalytic enzymes are functionally dependent on specific secondary and tertiary conformations that can enable multi-step reactions. In addition to their catalytic activity, metals within these structures confer enhanced conformational stability to proteins (*205*). By some estimates, metalloproteins with one or more proteins at their center account for a third of all known proteins used by life (*206*). Anaerobic microorganisms generally have higher metal demands, reflective of the needs of their central biochemical pathways, and the origins of many of these pathways under anoxic conditions on the early Earth (*207*, *208*). Key examples include carbon fixation via the Wood-Ljungdahl pathway methanogenesis, and nitrogen fixation using nitrogenases (*25*, *209*). The specific metals used by microorganisms in enzymatic functions are

related to their immediate availability in the surrounding environment, selected through over 3 billion years of evolution across the diverse environments of Earth's biosphere (*210*).

While widely distributed, metals can become limiting under certain scenarios depending on factors such as their source input rate, local environmental conditions, competition, and their bioavailability. Geochemistry plays an important role as most metals are more mobile under acidic or low oxygen conditions and are generally less soluble under oxic, alkaline conditions or in the presence of reactants such as sulfide. Multi-element metal complexes serve to limit metal accessibility and when incorporated into mineral solids their accessibility is further restricted. This is highlighted by studies that frequently show environmental metal concentrations in nature significantly lower than minimum or optimal requirements for cellular function as compared to laboratory cultures (*26*). A prime example of this is trace metal limitation in the open ocean, which is known to constrain biological productivity in otherwise energy-rich locales (*211*, *212*). Consequently, biological communities have been shown to modify their metal cofactor selection in response to which metals are readily bioavailable or alternatively, metal limitations can shape individual populations and community structure through long term ecological and evolutionary processes (*213*).

Metal availability is fundamentally interlinked with virulence and pathogenesis in host-microbe systems. The type and quantity of metal can trigger intracellular signaling pathways, activate virulence mechanisms and stimulate quorum sensing that guides pathogens to their optimal niches (*214*). Multicellular organisms and other microbes exploit this as a process to regulate available metal concentrations either to interrupt infection or induce a coarse anti-microbial response through locally high metal concentrations (*215*). Other studies have demonstrated a link between metal availability and biofilm formation and have shown how the

EPS matrix can serve to accumulate metals as matrix compounds through biosorption (*216*, *217*). Hydrothermal vents represent a physically and geochemically diverse environment and one of the settings favored in theories about the origin and early evolution of life. Microbial communities have evolved within vent ecosystems to adapt to a complex and dynamic environment in relation to energy, nutrients, and metals that can further stimulate inter-species and even multi-trophic level interactions, relying on extracellular biofilms for their survival and longevity (*55*). Shared metabolites, including metal complexes, may play a critical role in the recruitment and structuring of these microbial communities.

Hydrothermal Vents and the Early Evolution of Life

Early Earth was an anoxic and hot environment with an atmosphere primarily influenced by processes associated with planetary accretion and dominated by reduced volatiles such as CH_4, H_2, CO_2, and NH_3 (*218*, *219*). Simple organic compounds were theorized to have come from meteoritic contributions, mineral-catalyzed organosynthesis reactions, and photochemical reactions, that would have generated the necessary early building blocks of life (*220*, *221*). Before the first oxygenic photosynthetic organisms appeared approximately 2.7 billion years ago, redox active metals such as Fe and S, in addition to CO_2, played major roles as electron donors, terminal electron acceptors, and metal cofactors and strongly shaped the trajectory of early evolution (*222*). This is reflected in micro-fossil and geochemical records and the most conserved regions of DNA in extant organisms.

As the early Earth was cooling, submarine hydrothermal vents were prevalent and likely played a critical role in the origins and early evolution of life. These include acidic, high temperature vents associated with magmatism, and warm, alkaline vents associated with serpentinization (*59*). Geochemical gradients and metal-adorned micro-compartments within

hydrothermal vent chimneys have been proposed to catalyze primitive biochemical reactions (*95*). Modern hydrothermal vent ecosystems provide a rich hunting ground for testing theories related to the origin of life such as essential prebiotic chemistry or abiotic compartmentalization from precipitates with FeS and NiS minerals playing a key catalytic role, as would have occurred in ancient Hadean hydrothermal systems (*60, 223*). The reactive minerals and natural gradients formed in these alkaline systems create conditions that enhance the formation of RNA oligomers (*61*). Though there is continuing debate on the sequence of processes leading to the origin of life, there is a robust and growing body of evidence placing alkaline hydrothermal systems and serpentinization as a common denominator to OOL theories due to their ubiquity and the prevalence of abiotic organosynthesis. Fossilized microbial communities, thought to have been living near hydrothermal vents, suggest that Fe and S were utilized in early metabolism, and would be a parsimonious choice due to its availability and reactivity in these dynamic systems (*71, 224, 225*). Using phylogenetic relationships to reconstruct the Last Universal Common Ancestor (LUCA) from genome sequence data highlights LUCA as an anaerobic thermophile most likely found near hydrothermal vents similar to the serpentinization-influenced, modern-day Lost City Hydrothermal Field (LCHF), and dependent on transition metals for respiration (*69*). Methanogenic Archaea, presumed to have originated early in Earth history, utilize 4 of the 9 known Ni-containing enzymes to reduce CO_2 and form CH_4 as a waste product (*226*). Additionally, biofilms of the LCHF have some of the highest percentage of transposases involved in gene replication and transfer of any natural system yet investigated, despite having very low taxonomic diversity, which may suggest an analog to early proto-metabolic processes (*193*). These adaptations are prevalent in hydrothermal systems and require a level of

cooperativity or syntrophy among these biofilms and as a result provide a rapid mechanism for acquisition of helpful function or the sharing of limiting metabolites (*33*, *161*, *227*, *228*).

Acquisition Strategies Employed by Microbes in Metal-depleted Environments

As metals are a critical part of biological catalysis and protein structure, organisms have evolved numerous mechanisms to sequester and enrich metals from the environment. These strategies became especially prominent as conditions changed on the Earth's surface limiting metal solubility, the most pronounced of which was the Great Oxidation Event which instigated a proliferation of mineral diversity (*229–231*). The most well recognized of these strategies are metal chelating compounds secreted into the environment, such as siderophores, that target specific metals. Not only do these chelators greatly amplify the solubility of metals, but they solve a second problem by aiding the transport of these large atoms across the cell membrane helping to overcome issues of toxicity or bioavailability for direct uptake (*232*). These metal chelators are often promiscuous and can solubilize and transport a repertoire of metals including Co, Cr, Mo and Ni among others (*233*). A second strategy employed by microorganisms to enrich for heavy metals is through bioaccumulation or biosorption, where the former results from direct contact between cell and metal resulting in its active uptake and the latter a passive phenomenon of metal binding to cell wall molecules such as teichoic acids, lipids, or other secreted substances (*234*). Particulate organic matter and colloids and EPS are known to contain elevated concentrations of metals in the oxic open ocean relative to the surrounding seawater that facilitate metal transport and enrichment (*49*, *235*). Similarly sessile microbial communities in biofilms may trap and redistribute metals, in some cases in a cooperative fashion as part of a complex microscale network that may depend on liberation of otherwise unavailable metals (*236*, *237*). This is one key trait of endolithic microorganisms where they bind or embed within

rock surfaces and alter the physical and chemical features at the attachment sites, creating steep gradients along the biofilm especially in highly limited and metal depleted environments (*238*, *239*). Finally, differences in metal availability directly influence protein evolution. This is best evidenced by the alternative cofactors such as Fe, Mo and V that may be used in nitrogenases, indicative of the ancient anoxic environment that they evolved within (*240*, *241*). There are clear links between nitrogenase phylogeny and geochemical changes in the early Earth that influenced metal solubility (*126*, *242*). Large scale global changes influencing metal and nutrient cycling, in addition to ongoing localized factors are likely still influencing metal substitutions and evolutionary processes to this day.

Dissolved Metals are Exceptionally Poor in Hyperalkaline Fluids, but Enriched in Precipitated Carbonates

Hydrothermal seeps and hot springs associated with water-rock reactions such as serpentinization sustain environments with strongly contrasting conditions in pH, temperature, and redox chemistry that can drive the fundamental energetic needs of life (*16*). At high pH, Ca and Mg rich, dissolved inorganic carbon (DIC) poor fluids mix with oxic surface waters, rapidly sequestering CO_2 and forming extensive travertine deposits. On the seafloor, large carbonate hydrothermal chimneys are the product of this process, as evident in known vent sites in the ocean at the Lost City and Prony Hydrothermal Fields (*21*). While strongly contrasting conditions are observed between end-member hydrothermal fluids and seawater, gradients between these boundaries are masked by a deceptively homogeneous collection of three primary minerals in the hydrothermal chimneys, calcite ($CaCO_3$), aragonite ($CaCO_3$), and brucite ($Mg(OH)_2$).

The aqueous alteration of iron-rich mantle rocks through serpentinization produces hydroxyl anions and leads to the generation of hyperalkaline fluids, commonly over pH 11. These conditions are largely unfavorable for metal mobility, as the metal content in serpentinization influenced fluids are usually at sub-nanomolar levels. However, certain metals are more enriched in ultramafic settings and more soluble in alkaline fluids such as Ni, Cr, and Co (*100*, *243*). Owing to the low metal concentrations in hyperalkaline fluids, mixing with seawater or may provide an important source of trace metals that may otherwise be unavailable in endmember serpentinizing systems. In previous studies of hydrothermal chimney formation, U and Sr have been shown to be assimilated from seawater and have been used at a bulk scale to constrain the degree of seawater mixing in chimney environments, however, other metals were not specifically investigated at a bulk scale in the earlier studies or were below detection limits (*100*). While Sr and U are not especially important metals to biochemistry, they may be a proxy for seawater mixing and the extent of trace metal availability. Gradients of temperature, pH and redox potential within vent ecosystems add further layers of complexity to metal availability and shape the metabolic landscape for associated biota. This is exemplified by a study of vent associated macrofauna at the LCHF finding enrichment of certain metals in the biomass of corals and mussels at the site (*202*).

Lost City Microorganisms are Adapted to a Low Metal Environment

Mixing between highly reducing, volatile rich hydrothermal fluids and cold, oxygenated seawater provides the energy to support dense microbial communities throughout the hydrothermal chimney structures of the LCHF, in some cases exceeding 10^9 cells per gram of material. The pathways for fluid mixing and precipitation-dissolution reactions are extensive sinuous channel networks that permeate the chimney walls. Porosity within these structures is

high, often exceeding 50% of the overall volume and decreasing with vent age. The shape and directionality of these channels varies within the vent but provides a large total surface area for biofilm attachment to occur. Microbial biofilms that line the pore spaces are encapsulated in dense extra-polymeric substances (EPS) that allow the organisms to adhere in the dynamic mixing environment and may serve as nucleation sites for mineral precipitation. In relation to metal distributions in the chimney environment, several key questions remain. Are localized metal distributions the product of mixing environments and sequential mineral precipitation? Conversely: Do microbial activities, whether through passive trapping in biofilms or active sequestration mechanisms serve to locally enrich heavy metals in the chimney matrix? These relationships can be probed through both direct observations of microbe-mineral-metal distributions, and through the genomic content of microbes within the chimney.

This study utilized a combination of fluorescence microscopy linked to mineral and elemental mapping using Raman spectroscopy and Laser Ablation ICP-MS to describe microbe-mineral-metal relationships in pore spaces of the chimney habitat at the Lost City Hydrothermal Field. We supplement this information with metagenomic data from these same samples to identify genes related to metal acquisition. Together, our observations highlight a complex microenvironment that is intricately linked to microbial activity and leaves visible and measurable traces in the vent edifice on a microscopic scale. This underlines the importance of understanding trace metal distribution in these natural systems, microbial adaptations to the trace metal availability, and its' influence on habitability within extreme environments.

Materials and Methods

Sample Collection and Preservation.

Chimney samples were collected during expedition AT42-01 in September and October 2018 aboard the R/V Atlantis using ROV Jason II by both direct grabs using the ROV arm and "slurp" samples using a vacuum-like device. Each sample occupied its own container during the dive to avoid cross contamination and was continuously monitored in real time by video camera during sampling. Where possible *in situ* temperature and pH measurements were captured from the associated venting fluids using an ROV mounted probe. Shipboard, chimneys were aseptically subsampled into smaller sizes and volumes and stored in sterile Falcon tubes or Whirlpaks for long-term preservation. For this study, samples were prioritized for their structural integrity to ensure maintenance of the overall *in situ* organization of pore structure and biological material. The resulting sample lots were preserved in a 2-4% paraformaldehyde solution in 1× Phosphate Buffered Saline buffer, followed by washes and storage in 70% ethanol at 4℃ until processing. Parallel subsamples were also collected and frozen at –80℃ for DNA extraction and shotgun metagenomic analyses, as described in an earlier study (Alian et al., in review).

Embedding and Sectioning

For microscopic/spectroscopic analyses, samples of interest were further subsampled to fit within a 2.0 ml microcentrifuge tube. Samples were dehydrated in a gradual series of ethanol washes (30%, 50%, 70%, 100%) for ~1 minute in each bath. Following dehydration, samples were incubated in a premixed 1:1 mixture of LR-white resin (Electron Microscopy Sciences) and ethanol for at least 18 hours at 4℃. After incubation, the mixture was removed and replaced with a premixed 2:1 mixture of LR-white and ethanol for at least 18 h at 4℃. Subsequently, samples were incubated in pure LR-white resin for at least 18 h at 4℃. Then, samples were maintained at

room temperature (20-25°C) for 3 hours, followed by a final LR-white volume change with room temperature LR-white resin. After the volume change, samples underwent vacuum degassing at a rate of 1 inHg sec^{-1} for both depress and repress to ensure complete resin penetration of the sample and prevent inadvertent bubble formation. Samples were cycled and maintained under vacuum until bubbles were no longer visibly emanating. After vacuum degassing, samples were incubated at 60°C for at least 24 hours for hardening.

After polymerization, the microcentrifuge tube was removed leaving the hardened sample which was then indexed with notches along its length for easy visual reference between the resulting sections. Using a 0.65-micron diamond wire or diamond-coated Dremel saw wheel, transverse sections ~1mm in thickness were cut. Sections were smoothed and polished in a series of wet steps to a uniform finish. A CarbiMet SiC Abrasive Paper (320/P400 Grit, Buehler product number 36-02-0320) was placed on a flat surface and wet with DI water and the section smoothed in small evenly pressured circular motions to remove any rough topography from the initial cutting and create a flat plane. A surface of uniform opacity, free of gouges or major scratches was considered sufficiently planed. This step was repeated with increasing grit discs (400/P800, 800/P1500, 1200/P2500, Buehler product numbers 36-02-0400, 36-02-800 and 36-02-1200, respectively) ensuring uniform smoothness and reflective finish at each step. A final polish to a mirror finish was done using a dry MicroCloth Polishing Cloth (product number 821-3). Sections were washed with DI water to remove any dust or debris and lightly patted dry with a Kimwipe. Final sections had ~200-micron thickness, with most material removed during the initial low grit smoothening steps.

Raman Spectroscopy

Raman measurements were conducted using a Horiba LabRAM HR Evolution Raman spectrometer equipped with a 532 nm, 100mW frequency-doubled Nd:YAG laser excitation source, 600 mm^{-1} diffraction grating, 256 × 1024 pixel CCD detector, and 50× microscope objective (N.A. 0.75) at the University of Colorado. A laser power of 100% was applied at a 5 µm lateral and 5 µm vertical step size in sample areas of interest using a 0.25 second spectral acquisition time and 1 accumulation each. Spectra were collected from 50 cm^{-1} to 1800 cm^{-1} by integrating the counts in the undiffracted, 256-pixel direction of the detector, such that each spectrum contains 1024 points. Resulting spectra were corrected using a 6th order polynomial baseline using LabSpec 6 software (Horiba Scientific, Inc.). Models showcasing Raman map spectral components were created using Classical Least Squares (CLS) fitting in LabSpec 6.

Staining and Fluorescence Microscopy, and Image Analysis

Sectioned, embedded samples were stained with DAPI (4', 6-diamidino-2-phenylindole) (Ex355nm / Em460nm) targeting DNA for microbial cell visualization and imaged using a Leica Stellaris 5 While Laser Confocal Microscope and excitation diode 448nm at the Michigan State University Core Microscopy facility. Images were collected with a Plan Apo 63× oil immersion objective (NA 1.40) and stitched into a mosaic of 1024 px^2 tiles to cover the sample region(s) of interest. The mosaic was created during acquisition using the Leica LAS X software. Complete mosaics were processed using FIJI/ImageJ 2.14.0 and analyzed using QuPath 0.5.0 for cell counting, mineral distribution and porosity information (the latter two using Raman maps and a trained pixel classifier within QuPath).

Laser Ablation ToF/ICP Mass Spectrometry

A 10% w/v gelatin calibration standard was created using Porcine gelatin with 300 bloom strength. A 1000 µg/ml multielement standard containing Ca, K, Ba, B, Cr, Cu, In, Pb, Mn, Ag, Sr, Zn, Mg, Al, Bi, Cd, Co, Ga, Fe, Li, Ni, Na, Tl (IV-Stock 4 solution in 5% v/v nitric acid) was added to 8 ml ultrapure deionized water (18.2 M Ohm @ 25C) in a 65°C water bath followed by the addition of 1g of gelatin (Sigma Aldrich, Cat No. G2500-500G). The standard was mixed gently using metal free plastic spatulas and degassed in an ultrasonic water bath at 65°C to remove any air bubbles and keep gelatin liquid. The stock standards were subsequently diluted in fresh 10% w/v gelatin and ultrapure deionized water to make 50, 25, 12.5, 6.25 and 3.125 ng/g solutions of elements. 20 µl drops of the gelatin dilutions were placed on preheated glass microscope slides, covered with petri plates and dried in a heated incubator until solid. Resulting gelatin deposits were circular and flat.

Sectioned sample slides and gelatin standards were loaded in a Bioimage-266 nm laser ablation system (Elemental Scientific Lasers, Bozeman, MT, USA) coupled to an icpTOF S2 (TOFWERK AG, Thun, Switzerland) ICP-ToF-MS. The system was sealed and purged for 5 minutes after which the analytical regions of interest were mapped. 9 lines were selected across each gelatin standard and a blank using the same acquisition parameters as the sample of 5 µm circular laser spot size, 50% laser power and 125 Hz repetition rate with no gaps between laser spots. This allowed ablation of the whole analytical area without overlap to confound acquired data. This analytical region was created to encompass the entire visible chimney sample within the resin section to minimize acquisition time and instrument drift, allowing for an even plane of ablation across the region of interest.

Metagenomic processing and statistics

Genomic analyses were carried out on chimney samples and processed as described earlier and in previous studies but will be summarized here in brief (*85*, *132*, *135*, *137*). DNA was extracted using a FastDNA SPIN kit (MP biomedical), followed by size-selected metagenome library construction and paired-end sequencing at the University of Utah High-Throughput Genomics Core Facility using a NovaSeq 600 instrument. Sequences were trimmed of adapters, cleaned of low-quality reads and predicted protein sequences derived from the KEGG release 83.2 database. The coverage of predicted KEGG annotated proteins was calculated as Transcripts Per Million (TPM) using the seq-annot package and normalized against the total number of read pairs in the library. A search for metal substrate binding, storage or responsive genes was carried out to filter on KEGG predicted sequences of interest to our study and were retained for further analysis on presence between sites. Differences in gene counts between sites were examined using ANOVA aov function in R version 4.2.2, followed by Tukey-HSD post-hoc test for each gene of interest with significance ($p < 0.1$) using the TukeyHSD function in R. Results were visualized using the Rpackage ggplot.

Results and Discussion

Biofilms are primarily associated with brucite-lined surfaces within the LCHF chimneys.

In all the samples examined, most biofilms were found attached to brucite-lined pore spaces, indicative of recent contact with hydrothermal fluids. This contrasts with a sparse distribution of cells found at interfaces between pore space and aragonite- or calcite-enriched regions. The detection of brucite showed several different physical characteristics that appear related to proximity of identified microbial cells. While brucite naturally precipitates as vent fluids interact with seawater, evidence suggests this process may be further catalyzed by

microbial activity impacting its mineralization particularly under changing pCO_2 and increased alkalinity of the surrounding fluids (*244*). Most biofilms were generally found to be rather thin, planar structures blanketed across the mineral interface (**figure 10**). This resembles the classical form of monolayer biofilms under the shear forces of fluid flow, as would be expected within venting pathways of the chimney and may organize with the flow direction (*245*). While no direct measurements of fluid flow rates are available at LCHF, venting through the chimney walls is primarily diffuse and results from the buoyancy of heated fluids convecting out of the system. Chun, et al. demonstrate a relationship between flow speed, shear flow stress and biofilm thickness in line with biofilms observed in our Lost City samples and pointing to the same range of flow speeds of approximately 0.2 m/s (*245*). In some channels within the chimneys, planar biofilms can be observed with varying thickness and cell density. This qualitatively shares many of the same observable characteristics as other venting fractures and seeps seen in the Mid-Atlantic Ridge where measured vent flow rates range from 0.0001 m/s to 0.15 m/s (*57*). Flow conditions influence the shape of biofilm structures, nutrient access and diffusion within the overall system (*246*). In other systems, flow conditions provide a mechanical signal stimulating downstream biochemical processes that enhance EPS production, further increasing or decreasing biofilm formation and increasing the use of key signaling molecules such as cyclic-di-GMP. Notably, under some conditions, increased shear stresses from higher flow rates may inherently increase biofilm density which may select for more conditionally adapted species (*51*). Direct flow measurements and studies in the future would be critical to understanding the myriad physical signals biofilms use for colonization and growth within the chimney system but are beyond the current study.

Within some venting pathways, EPS strands occur as part of larger networks that have precipitated a series of brucite grains, one after the other and overlying the surface they attach to (**figure 10B**). The effect on vent channels becomes readily apparent where many surfaces are predominantly covered with biofilm cells while others appear very rough and contain an irregular and granular layer. Within many of the observed flow paths, microbial networks span the channels wall to wall. The most recent studies examining mineral formation at Lost City highlight the centrality of brucite precipitation in early and young venting chimneys (*133*). Aquino, et al demonstrate extensive brucite mineralization associated with biofilms imaged on brucite faces. These mineralized brucite targets exhibited a rough appearance possibly lining up with EPS strands formed by biofilms, in contrast to the smooth brucite linings found elsewhere in the vent chimney. Our embedded samples preserved biofilm attachments and the approximately *in situ* position they occupied allowing an examination of the channel spanning microbial networks that would otherwise be destroyed or removed by other microscopy techniques. Similar patterns of putative brucite biomineralization were identified by Pisapia et al at the Prony Bay Hydrothermal Field, a Lost-City type hydrothermal vent system in New Caledonia sharing many of the same key characteristics including microbial filaments associated with brucite mineralization in close proximity to diverse cell aggregates (*180*). Carbonate mineralization is a common observation in nature, and biologically induced magnesium carbonate in particular has been studied as a byproduct of bacterial autotrophic metabolism (*183*, *247*, *248*). Sulfate reducing bacteria have been shown to adsorb high amounts of magnesium into the EPS and catalyze the precipitation of magnesium-carbonates and magnesium hydroxide (brucite) during active metabolism, while the mineralogy of such carbonates may evolve over the lifetime of biofilms during formation of microbialites in alkaline environments (*249–251*). Very

little research has focused on the underpinnings of microbially mediated brucite precipitation in the deep sea, and this represents a gap in our knowledge on microbe-mineral formation processes. A much more active involvement of brucite may contribute to microbial activity and in the alkaline reducing conditions found in serpentinizing systems such as Lost City, further facilitating microbial metabolism that would further stabilize a solid brucite phase over time (*252*).

In two instances, we observed elevated fluorescent signals in aragonite (**IMAX internal, figure 11**) and brucite (**Marker 3, figure 12**) with only the latter co-associated with a unique biofilm. The entirety of the Marker 3 fluorescent surface is covered with what appears to be a single type of filamentous microorganism anchored to the brucite and growing into the pore space. Lodged within this channel is a non-fluorescent brucite granule devoid of these growths. Adjacent to it is a denser biofilm hotspot that nearly connects it to the nearby vent wall. Within this region, a brucite signal is detected with weak fluorescence. The filamentous community appears to grow in a radiating pattern outward from the surface of rounded brucite regions. Interestingly this radiating pattern also appears within the brucite matrix, indicating a continuous mineral growth catalyzed by what could be a stable process within this specific region. This combination of filamentous microbes growing from a rounded brucite surface can be found in other areas in our samples, but without the fluorescent signal.

Frequently in our study and others we encounter significant brucite autofluorescence that hitherto has been inexplicable though our and others' observations show consistent evidence of interlinkage between the brucite matrix and any co-associated microbial communities. Aquino et al observed similar fluorescence patterns in samples from the same expedition, with indications relating brucite crystal structure to an influence from the proximal or attached biofilms (*133*).

Brucite has been noted to have greater absorption properties for nucleic acids, peptides, and metals under hydrothermal conditions driven by the mineral's charge properties (*253–255*). The surrounding microenvironment of microbial cells may itself be highly regulated, with stark gradients between internal biofilm and EPS phases and the external environment in pH and composition, which logically may contribute to even more localized dissolution and precipitation reactions (*256*). As cells attached to growing chimneys, the production of EPS components in addition to the normal cellular metabolic processes create a source of concentrated organic molecules in direct contact with a locally absorptive mineral surface. The fluorescent brucite layer found in Marker 3 shows a unique botryoidal pattern of precipitation not seen in any other samples from Lost City and may be linked to the properties of associated biology and the local microenvironmental conditions within this pore space. An examination of the microbe influenced dissolution-precipitation dynamics that can lead to these patterns is warranted although it is beyond the goals of the current work. Furthermore, there is a clear need to understand the contributors to mineral fluorescence in the context of these complex systems and historical works show organic inclusions, metal deposits and redox state contributing to fluorescence in minerals and carbonates such as aragonite (*257*).

Within the same Marker 3 sample, we observe in an aragonite dominated channel a dense and morphologically diverse community, anchored by what appears to be an organized filamentous microbial web resembling a hive (**figure 13**). The structure covers the entire space within the channel with cells primarily residing along the EPS webs. Interspersed within this hive are a significant number of microbial sheaths with a higher density of both features concomitant with an observed Raman signal for carotenoids (**figure 13A**). Within this high-density cell region, many sarcinal-shaped aggregates line the walls. The morphology and density

of these aggregates is suggestive of them being the eponymous Lost City Methanosarcinales (LCMS) previously identified as the dominant archaeal species at this site (**figure 14**). It can also be identified within an aragonite rich particle containing a highly dense microbial mass (**figure 15**). One portion of this aragonite mass contains a significantly sized sarcinal aggregate that may overlap with a carotenoid signal. Carotenoids and LCMS were not seen in any other regions in our samples and is possibly unique to this specific consortium and possibly LCMS. The exact identity of the carotenoid(s) comprising the Raman signal are unknown, however their presence is in line with other observations of non-phototrophic marine organisms utilizing them as part of a robust stress response (*258*). An array of carotenoid types have been implicated in the thermal stability of enzyme complexes, membrane integrity, pH tolerance and resistance to oxidative stress; all challenges that can be found across environmental gradients in Lost City (*259–261*). Within our samples, this is the only aragonite associated biomass of high density that is observed. This region contains variable minor mixtures of brucite and calcite indicating the venting environment remains dominated by hydrothermal fluids but decreased with a minor influence seawater. As a result, communities may exist within a transition region forming a microbial island within the edifice, which would explain the apparent organization around EPS hives as we as the diversity of cells. While we cannot ascertain any degree of cooperativity within this community, the structure of cells is suggestive of syntrophic interactions reminiscent of those found in marine sediments and seeps.

Metal enrichments are linked with microbial occurrence within pore spaces.

The overall chemical environment within the LCHF chimneys varies depending on the sample and its venting history. Metals were detected within the mineral matrix in all samples, with local maxima often found in the brucite-enriched lining of pore spaces where cells were

located. The concentrations of cobalt, copper, manganese, molybdenum, nickel, uranium and zinc were measured, with average sample and microbial hotspot values summarized in **table 6** and **table 7**. Cells were manually annotated and counted within the mapping area to generate density maps, revealing the heterogeneous population geography along vent walls in comparison to a heterogeneous mineral environment, as characterized by Raman (**figure 16**). This approach provided a constrained region for further analysis, avoiding assumptions about cell distribution typical in traditional cell count methods and accounting for the unseen data in what is a three-dimensional sample examined along a two-dimensional subsection. Hotspots were annotated and carried forth in further metal analyses in both the IMAX transect (**figure 17**) and remainder of samples (**figure 18**), which can be referenced for the subsequent discussion.

Cobalt concentrations ranged from 0 to 2.82 ppm, generally low but higher than in vent fluids or seawater (*100*). The IMAX transect, especially IMAX Top, showed noticeable cobalt occurrence primarily confined to the aragonite mineral matrix . Hotspots in IMAX had variable cobalt concentrations compared to the sample average, mainly along the aragonite phase. Marker 3 had an average cobalt concentration of 0.73 ppm within the aragonite phase, with microbial hotspots ranging from -0.47 ppm (negative due to regression extrapolation) to 1.22 ppm, averaging 0.49 ppm. Eastern Wall sample B had the highest measurement at 2.82 ppm in the aragonite phase with microbial hotspots averaging 5.11 ppm. Sample A and Sombrero had nearly undetectable cobalt signals, except for a single hotspot in Sombrero. Marker 8 showed a different trend with a higher hotspot of 2.60 ppm that was only associated with brucite. Cobalt incorporation into the aragonite mineral matrix may result from increased interaction with seawater during precipitation (*262*). The varied concentrations of cobalt across different samples, especially the higher levels in the aragonite phase suggest a combination of both seawater

contribution in addition to microbial activity. The higher cobalt levels in the IMAX transect, particular at the top (and the most seawater exposed) and the significant concentrations in Eastern Wall samples which are inactive veins align with previous findings indicating the preferential incorporation of cobalt into aragonite within a mixture of hydrothermal and seawater input, possibly due to fresh precipitate adsorbing cobalt immediately from vent fluids (*263*, *264*).

The *cbiN* gene, involved in cobalt uptake, was found significantly higher in Sombrero compared to Marker 9 (**figure 19**, $p < 0.1$). This suggests site-specific adaptations to cobalt availability, with microbial communities at Sombrero potentially developing more efficient mechanisms for cobalt uptake. This adaptation is likely driven by local geochemical conditions that influence its bioavailability, with evidence suggesting increased bioavailability on ancient Earth under much different redox conditions than today (*265*). Cobalt is an essential trace element for many microorganisms, serving as a cofactor in key enzymes such as vitamin B12, also known as cobalamin (*266*). The observed patterns can be suggestive of microbial communities actively participating in the biogeochemical cycling of cobalt that is further impacted by the high pH and temperature regimes found in LCHF vents that would influence its speciation and availability.

Copper concentrations varied from 0.07 to 3.24 ppm. The IMAX transect showed the highest copper content at the bottom, with distinct patterning found in the top sample associated with microbial cells and brucite surfaces. Planar biofilms in these areas had brucite-associated copper signals averaging 1.16 ppm, with HS1 and HS2 showing the highest signals at 1.61 and 2.26 ppm respectively. The internal IMAX sample had a nearly uniform copper distribution averaging 0.92 ppm, with enrichments in brucite areas with associated biofilm. Marker 3 had the highest average copper content at 3.24 ppm, with the highest concentration in a calcite region.

Sombrero's copper signals were associated with brucite overlapping with biofilms and showing the lowest overall average signal at 0.18 ppm. Eastern Wall A and B showed copper associated with brucite and aragonite needles, with higher hotspot signals averaging 1.31 ppm. The copper distribution patterns indicate a strong association with brucite surfaces and microbial biofilms, particularly in the IMAX transect. The detection of high copper concentrations in microbial hotspots suggests that microbes may play a role in concentrating copper in these niches. This aligns with the known copper-binding capacities of microbial biofilms through their organic secretions or complexations and the potential for copper to serve as a cofactor in multiple enzymatic processes essential for microbial metabolism in extreme environments (*101*, *267*).

The presence of *cusA/silA* and *ycnJ* genes, associated with copper efflux and binding, respectively, reflect the microbial need to regulate copper concentrations, particularly under limiting conditions (*268*, *269*). The detection of *ycnJ* was significantly higher in Marker 8 compared to Marker 3 (**figure 20**, $p < 0.1$), indicating a higher capacity for copper binding in Marker 8 but no statistically significant difference in *cusA/silA* detection, though there is a trend towards higher presence in Sombrero over Marker 3. *ycnJ* expression increases under copper starvation, and its heightened appearance in Marker 8 tracks with it having the lowest copper signal of the three, with the microbial hotspot average slightly higher than baseline. This gene's detection patterns mimic copper distribution in the samples, highlighting the possible effects of microbial presence on localized copper cycling. Copper is critical for various cell functions, including electron transport and oxidative stress response, but can also induce significant stress and toxicity on microbes. The detection of copper transport and binding genes in hotspots suggests that microbial communities at LCHF actively manage copper concentrations in addition to their sequestration for use in key metabolic pathways.

Iron content ranged from 0.48 to 13.87 ppm, with a moderate increase towards the top of the IMAX transect. Eastern Wall A and B showed isolated hotspots with increased iron levels, averaging 4.20 and 13.87 ppm, respectively. Marker 3 had similar patterns with higher microbial hotspot measurements. The iron content showed a moderate increase towards the top of the IMAX transect, with some signal hotspots overlapping with microbial hotspots, particularly in Eastern Wall samples. The observed patterns suggest that iron is highly variable from vent to vent though the carbonate matrix is historically considered iron-poor (*100*).

Iron is one of the most important and vital elements for many metabolic processes including respiration, DNA synthesis and central to many enzymatic cofactors. We examined the presence of four iron uptake genes finding no significant differences in their expression between the three sites (**figure 21**). However, all four showed relatively high presence in all three vents indicating robust iron cycling activity taking place, the highest of which being *afuA*, encoding for an iron(III) substrate binding protein, and the second highest being *feoA* coding for an iron(II) substrate binding protein (*270*, *271*). Our analyses do not distinguish between iron oxidation states, but the degree of differential abundance between each of these genes points to a greater utilization of one over another. Microbial iron(III) reduction can be coupled to organic matter degradation, direct electron transfer, and its utilization as an electron shuttle under alkaline conditions, which may explain its perceived preference for expression (*272–274*). *sitA* and *troA/mntA/znuA*, coding for combined manganese / zinc / iron binding and transport showed much lower expressions and may reflect a degree of adaptability to metal scavenging.

Manganese measurements ranged from 0.23 to 1.58 ppm. IMAX samples generally had low manganese content, with the internal sample enriched on one side of the brucite vent interface. Marker 3 had moderate enrichments in brucite. In Sombrero, manganese signals were

contained within brucite faces with enrichments overlapping with microbial networks. Marker 8 showed manganese within a brucite layer overlapping with a microbial hotspot.

The gene *mntC*, involved in manganese substrate binding, showed significantly higher expression in Sombrero compared to Marker 3 (**figure 22**, $p < 0.05$). *ABC.MN.S*, a combined manganese/iron substrate binding product showed similarly low levels of expression, with no significant differences between sites. This suggests that microorganisms in Sombrero may have focused mechanisms for manganese uptake, which could supplement resistance to oxidative stress in addition to supplying various enzymatic functions. Frequently observed discoloration of the white carbonates at LCHF is attributed to the increased presence of manganese-oxides, which may be further stabilized within the system by the high pH environment and be more accessible to microbes in addition to manganese precipitates being further catalyzed by biofilms formations.

Molybdenum concentrations primarily detected in the aragonite matrix across all samples showed a slight increase from top to bottom in the IMAX transect. Marker 3 had the highest average concentration of 5.29 ppm in enriched regions. Sombrero had limited molybdenum signals on venting surfaces, with low signals in Marker 8 and Eastern Wall samples. The distribution of molybdenum primarily in the aragonite matrix, with higher concentrations in internal samples has been previously simulated to occur primarily surfaces of areas examined and exhibiting greatest stability in aragonite when primarily incorporated as a molybdate molecule (*275*). Molybdate is the most bioavailable form of molybdenum and examining the three detected genes for molybdate transport and storage, no significant difference between sites was detected (**figure 23**). However, *modA*, coding for molybdate substrate binding and *mosAB*, coding for molybdate storage, showed relatively high expressions overall, comparable to iron and copper uptake expression discussed earlier. Molybdenum's criticality as a cofactor for

nitrogenases in addition to iron, belies its significant uptake and storage potential (*276*, *277*). Marker 3 contained the highest molybdenum signals of all three sites, but the wider and higher range of *mosAB* in Sombrero and Marker 3, showing much lower molybdenum signal detection points to a possible molybdenum limitation response which has also been shown to cause increased expression of *modA* (*278*). While much lower in expression, the tungstate/molybdate transporter *wtpA* also shows a similar pattern to *mosAB*, indicating an additional uptake mechanism targeting molybdenum, since nearly no tungsten was detected in any of our samples (data not shown).

Nickel concentrations were higher in IMAX samples, particularly the top portion at 15.83 ppm, associated with microbial hotspots and the previously described brucite pearls. Marker 3 had dispersed nickel signals, with a positive detection in the calcite-associated HS3. Sombrero had low average content overall at 0.17 ppm, with a single hotspot measuring 0.21 ppm associated with brucite. Marker 8 and Eastern Wall samples showed sparse signals, with enrichments overlapping microbial hotspots on brucite interfaces. Higher nickel concentrations in the top segment of the IMAX transect, associated with microbial hotspots and brucite pearls, suggest a co-occurrence between nickel presence and microbial mediated brucite precipitation. This may occur as a byproduct of methane production and / or nitrogen fixation where microbial brucite precipitation occurs. The *nrsD* gene, associated with nickel resistance, showed significantly higher expression in Marker 8 compared to Marker 3 ($p < 0.05$), though at overall lower expression levels than the nickel transport genes *nikA* and *cbiK* (**figure 24**). Nickel has been shown to variable incorporate into aragonite and carbonates, in addition to cobalt, with a potential for indicating precipitation rates, though its overall presence at Lost City remains low

but increases with seawater input and decreasing venting activity, making it another potentially limiting element where microbes reside in the primary venting regions (*100*, *264*).

Uranium signals were generally confined to brucite regions in IMAX samples, decreasing down the transect. Marker 3 had extensive uranium signals along aragonite surfaces and calcite boundaries, with the highest microbial hotspot signal. Zinc signals were prevalent in brucite and brucite pearls, with higher signals in microbial hotspots than average sample measurements. The highest zinc concentration was in the calcite-associated HS3 of Marker 3, measuring 82.68 ppm. The confinement of uranium signals to brucite regions and the prevalence of zinc in brucite pearls and microbial hotspots underscore the selective incorporation of these metals into specific mineral phases. The high zinc concentrations in microbial hotspots, particularly calcite-associated regions, suggest that microbes might facilitate zinc concentration and sequestration in these areas. The *tlyC* gene, which encodes for a zinc and cobalt efflux system, showed significantly higher expression in Marker 8 compared to Marker 3, though detections were limited across the three samples (**figure 25**, $p < 0.1$). This suggests however a degree of microbial communities actively exporting excess zinc and cobalt that is being captured by the mineral surroundings. Zinc is ever-present and is an essential element for many enzymes and structural components, making the element's high concentration in the mineral matrix notable and is reflected by the relatively high detection counts of *znuA* zinc uptake genes indicating its high requirement (**figure 26**).

Biogeochemical dynamics are intricately linked at the microbe-fluid-mineral interface

Our study maps for the first time the intricate relationship between biology and its physical microenvironment within the extreme and dynamic environment of the Lost City hydrothermal vents. We identify unique microbial assemblages that structure their distribution in

highly organized ways, interacting dynamically with the mineral surfaces they attach to. Within these environs, microbial activity further impacts the formation and composition of carbonate mineral precipitation, creating a highly complex interconnected system of biotic and abiotic features. Site specific-detections of metal-cycling genes provides insight into the microbial adaptations and the roles of microbes in biogeochemical cycling within these unique environments. Heavy metals, including cobalt, copper, manganese, molybdenum, nickel, uranium and zinc were detected within the mineral matrix of all samples, with local changes often found specifically in the brucite-enriched lining of pore spaces where microbial cells were most densely concentrated. The heterogeneity in metal concentrations across different samples underscores the complexity of these hydrothermal systems. For instance, cobalt was predominantly found in aragonite phases of limited microbial presence, while copper was closely associated with brucite surfaces and microbial biofilms. This suggests that microbial activity can significantly influence the distribution and incorporation of metals in mineral phases, but also can dictate where microbes take root and thus constrain the range of metabolism possible due to their metal cofactor limitations. The differential presence of metal-binding and transport genes further highlights these limitations across the hydrothermal field due to their variations in expression across different samples. This highlights the small environmental niches that form where microbial adaptations have taken place due to the local metal concentrations.

This was not an exhaustive analysis of all the metal or gene distributions and represents a first order survey to highlight the importance of considering the direct microbial microenvironment in understanding the biogeochemistry of these extreme sites that must consider limitations within this study. Existing data shows that there is a high variability in the geochemical environment of Lost City, which could result in more heterogeneous distributions

of metals and microbes making identification of consistent patterns between samples difficult. The dynamic conditions of the LCHF characterized by pH, temperature, and redox gradients inherently require microbial communities to continually adapt to fluctuating geochemistry. This adaptive process would further involve regulatory pathways and functional redundancies in nutrient uptake and resistance mechanisms. This can lead to diffuse gene detection patterns that are difficult to detect statistically or may altogether fall out of significance. We observe the presence of multiple metal-binding and transport genes in microbial genomes suggesting the possibility of functional redundancy. This is a common feature in microbes where less efficient processes may be employed due to their inherently greater stability under more extreme conditions such as thermal stability or pH tolerance. This redundancy, while advantageous for microbes, complicates identification of significant differences in gene expression and requires higher throughput sample collection and processing. The remote location of Lost City coupled with the difficulty of collecting many intact fragile samples from a kilometer below the sea creates a mosaic of challenges that are further exacerbated by variable success in DNA collection and sequencing for downstream analyses, and so this study serves as a methodological approach to deeper contextual analysis with a multiplicity of toolsets. Further functional analyses of metal cycling, microbe-mineral precipitation processes and the microbial community response to varying geochemical conditions will serve to better clarify not just the adaptive mechanisms employed by these organisms, but also the evolutionary pathways they undertook to survive over billions of years in the most ancient environments that persist on Earth today.

Tables

Table 5 - Samples used in this study, with their IDs, location, calculated mineral area percentage and estimated porosity in addition to the highest measured fluid temperature and pH where available.

Main Sample ID	Sample ID	Location	Aragonite %	Brucite %	Calcite %	Porosity %	Latitude	Longitude	Depth (m)	Highest Temp. (°C)	Highest pH
1107-1723	LC03281	Marker 3	66	14	19	30	30.1205071	-42.1243435	729.69	85	9.4
1107-2314	LC03277	Marker 2 / IMAX Top	49	45	6	48	30.1204803	-42.1241987	762.24	63.9	-
1107-2314	LC03280	Marker 2 / IMAX Internal	55	44	1	51	30.1204803	-42.1241987	762.24	63.9	-
1107-2314	LC03279	Marker 2 / IMAX Bottom	40	60	0	55	30.1204803	-42.1241987	762.24	63.9	-
1108-1211	LC03282	Eastern Wall	43	37	20	56	30.1240043	-42.1192428	839.19	-	-
1108-2301	LC00940	Eastern Wall	62	0	38	26	30.1245919	-42.1193596	797.97	-	-
1109-0743	LC01375	Sombrero	28	52	20	58	30.1240569	-42.1195469	761.73	74.4	9.3
1110-0603	LC01808	Marker 8	0	100	0	51	30.1204756	-42.1249187	801.24	49.1	10

Table 6 - Average elemental content of chimney samples as a function of the averaged area measurements for each respective element.

Main Sample ID	Sample ID	Location	Co59 (ppm)	Cu63 (ppm)	Fe56 (ppm)	Mn55 (ppm)	Mo95 (ppm)	Ni60 (ppm)	U238 (ppm)	Zn66 (ppm)
1107-1723	LC03281	Marker 3	0.73	3.24	8.65	0.61	5.29	-0.02	1.08	30.25
1107-2314	LC03277	Marker 2 / IMAX Top	0.51	0.49	0.95	0.23	0.32	15.83	5.01	0.00
1107-2314	LC03280	Marker 2 / IMAX Internal	0.68	0.07	0.69	0.80	0.37	0.00	9.81	5.96
1107-2314	LC03279	Marker 2 / IMAX Bottom	0.65	2.87	0.48	0.31	1.55	0.31	10.41	0.00
1108-1211	LC03282	Eastern Wall A	0.00	0.45	2.73	0.48	-0.11	1.32	0.03	9.08
1108-2301	LC00940	Eastern Wall B	2.82	0.56	13.87	0.59	-0.06	0.35	0.00	1.85
1109-0743	LC01375	Sombrero	0.04	0.36	0.87	1.58	0.07	0.17	0.05	4.19
1110-0603	LC01808	Marker 8	1.51	0.18	1.37	0.54	-0.12	0.04	0.09	3.58

Table 7 - Elemental measurements over regions of microbial density hotspots corresponding with each site and identifying the primary mineral at that region as detected by Raman.

ROI	Interfacial Mineral	Co59 (ppm)	Cu63 (ppm)	Fe56 (ppm)	Mn55 (ppm)	Mo95 (ppm)	Ni60 (ppm)	U238 (ppm)	Zn66 (ppm)
Eastern Wall B HS1	Aragonite	5.16	1.39	35.09	1.20	-0.13	0.60	0.00	4.30
Eastern Wall B HS2	Aragonite	8.89	2.87	49.61	0.87	0.16	0.89	0.00	6.16
Eastern Wall B HS3	Calcite	2.02	0.24	11.37	0.42	-0.11	0.10	-0.01	1.11
Eastern Wall B HS4	Aragonite / Calcite	4.39	0.75	26.84	2.07	-0.05	0.34	0.00	2.84
Eastern Wall B HS Average	***	**5.11**	**1.31**	**30.73**	**1.14**	**-0.03**	**0.48**	**0.00**	**3.60**
Marker 3 HS1	Aragonite / Calcite	1.22	1.85	9.05	1.13	3.02	-1.21	0.95	33.43
Marker 3 HS2	Brucite	-0.47	1.13	5.35	0.13	1.18	-3.93	1.16	19.30
Marker 3 HS3	Calcite	1.09	6.63	8.34	4.41	7.57	1.60	4.41	82.68
Marker 3 HS4	Brucite	0.12	3.36	7.41	0.10	5.96	-0.75	1.33	30.90
Marker 3 HS Average	***	**0.49**	**3.24**	**7.54**	**1.44**	**4.43**	**-1.07**	**1.96**	**41.58**
Eastern Wall A HS1	Brucite	0.07	0.79	3.82	1.00	0.14	1.64	0.10	17.08
Eastern Wall A HS2	Brucite	0.10	0.30	2.35	0.89	-0.20	0.61	0.08	14.17
Eastern Wall A HS3	Aragonite	-0.02	0.22	1.03	0.37	-0.23	-0.05	0.01	8.14
Eastern Wall A HS4	Aragonite	-0.04	0.52	7.74	0.35	0.01	4.57	0.02	7.67
Eastern Wall A HS5	Brucite / Calcite	-0.01	0.69	5.39	0.71	-0.09	1.44	0.05	11.26
Eastern Wall A HS6	Brucite	0.06	0.85	5.61	0.62	-0.14	1.87	0.06	15.17
Eastern Wall A HS7	Brucite	0.05	0.74	3.46	1.31	0.01	1.02	0.07	35.46
Eastern Wall A HS Average	***	**0.03**	**0.59**	**4.20**	**0.75**	**-0.07**	**1.58**	**0.05**	**15.56**
IMAX Top HS1	Aragonite	1.13	1.61	10.97	0.33	0.31	0.52	0.08	18.77
IMAX Top HS2	Brucite	0.50	2.26	9.01	0.70	0.72	1.07	0.70	36.22
IMAX Top HS3	Brucite	0.07	0.62	3.10	0.60	0.16	0.64	0.87	29.20
IMAX Top HS4	Brucite	0.07	0.62	4.34	0.64	0.17	0.69	1.08	15.17
IMAX Top HS5	Brucite	0.03	0.66	3.44	0.44	0.07	0.52	0.55	13.47
IMAX Top HS Average	***	**0.36**	**1.16**	**6.17**	**0.54**	**0.29**	**0.69**	**0.65**	**22.56**
IMAX Internal HS1	Aragonite	0.24	1.78	7.88	1.92	2.89	1.54	2.53	42.57
IMAX Internal HS2	Brucite	0.14	1.00	2.62	1.02	1.79	0.87	1.55	24.58
IMAX Internal HS3	Brucite	0.33	1.08	21.04	0.87	3.27	1.32	1.59	26.05
IMAX Internal HS4	Brucite	0.03	0.44	3.79	0.62	0.51	0.47	0.49	13.17
IMAX Internal HS5	Brucite	0.06	0.68	3.93	0.99	0.22	0.22	0.47	10.34
IMAX Internal HS6	Brucite	0.00	0.50	2.15	0.66	0.21	0.31	0.34	8.19
IMAX Internal HS Average	***	**0.13**	**0.92**	**6.90**	**1.01**	**1.48**	**0.79**	**1.16**	**20.82**
IMAX Bottom HS1	Brucite	0.11	0.34	3.20	0.64	-0.27	1.84	0.45	8.31
IMAX Bottom HS2	Brucite	0.01	0.40	2.32	0.62	-0.20	1.09	0.58	7.99
IMAX Bottom HS3	Brucite	0.14	1.47	9.96	0.86	0.46	3.35	0.50	25.55
IMAX Bottom HS4	Brucite	0.19	0.58	3.11	1.03	1.86	2.43	0.77	16.06
IMAX Bottom HS5	Brucite	0.10	0.83	4.37	0.65	-0.09	1.47	0.82	11.76
IMAX Bottom HS Average	***	**0.11**	**0.72**	**4.59**	**0.76**	**0.35**	**2.03**	**0.62**	**13.93**
Sombrero HS1	Brucite	0.04	0.61	1.87	7.96	0.19	0.21	0.09	6.02
Sombrero HS Average	***	**0.04**	**0.61**	**1.87**	**7.96**	**0.19**	**0.21**	**0.09**	**6.02**
Marker 8 HS1	Brucite	2.91	0.34	2.37	4.91	0.34	0.26	0.57	10.79
Marker 8 HS2	Brucite	2.29	0.03	2.42	2.65	0.02	0.05	0.20	5.77
Marker 8 HS Average	***	**2.60**	**0.18**	**2.40**	**3.78**	**0.18**	**0.15**	**0.38**	**8.28**

Figures

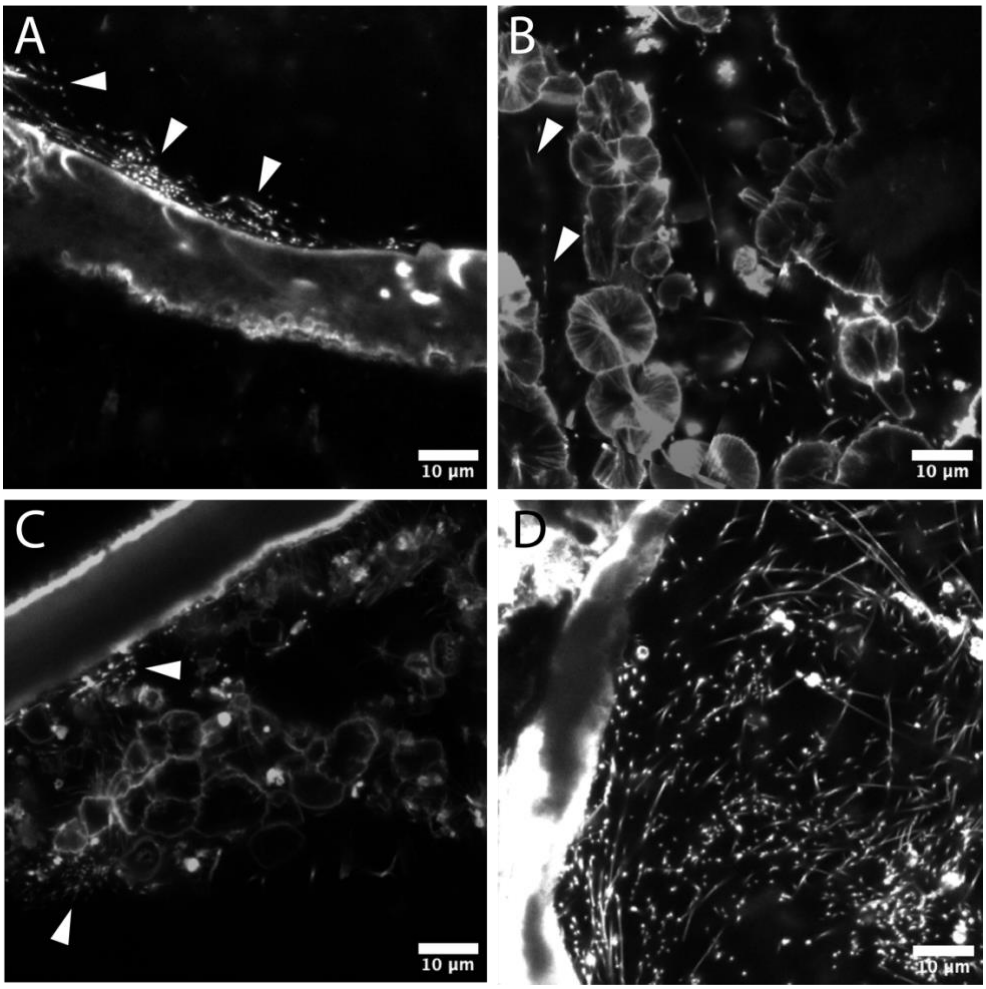

Figure 10 - Microbial community organization observed within flow channels of LCHF chimneys as imaged by confocal microscopy with the DNA-specific stain DAPI. (A) Microbial cells, denoted by arrows, forming a biofilm on a brucite-lined vent channel from LC03277 / IMAX Top. (B) The appearance of network microbial cells forming between brucite granules that appear to have mineralized on suspended EPS filaments in LC03279 / IMAX Bottom. (C) Cells denoted by arrows detected between brucite granules that have formed against a brucite lined channel causing a rough appearance to the lining from LC03280 / IMAX Internal. (D) An example of a dense network of microbial cells spanning a significant portion of a vent channel flow space from LC03279 / IMAX Internal.

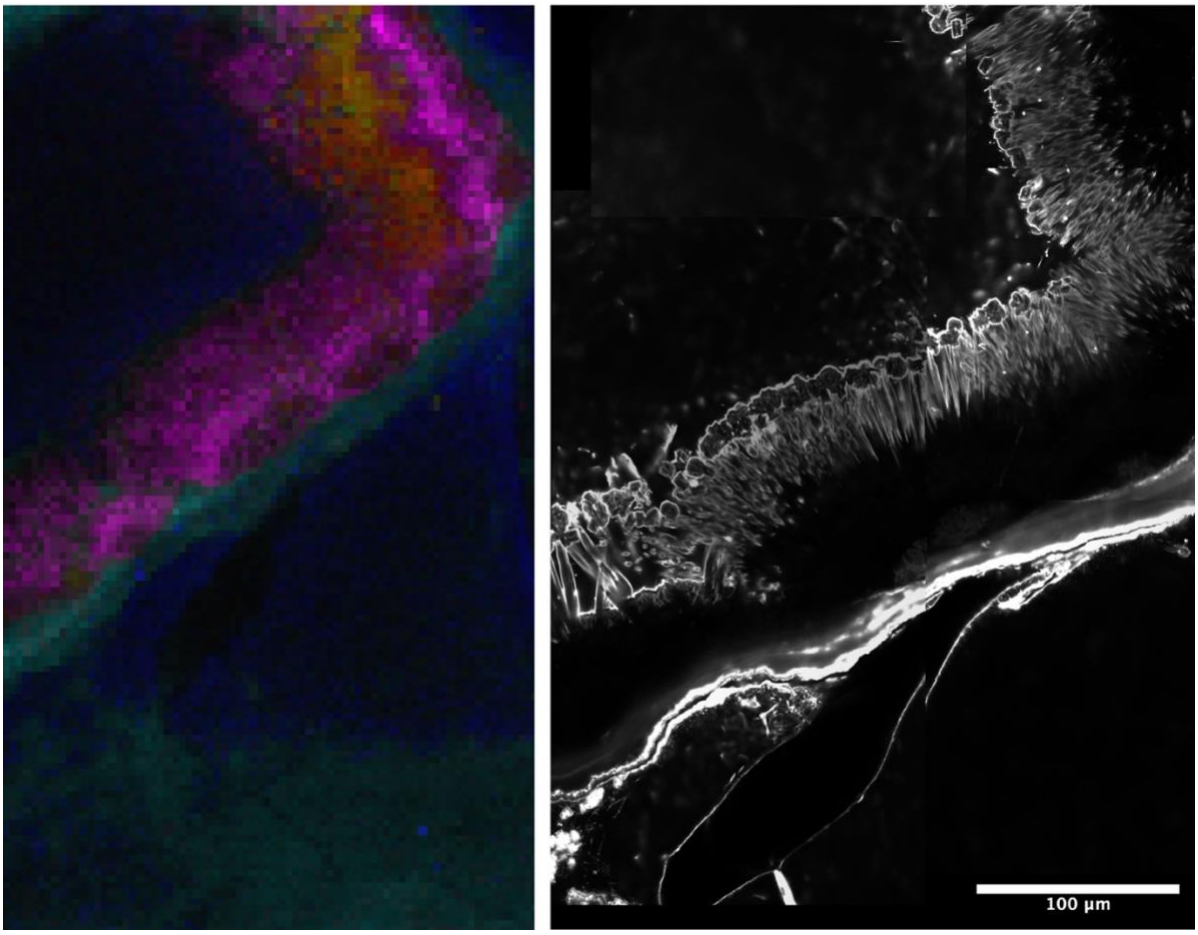

Figure 11 - Comparison between detected aragonite fluorescence in the Raman spectra of pink colored aragonite, bounded by cyan colored brucite on both sides (left) and the same region observed visually using CLSM showing the clear morphological differences between brucite and aragonite (right).

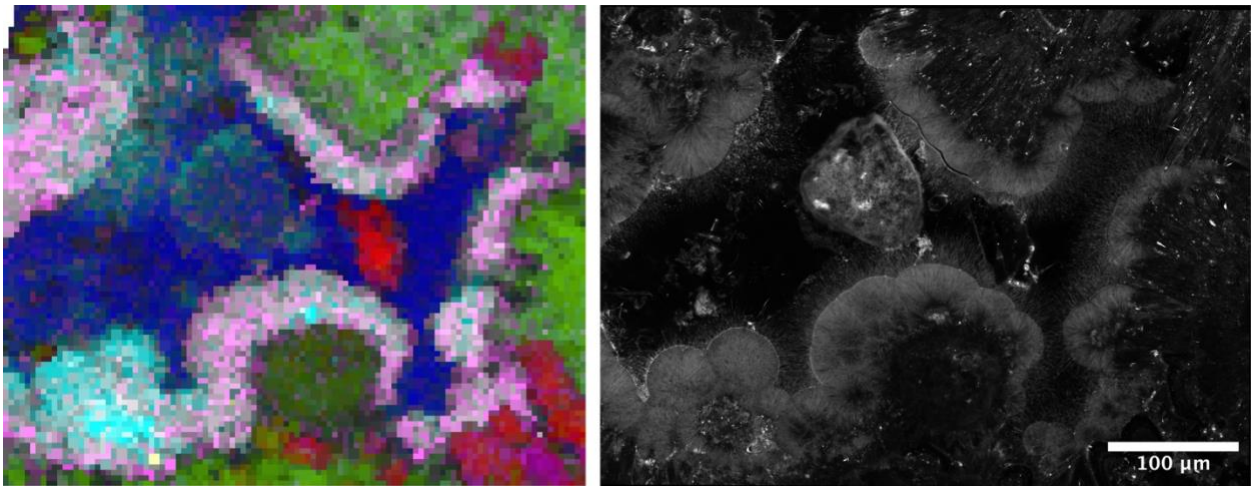

Figure 12 - Comparison of the Raman map identifying a large fluorescent light pink brucite signal (left) and the same region exhibiting both fluorescence and putative fibrous microbial growth within the same region (right).

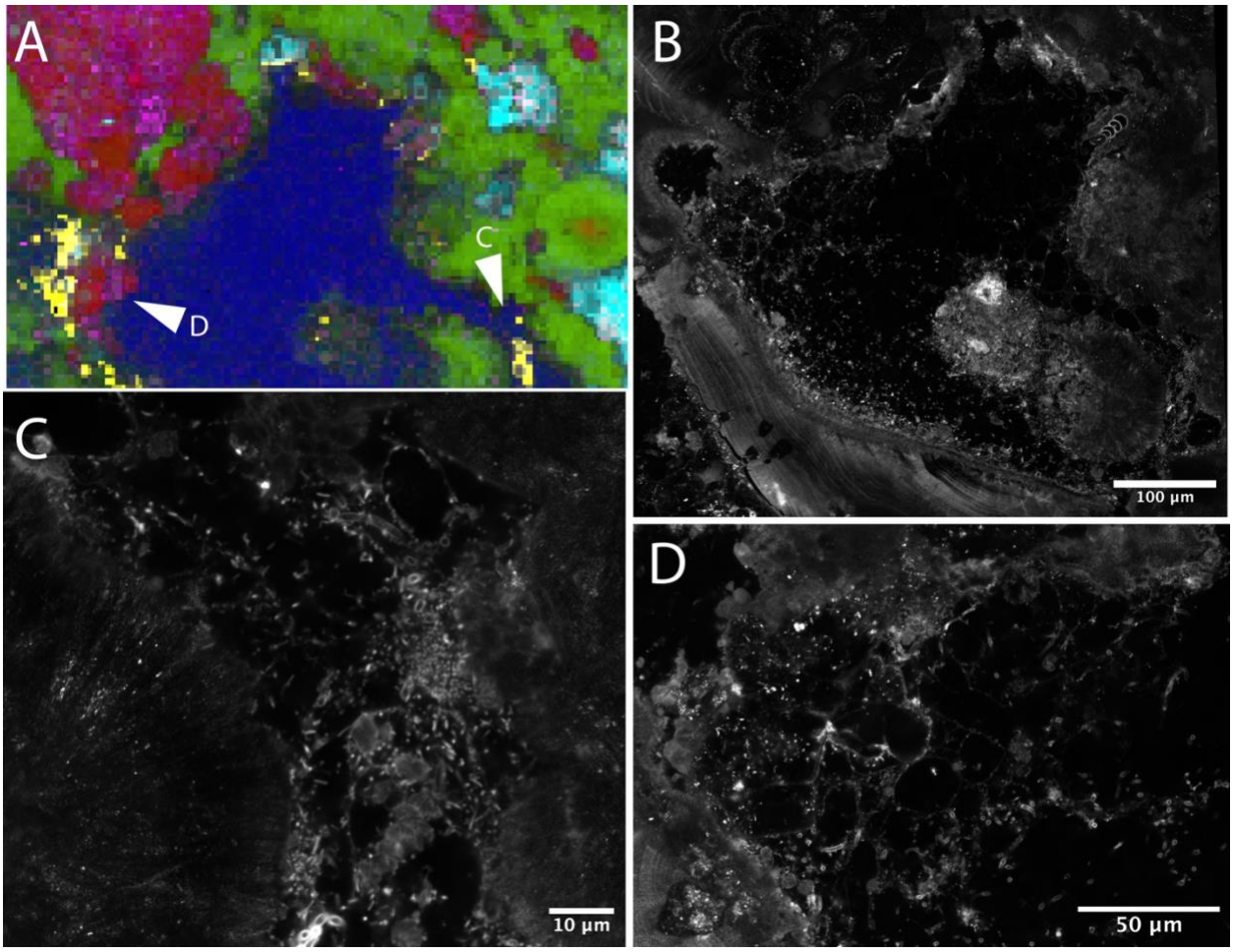

Figure 13 - Carotenoid Raman signal detections corresponding with a web of microbial growth in Marker 3. (A) The Raman map of the channel space showing areas of carotenoid detections in yellow. (B) CLSM image of the channel pore space showing a "hive" web structure extending through and covering the channel area. (C) A close up CLSM image corresponding to carotenoid signal marked by arrow C in panel A showing a large density of cells forming part of the observed hive web structure. (D) A closeup CLSM image corresponding to the carotenoid rich region marked by arrow D in panel A showing the hive web structure, but also overlapping with a calcite mineral signal as compared with the map in panel A.

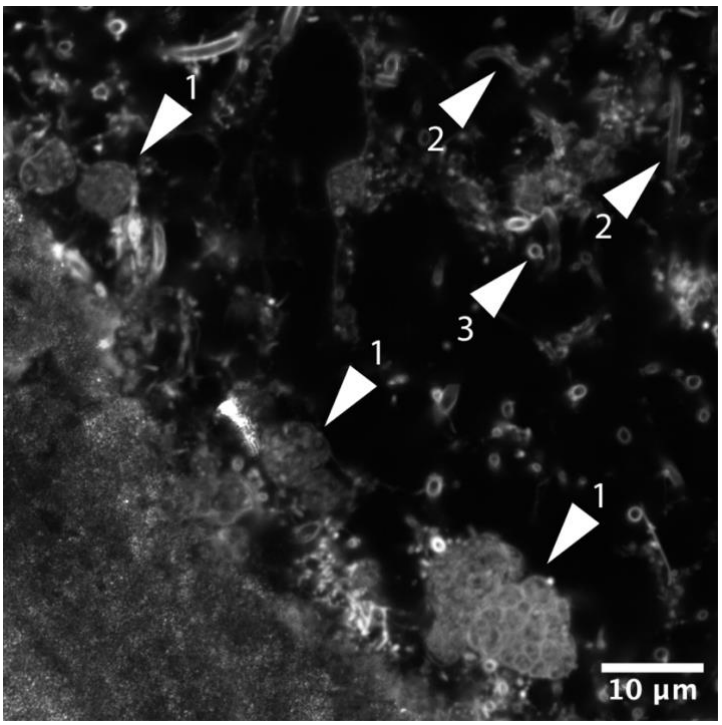

Figure 14 - Closer examination of Marker 3 microbial structures, showing putative LCMS cells with a sarcinal morphology (1) primarily on the vent wall near several filamentous (2) or sheathed cells (3) extending through the vent space.

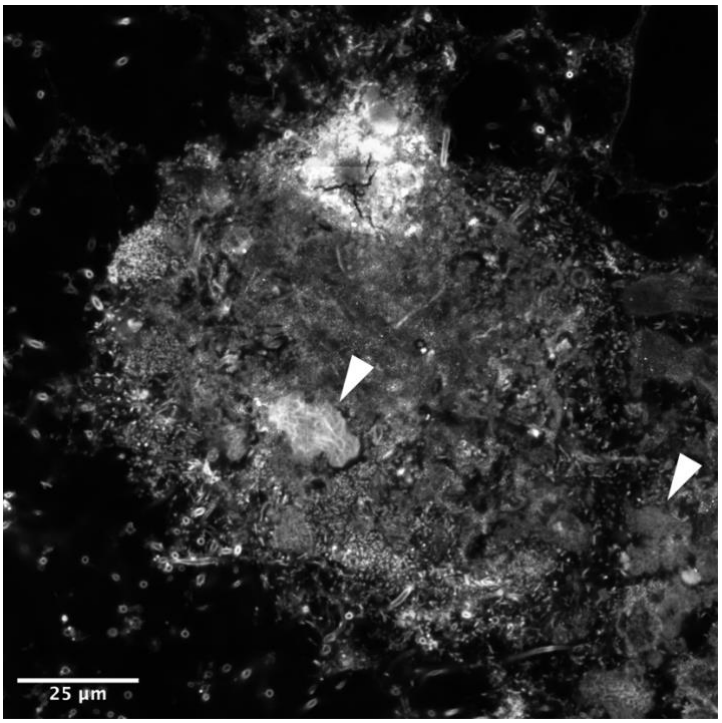

Figure 15 - Within Marker 3, a closeup of a dense microbial aggregate of diverse cell morphology that also contains an aragonite Raman signature. Enmeshed within this aggregation are putative LCMS clusters (arrows).

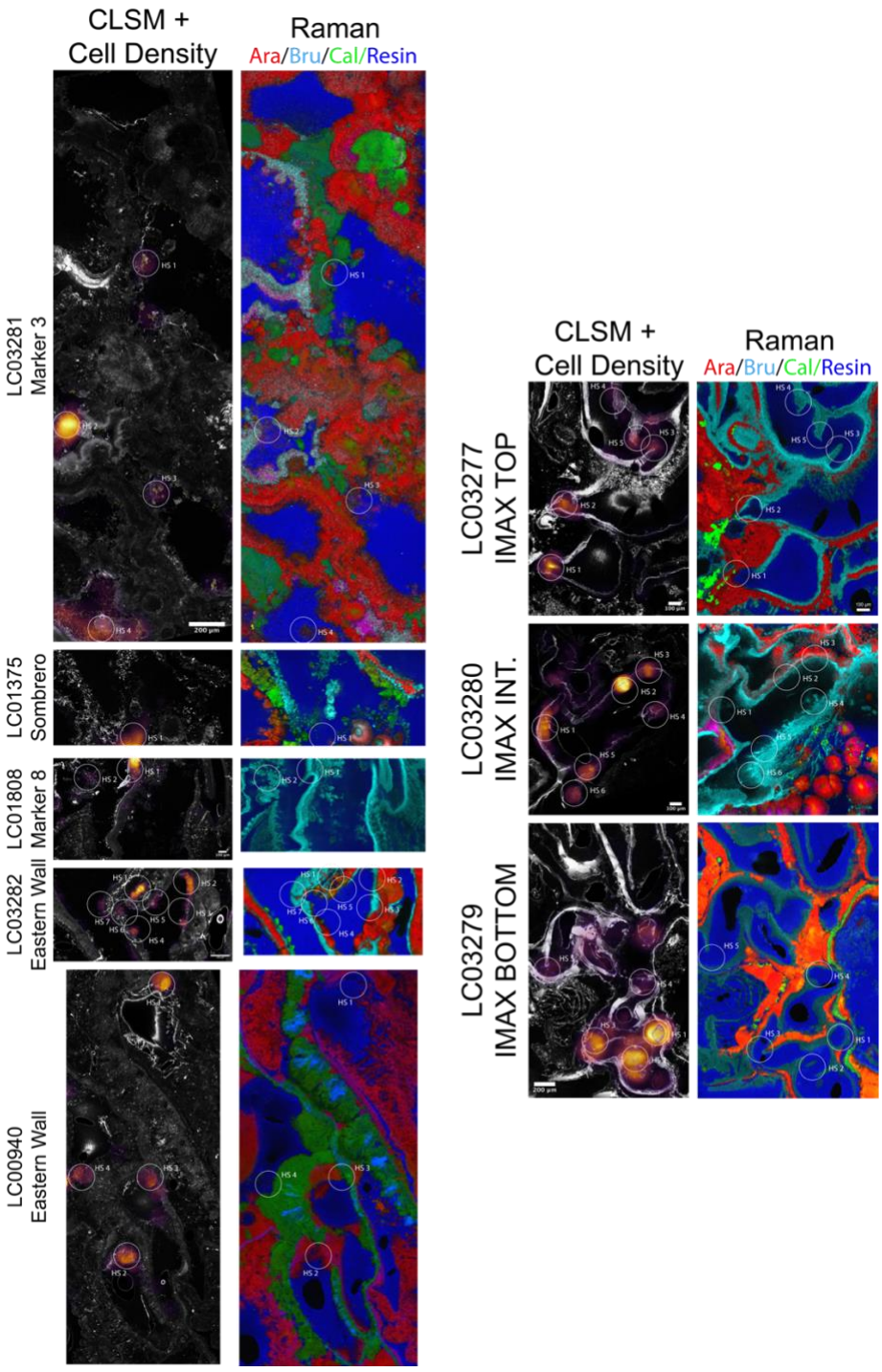

Figure 16 - Confocal Laser Scanning Microscopy (CLSM) was used to identify and annotated microbial cells in order to generate and mark where microbial density shows localized increases. Each sample contained unique hotspots heterogeneously distributed within it. Concurrently, a Raman spectroscopic map was generated to identify the mineral heterogeneity that indicates microenvironmental features where hotspots were located. Hotspot regions are circled and numbered for co-registration between analyses.

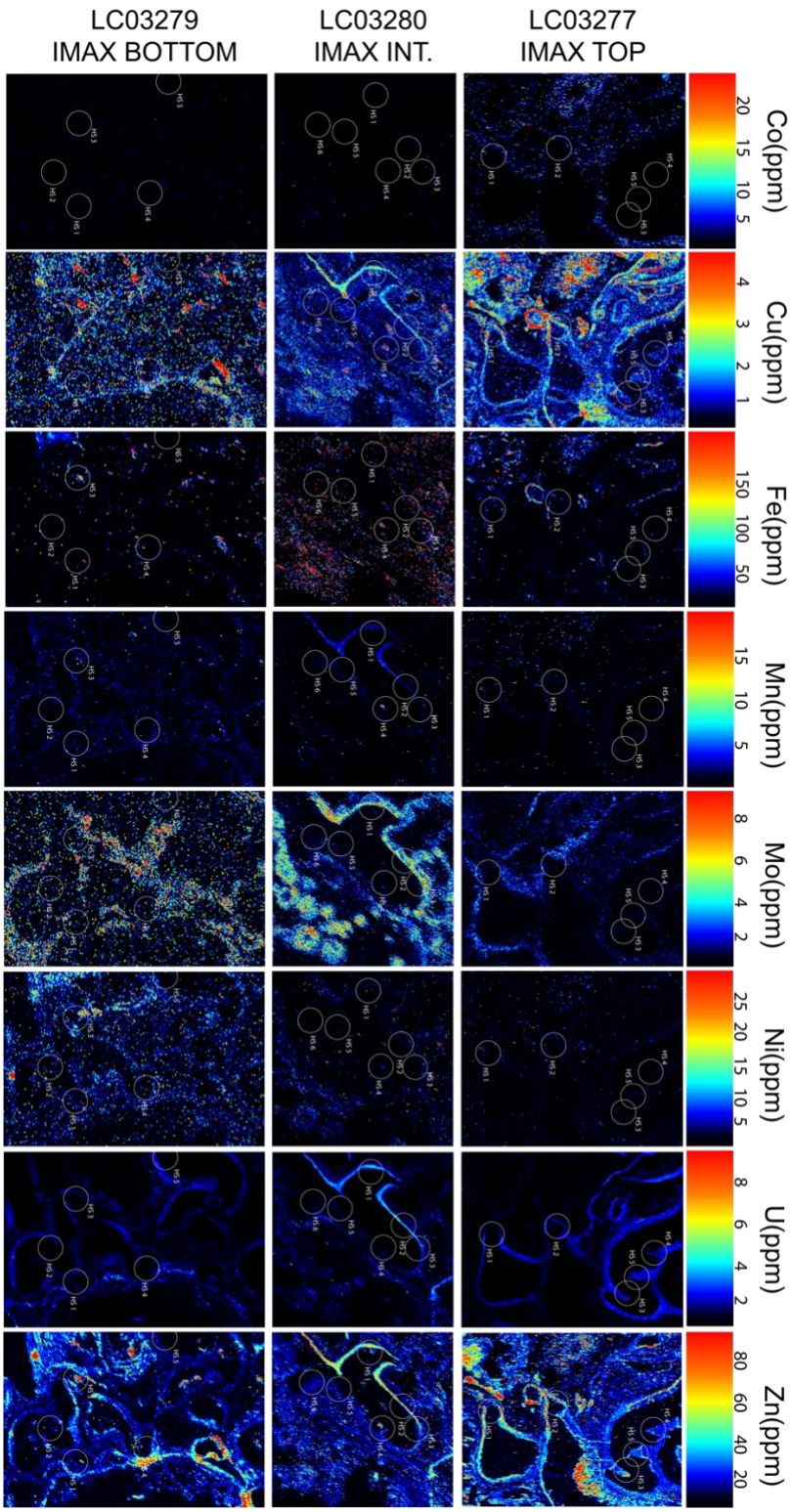

Figure 17 - Three samples were analyzed to generate a transect within the IMAX chimney from bottom to top of the vent. Comparing the entire selected element repertoire, localizations are identified both in minerals and at different points in the transect, indicating much more localized dynamics of metal enrichment than previously measured.

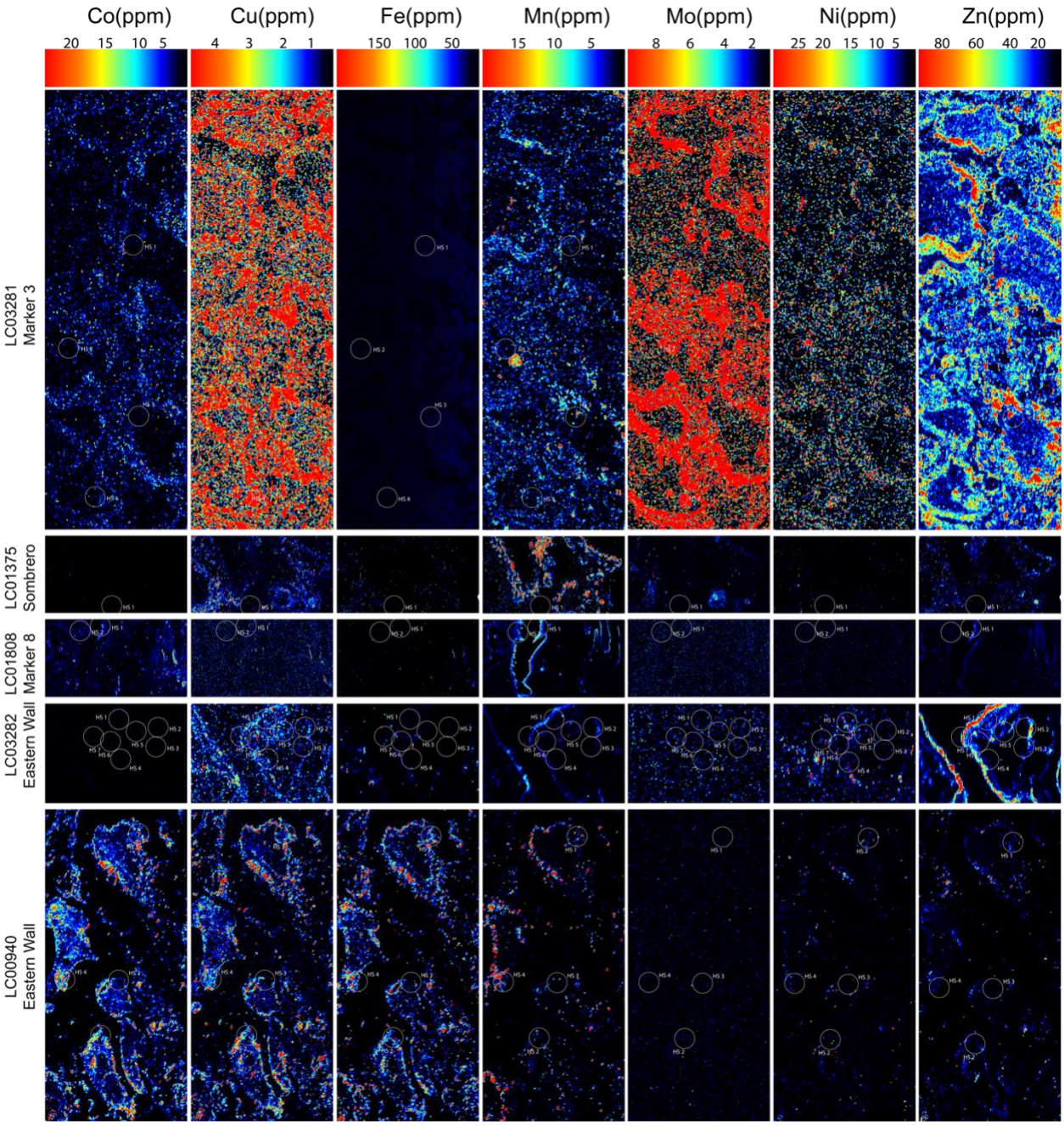

Figure 18 - Elemental analysis of selected samples from Marker 3, Sombrero, Marker 8 and Eastern Wall. Vents with similar venting histories show drastically different elemental distributions, the combinations of which may be a mixture of biotic and abiotic factors.

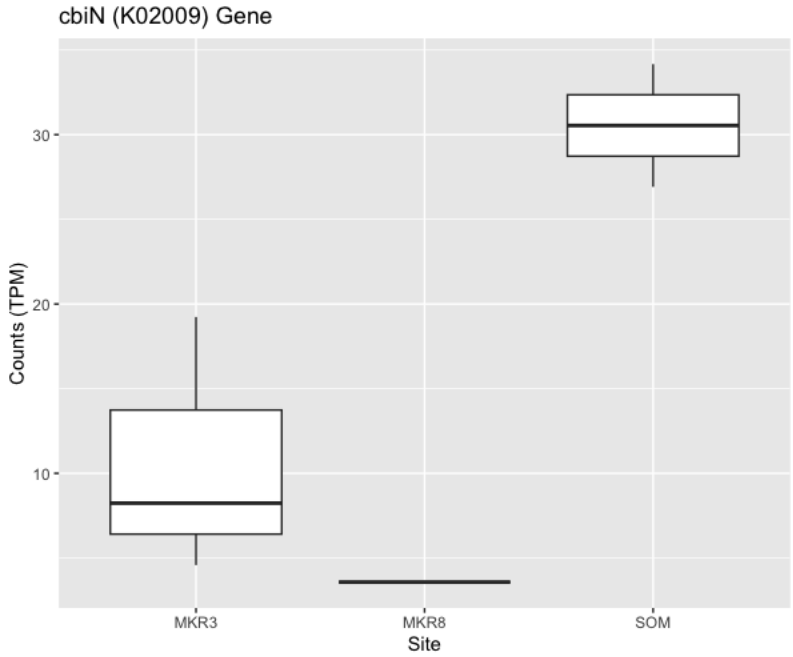

Figure 19 - Comparison of cobalt transport gene substrate binding region counts between Marker 3, Marker 8 and Sombrero sites showing increased detection in Sombrero than Marker 3.

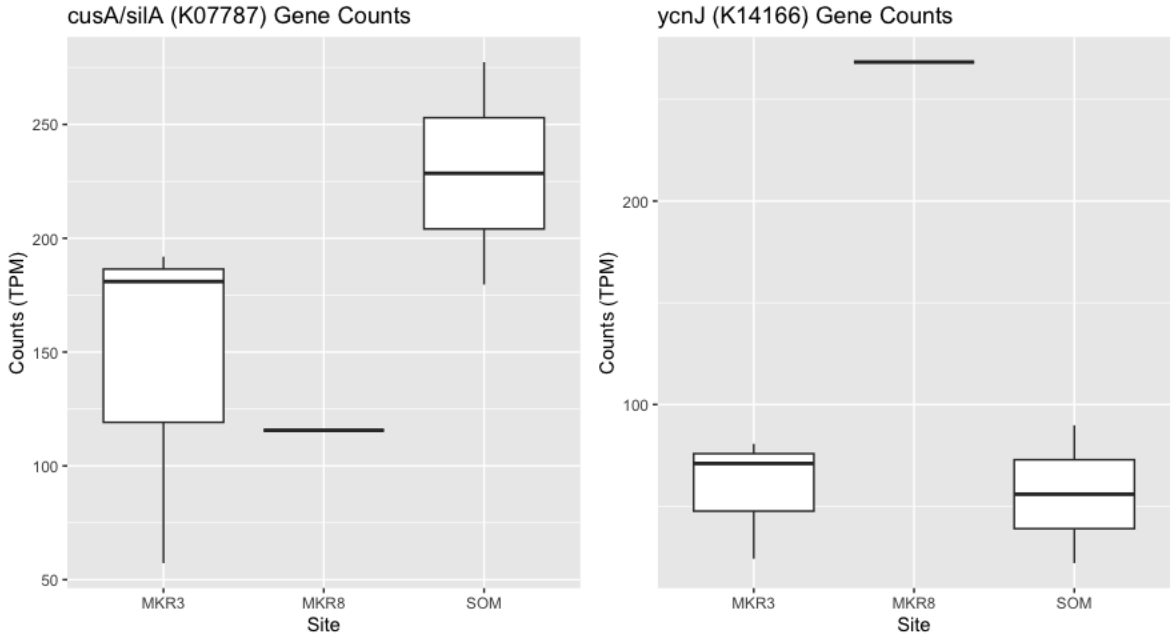

Figure 20 - Comparison of copper transport gene counts between Marker 3, Marker 8 and Sombrero sites showing differences in detections between Marker 3 and Sombrero, but also a possibility of gene preference at the site.

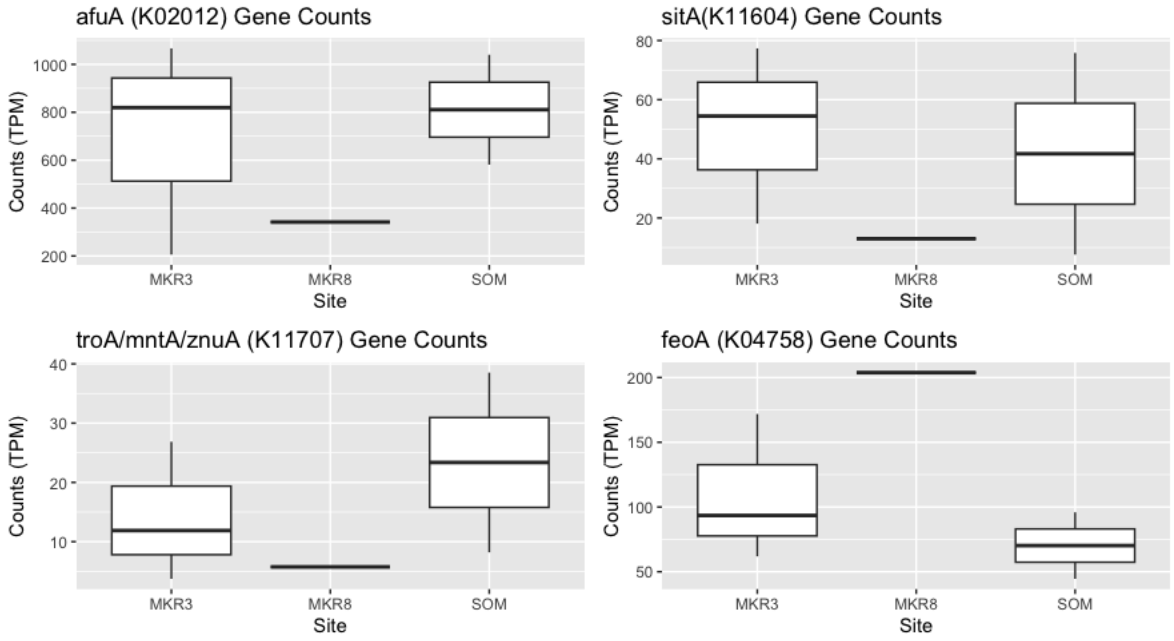

Figure 21 - Comparison of iron transport gene component counts across Marker 3, Marker 8 and Sombrero, which are also the highest detected gene counts and diversity of related genes highlighting the importance of iron in the microbial community.

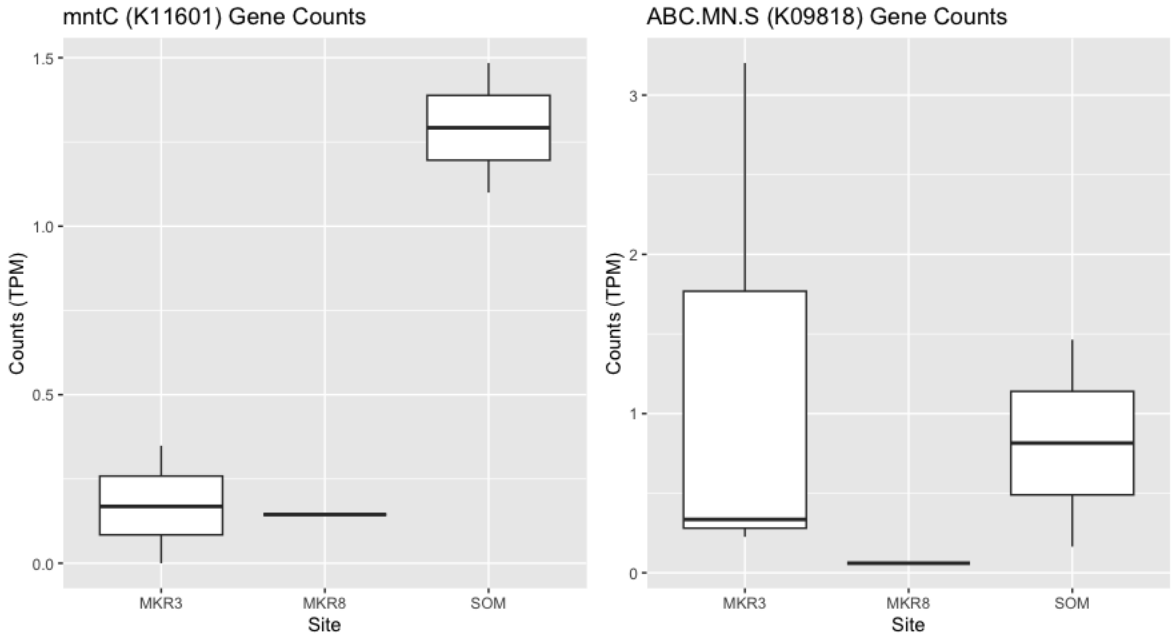

Figure 22 - Comparison of manganese transport gene count across Marker 3, Marker 8 and Sombrero showing slight differences in detection, but also a variability between gene appearance.

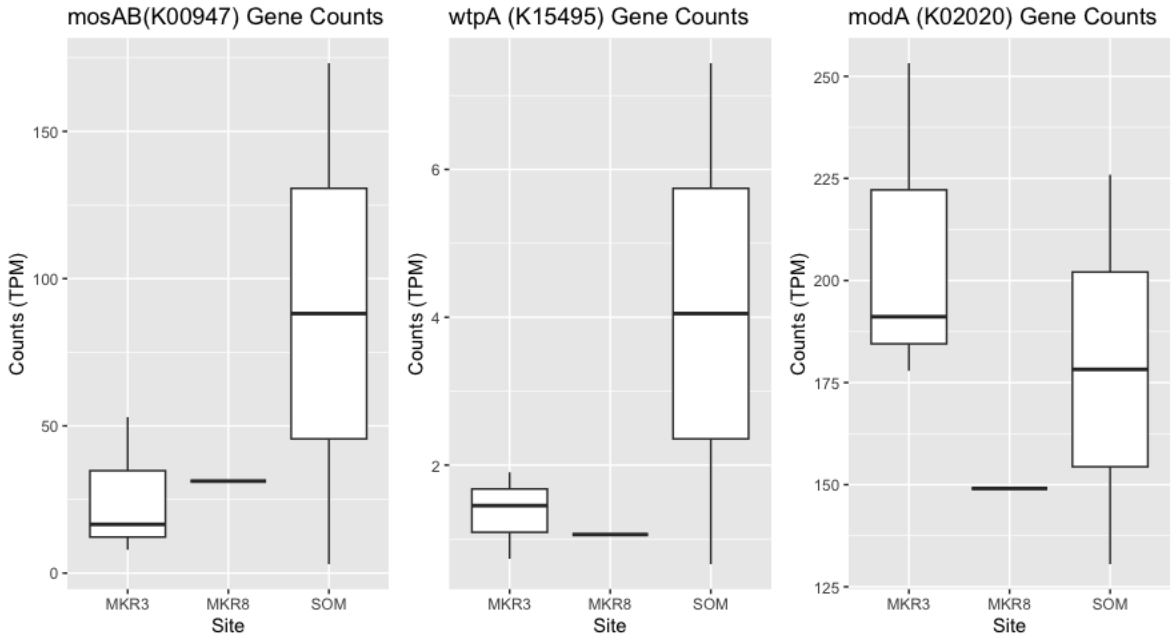

Figure 23 - Comparison of molybdenum transport genes across Marker 3, Marker 8 and Sombrero, showing similar dynamics to iron transport components and highlighting molybdenum as another element of consequence and importance to the microbial community.

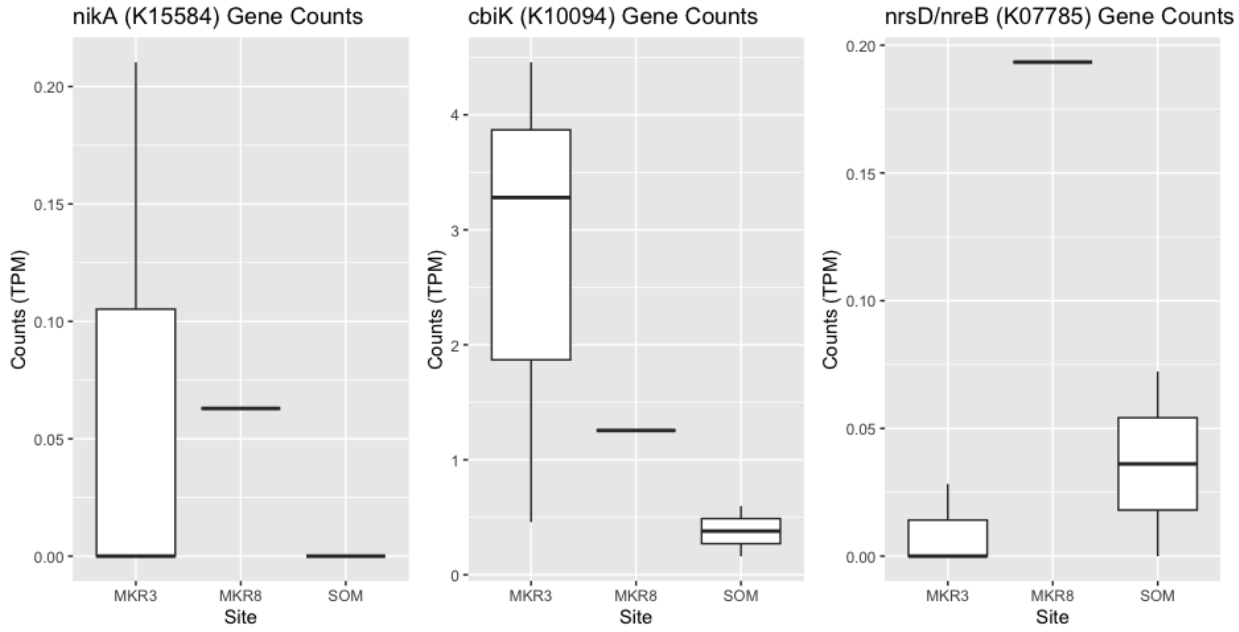

Figure 24 - Comparison of nickel transport genes across Marker 3, Marker 8 and Sombrero, showing low relative detections, but slightly higher presence in Marker 3 samples.

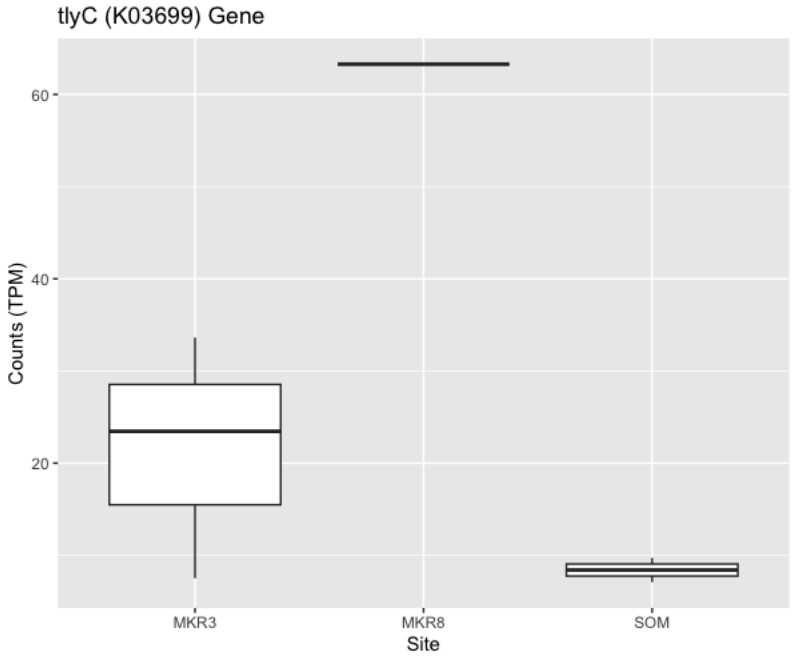

Figure 25 - Comparison of zinc/cobalt transport gene tlyC across Marker 3, Marker 8 and Sombrero, with higher detections in Marker 3 and Marker 8 illustrating a possible preference for mixed-use genes as a redundancy to single element-specific ones.

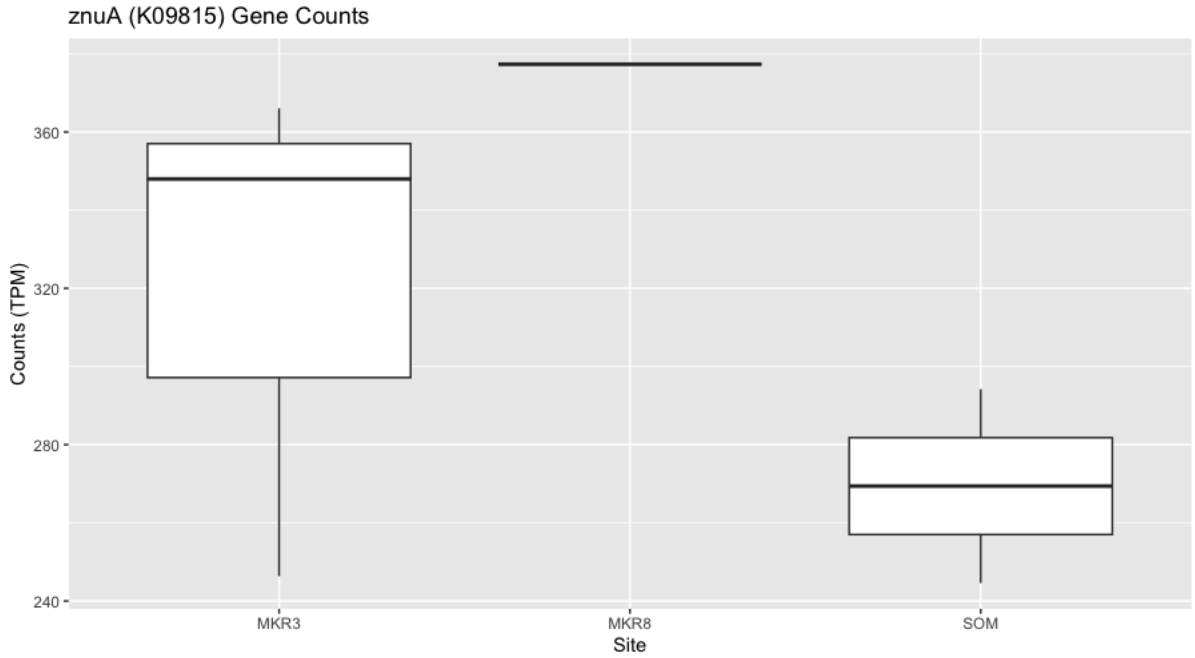

Figure 26 - Comparison of zinc transport genes across Marker 3, Marker 8 and Sombrero, showing relatively high detection in Marker 3 than in Sombrero and overall comparable to iron uptake, placing them in the same level of microbial necessity within the site.

CHAPTER 4 - METAL STRESS AND MICROBIOMES IN SERPENTINIZING LANDSCAPES

Abstract

Serpentinized ultramafic rocks are globally common features, particularly along continental margins. They weather into harsh, nutrient-poor soils that support unique endemic plants and extremophilic microorganisms. In addition to pH and nutrient stress, high concentrations of heavy metals, including Ni, Cr, and Co may be released from ultramafic rocks and accumulate in serpentine soils. Although plant-microbe interactions in these types of soils have been previously investigated, few studies have addressed microbial communities in barren (plant-free) serpentine soils and in subsurface aquifers. This study uses a unique suite of data derived from serpentine soils, rock cores, and hyperalkaline groundwater at the Coast Range Ophiolite Microbial Observatory (CROMO) in northern California to study the relationship between trace metal distributions and microbial communities. Ni, Cr, and Co were found to be enriched in bedrock, but heterogeneously distributed and most abundant in serpentine bearing mineral assemblages. Likewise, dissolved Ni and Cr were abundant in groundwater, but displayed no clear relationship to fluid pH, depth, or other physical-chemical parameters. Comparisons between taxonomic abundances in 16S rRNA amplicon sequence data and trace metal concentrations in fluid and core samples were used to investigate key taxa correlated with Ni and Cr abundances, but found no clear statistically supported relationships, likely due to the near uniformly high concentrations of these metals at the site. Examination of shotgun metagenomic and metatranscriptomic data from high pH groundwater at the site showed the occurrence and expression of genes involved in metal efflux systems in the presence of >100 ppb Cr and >500 ppb Ni. These genes were abundant in microbial populations that are prevalent in

the hyperalkaline groundwater at CROMO and other serpentinites and likely help these organisms contend with metal toxicity. Metal stress constitutes an additional expense of resources and energy in serpentinite-hosted environments, that may serve to limit microbial productivity in these extreme ecosystems. Physiological adaptations to high metal concentrations may play an important role in selecting for the uniquely adapted microorganisms found in serpentinizing environments and guide future efforts towards biomining and environmental sustainability.

Introduction

Habitat diversity in serpentine landscapes

Serpentinizing ophiolites are globally common features as oceanic crust is emplaced onto continental margins through the process of plate tectonics (*279*). As these ophiolites become incorporated into terrestrial ecosystems, they strongly influence local soil compositions as ultramafic rocks are chemically altered and eventually erode into serpentine soils. Serpentine soils are very different than common organic-rich soils used in agriculture as they have an elevated pH, poor water retention, and major differences in the distribution of nitrogen, phosphorus and potassium (*280*). As they are sourced from silica-poor ultramafic source rocks, they are generally enriched in the heavy metals Ni, Cr, and Co (*281*, *282*). This challenging soil environment results in unique endemic plant species capable of overcoming metal toxicity and nutrient limitation constraints (*283*). Rhizosphere-associated microorganisms in these serpentine ecosystems have been shown to promote nitrogen fixation coupled to nickel-resistance that enable their plant partners to proliferate in harsh soils (*284–286*). In regions with abundant serpentine soils, fauna characterized as hyperaccumulators are found with leaf nickel concentrations in excess of 1% engaging in cooperative metal uptake with microbial root

partners (*287*). Serpentinizing ophiolites have been subject to more recent focus due to their characteristic hyperalkaline groundwater and associated seeps as fluids reach the surface (*21*). These environments host unique, low diversity extremophilic microbial communities adapted to extremely high pH (>11), and low oxygen conditions (*90*, *288–290*). The microbial community composition observed in the serpentine soils and surface rock features is closely linked to nutrient availability, particularly nitrogen and carbon, exhibiting clear spatial variability across landscapes and related to seasonal and hydrologic variations (*291*). Beyond soils, serpentinite ecosystems can have more nuanced effects on biological activity that have been less well understood such as latitudinal temperature differences and hydrological changes that influence plant productivity and the interlinked soil chemistry. This highlights the variability of physical and chemical features seen at both the land surface and in the subsurface yet to be understood and becomes critical to study as climate shifts become more pronounced (*292*). Serpentine habitats can be further impacted by processes unique to their locations, such as strong seasonal wet-dry cycles, surface vegetation, briny subsurface aquifers, hydrothermal activity, and many other factors. While the composition of serpentinizing ophiolites is broadly similar, they all have high H_2 concentrations and high pH, the variety of geochemical regimes outlined above coupled with sparse information on the resident microbial populations make it difficult to decouple the biotic and abiotic processes that contribute to key biogeochemical cycles. This is apparent when comparing sites such as Tablelands, The Cedars, Hakuba-Happo, Santa Elena and CROMO - all serpentinite hosted terrestrial sites sharing the characteristics of ultrabasic fluids, methane production from a variety of sources unrelated to serpentinization, or in the case of Aqua de Ney, observing a complete absence H_2, a canonical product of serpentinization (*21*, *78*, *293*, *294*). Ultimately, the variety of conditions serpentinite hosted sites exist within shape the character of

their geochemistry and will inherently control the activities of microbial communities and macrofauna in serpentine habitats both at and below the surface.

Serpentine-associated rocks and soils are generally harsh and nutrient depleted

The collection of plant environmental stressors in serpentinites, termed "serpentine syndrome" are driven fundamentally by a combination of low productivity resulting from deficiencies in micro- and macronutrients, as well as high toxicity from accumulation of heavy metals such as Ni, Cr, Co and Mn (*295*). This is further exacerbated by poorly developed rocky soils primarily derived from the weathering of serpentinite rocks. The earliest examinations of microbiology in serpentinite soils noted nitrogen limitation as far back as the 1920's with an understanding of microbes bearing a critical role in maintaining soil health and fertility for plant productivity and agricultural potential (*296, 297*). Symbiotic nitrogen-fixing bacteria associated with serpentine endemic plants have been shown to enable their success in nutrient poor soils, with the distinct possibility that these partnerships driven by plant selection may account for a majority of the factors influencing biological remediation of soil chemistry (*298*, *299*).

As water and iron-rich minerals in the ophiolites react, extremely high pH fluids, commonly greater than 11, are produced while oxygen is concomitantly consumed resulting in a highly reducing environment (< -550 mV) (*21, 288*). These hyperalkaline waters strongly limit the availability of extracellular protons necessary to support common cellular electron transport processes. In systems such as soda lakes, alkaliphilic microorganisms have been shown to use alternative ions such as K^+ and Na^+ to facilitate membrane transport and flagellar activity (*22, 300*). High pH may further impact molecular stability of key molecules such as RNA, requiring increased mRNA expression to overcome increased degradation, among other specific adaptations and repair mechanisms that maintain homeostasis and cell function (*22, 301*). A

subtle but important consequence of these challenges is that due to high pH and high concentrations of divalent cations such as Ca^{2+} and Mg^{2+} in the serpentinizing fluids, dissolved inorganic carbon (DIC) is scrubbed from the surrounding medium, precipitating as various carbonate minerals. Additionally, although serpentinization has the potential to liberate copious energy in the form of H_2, abiogenic methane, and other small organic compounds, serpentinization-associated environments are generally poor in organic matter that would support traditional heterotrophic oxidative respiration. Further, the water-rock reactions consume oxidants leading to highly reducing fluids and lead to a scarcity of alternative terminal electron acceptors. Fundamentally, these processes lead to less available free energy to enable growth and facilitate stress responses. An extensive study of an array of extreme environments shows a delicate balance between available energy flux and the growth and survival of microorganisms at environmental extremes, resulting in a gradient of survival strategies ranging from alternative metabolic processes as adaptations to energy limitation to dormancy and anhydrobiosis (*2*, *3*). In serpentine grasslands, nutrient limitation and retention is strongly coupled to processes such as precipitation, organic matter respiration, and photosynthesis (*302*, *303*). Microbial community composition in serpentine soils demonstrates clear changes because precipitation patterns and nutrient addition/depletion setting the stage for other biogeochemical and physiological responses (*291*, *303*). A recent comparison of metagenomic data highlights the global importance of phosphorous scavenging mechanisms in serpentine seeps, where meteoric water inputs influence both the chemistry and the microbial community composition drastically (*89*). Fundamentally, the mobility and availability of phosphorous, among other nutrients in these settings, is tightly coupled to environmental conditions, meteoric inputs and leaching from other rocks and minerals or rapid uptake by biology and mineralization processes (*304*).

Serpentinites and serpentine soils are highly enriched in trace metals

While overall large-scale geological and environmental conditions create an array of stressors within serpentine ecosystems, less obvious are the constraints imposed by heavy metals on microbial communities. As serpentinites originate in Earth's upper mantle, they have high abundances of nickel, chromium, and cobalt bearing minerals such as olivine, pyroxenes, and spinels. Globally, these systems serve as rich resources of these metals for the mining industry and are becoming much more vital components of emerging energy storage and transmission technologies, rendering their acquisition increasingly valuable (*305*, *306*). While most metals are generally insoluble at high pH, in serpentinization influenced systems, dissolved Ni, Cr, and Co complexes can allow these metals to remain mobile at relatively high concentrations and relatively more accessible than the lower concentrations found in crustal locales (*307*).

Weathered ultramafic rocks, known as laterites, are some of the world's most important sources of nickel, as well as other Platinum Group Elements (*308*). Recent estimates suggest that these deposits host up to 60% of the global nickel supply, where it can be enriched to nearly 3% of total solid mass (*309*). Depending on the geologic setting and its history, certain serpentinites that host ultramafic igneous intrusions known as chromites may also be highly enriched in chromium and are readily mined as a primary source, with far reaching environmental and health impacts to its host ecosystems (*310*). Peridotites and their weathered products may similarly be enriched in cobalt and other heavy metals owing to their origins in silica poor, reducing regions of Earth's upper mantle and their weathering processes remobilize their elemental constituents, making them a compelling exploration targets for the mining industry (*311*). However, as is the case with any localized increases of heavy metal concentrations there is a sustained and measurable ecosystem stress most notable in plants through detrimental interaction with

enzymes, perturbed cellular and molecular stability, or overproduction of reactive oxygen species (*312*, *313*).

The form and oxidation state of nickel, chromium, and cobalt greatly influences their concentration in natural waters, as well as their environmental toxicity (**table 8**). For example, nickel hydroxide complexes stay soluble at pH close to 10, reaching values over 50 ppb in certain geological settings (**table 10**). Oxidized chromium becomes more soluble at alkaline pH compared to neutral pH, and hexavalent chromium has been considered as a clear threat to environmental health via drinking water in serpentine terranes of California (*314*). Cobalt hydroxides are similarly amphoteric, with a higher solubility at alkaline pH similar to the range found in serpentinite-hosted groundwater (pH >11) (*315*). Such conditions may allow for the dissolution and transport of these heavy metals and their deposition at elevated concentrations sufficient to induce cytotoxicity.

Microbial communities are locally adapted to stressors imposed by serpentinization

Serpentine soils harbor distinctive endemic plant species, specifically adapted to harsh environmental conditions including low nutrient concentrations and high pH as described earlier. One strategy identified in serpentine endemic plants is to form symbiotic relationships with rhizosphere-associated bacteria. The plants provide a carbon source to the rhizosphere communities in exchange for N_2 fixation and nickel detoxification functions (*316*). Another strategy employed by serpentine endemics is to hyperaccumulate these metals as metabolites, as seen in the blue-green latex (up to 25% nickel by weight) of the *Pycnandra* plant native to New Caledonia (*317*). In subterranean environments, microorganisms survive by using alternative ions to facilitate cross-membrane transport (*86*). Serpentinite-adapted microbial communities have also been shown to use available reduced carbon sources such as formate and CH_4 as

alternatives to DIC utilization. However, to our knowledge, serpentinite-associated microbial communities have not yet been broadly investigated for metal resistance mechanisms and how *in situ* metal distributions relate to other stressors shaping microbial diversity and adaptation. Microbes possess diverse regulatory and housekeeping functions aimed at maintaining metal homeostasis within the cell and preventing toxic accumulation by either creating passive removal processes relying on molecular interactions with cell wall components, or utilizing active processes such as targeted transport or efflux systems (*318*).

This paper explores the relationship between heavy metal content and free-living microbial populations in a serpentinizing ophiolite of the California Coast Range across three different habitats, soils, altered bedrock, and ultrabasic groundwater. Adaptations of microbial populations to metal stress were examined through amplicon sequencing, metagenomic, and metatranscriptomic data from the same locations. Together these data were used to illuminate patterns of microbe-metal interactions and the potential mechanisms of metal resistance in this harsh yet globally common ecosystem.

Methods

This study was carried out at the McLaughlin Natural Reserve, a University of California field station in the California Coast Range. Within the McLaughlin Reserve, the Coast Range Ophiolite Microbial Observatory (CROMO) is a series of monitoring wells with associated core samples that was established in 2011 (*319*). Core samples were collected using aseptic technique during drilling operations in 2011, flash-frozen in liquid nitrogen and stored at –80°C or preserved in 4% paraformaldehyde-1× PBS buffer, followed by storage in 70% Ethanol at -20°C. as required for molecular and microscopic analyses, respectively. Details related to sampling well water at CROMO are described in Twing, et al., 2017 and employed a low-flow

submersible pump to deliver reducing groundwater to the well head without degassing (*290*). Microbial populations in water samples were collected on 0.22 µm Sterivex filters (Millipore; Billerica, MA) and flash-frozen in liquid nitrogen before long term storage at –80° C.

Geochemical data from CROMO

Standard water quality measurements (pH, ORP, temperature, etc.) of CROMO groundwater were carried out by attaching the pump tubing from the well head to a flow cell with a submerged YSI multiprobe, similar to what has been previously described (*290*, *320*) . A compendium of mineralogical and elemental chemistry data was generated from analyses of soil and rock samples from the CROMO, some of which is previously reported as lithostratigraphic analyses (*319*, *321*) and some of which is included in a manuscript representing a thorough description of subsurface biogeochemistry (Twing et al 2024, in review). This study specifically focused on the heavy metal content of the cores and fluids from CROMO. Core and soil samples were ground to a <100 µm sized powder in metal-free conditions and sent to ActLabs (Ontario, Canada) for analysis by ICP-MS and Instrumental Neutron Activation Analyses (INAA). Fluid samples were collected in May/June 2016, 0.22 µm filtered, and acidified on site with 1% trace metal grade nitric acid, before being submitted for analysis by ICP-MS at the Analytical Geochemistry Laboratory at University of New Mexico.

DNA/RNA extraction from CROMO cores and groundwater

Thawed core samples and soil material were homogenized using autoclaved and ethanol-sterilized percussion mortars and ceramic mortars and pestles. DNA was extracted from two parallel samples of approximately 10 g homogenized core using the PowerMaxSoil Kit (MoBio, Carlsbad, CA, USA), following the manufacturer's instructions. The resulting DNA suspensions were pooled from replicate extractions and concentrated in an Amicon Ultra-2 Centrifugal Filter

Unit with Ultracel-30 membrane (Millipore, Darmstadt, Germany) to a volume of 50 µL. DNA was quantified using High Sensitivity regents for a Qubit® 2.0 Fluorometer (Life Technologies, Grand Island, NY, USA), which has a detection limit of 0.1 ng/µL. Cells on filter cartridges were lysed by using freeze/thaw cycles and lysozyme/Proteinase K treatment and purified using a series of phenol/chloroform extractions. DNA was precipitated using ethanol and purified using the Genomic DNA Clean & Concentrate kit (Zymo Research, Irvine, CA, USA). Genomic DNA was quantified using the High Sensitivity dsDNA Assay Kit on a Qubit fluorometer (Invitrogen, Carlsbad, CA, USA). RNA extractions were performed as previously described, using a modified phenol/chloroform extraction method. RNA was precipitated using ethanol, suspended in RNAse-free water, and quantified using a Qubit fluorometer (Invitrogen, Carlsbad, CA, USA) (*172*).

DNA and cDNA sequencing

Purified DNA samples from core and soils were submitted to the Josephine Bay Paul Center at the Marine Biological Laboratory (MBL) for sequencing of the V4-V5 region of the 16S rRNA gene on an Illumina MiSeq instrument as part of the Census of Deep Life project. Sequence data from rock cores and soils are available via NCBI SRA BioProject PRJNA1097798. The paired-end reads were merged and subjected to MBL's post-processing quality control for removal of low-quality reads and chimera checking (*322*). The samples yielded 8,493 to 246,345 and 12,020 to 241,730 merged, quality-filtered sequences with the bacterial and archaeal primers, respectively. Extracts from fluid samples were sequenced at the MSU Genomics Core facility targeting the V4 region of the 16S rRNA gene. Amplification, quantification, and sequencing procedures performed by the MSU Genomics Core have been previously described (*172*). Field and extraction blanks collected alongside samples in this data

set could not be quantified or amplified and were not submitted for sequencing. Fluid-derived sequences are available in the NCBI SRA (PRJNA289273). Sequences generated by MBL and the MSU Genomics Core were processed using mothur v1.39.5 and annotated as previously described (*172*, *290*, *323*).

Metagenomic and metatranscriptomic processing

Metagenome and metatranscriptome sequencing were conducted at the Joint Genome Institute (JGI) on an Illumina HiSeq2000 instrument as previously described (*24, 290*). Briefly, all CROMO metagenomes and metatranscriptomes were pooled together for a master CROMO assembly computed with Ray Meta v.2.3.1 (*324*). Phylogenetic affiliation of contigs was assigned using PhyloPythiaS (*325*). Metagenome and metatranscriptome short reads were mapped to the pooled assembly using Bowtie2 v.2.2.6 (*141*). The Prokka pipeline was used for gene prediction and functional annotation of contigs (*326*). The arguments –metagenome and –proteins were used with Prokka v.1.12 to indicate that genes should be predicted with the implementation of Prodigal v.2.6.2 optimized for metagenomes as described by Twing et al (*139*). Metagenome-assembled genome (MAG) bins were constructed with ABAWACA (https://github.com/CK7/abawaca) using tetranucleotide frequencies and differential abundance as measured by Bowtie2-mapped read abundances. Bin quality was computed with CheckM (60), and only high-quality MAG bins are reported here (>50% completeness and <10% contamination) (*144*). The completeness and contamination of some bins were improved by refinement with Binsanity (*142*). Taxonomic classifications of MAGs were assigned using GTDB-Tk (https://github.com/Ecogenomics/GTDBTk) (*143*). Predicted protein-coding sequences were annotated by searching the Kyoto Encyclopedia of Genes and Genomes release v. 83.2 within Prokka and HTSeq v.0.6.1 and were used to calculate predicted protein

abundances (*154*, *327*). The abundances of predicted protein functions in all CROMO metagenomes and metatranscriptomes were normalized to predicted protein size and metagenome size. Data reported here are in units of metagenome fragments per kilobase of predicted protein sequence per million mapped reads (FPKM). The identity of organisms harboring metal resistance genes was queried using Metagenome Assembled Genomes (MAGs), as previously reported in Sabuda, et al., 2021 (*320*). Metagenomic data from this study are available under NCBI SRA BioProject accession numbers PRJNA672823, PRJNA410019, PRJNA410020, PRJNA410022 to PRJNA410033, PRJNA410035 to PRJNA410037, PRJNA410054, PRJNA410057, PRJNA410286, PRJNA410403, PRJNA410404, PRJNA410553 to PRJNA410555, and PRJNA410557.

Dataset processing and statistical analysis

16S rRNA data for both archaea and bacteria were analyzed separately using R Studio version 4.2.2, with initial data processing carried out within the Phyloseq package and as previously described (*146*, *149*). Samples were normalized and transformed to relative abundance. 126,182 archaea and 40,417 bacterial taxa were initially identified before a prevalence filter was applied to keep sequences present in at least 1 read and greater than or equal to 1% abundance in samples, resulting in 61 archaea and 58 bacterial taxa to analyze for correlations. Correlation tests of archaeal and bacterial taxa were carried out against the measured sample metal content using the ltm package rcor.test() function, followed by a multiple tests correction using the R package qvalue and qvalue() function (*151*) (*152*, *153*). Significant correlation scores with $p < 0.05$ and $q < 0.05$ were used to identify the most significant correlates against metal measurements, if any were identified.

Results and Discussion

Lithological Variations in Heavy Metal Concentrations

The collection of rocks, soils, and fluids from the CROMO allowed for direct comparisons between different reservoirs of heavy metals at the site. The serpentinites of the Coast Range Ophiolite cover an expansive region in northern California, with additional potential metal inputs coming from runoff from the nearby Sierra Nevada Mountain Range and the extensive agricultural areas nearby. As ultramafic rocks (i.e., serpentinizing peridotite) are the most obvious source material, we compared different lithologies within the collected core samples to soils and groundwater. Overall, core samples showed high concentrations of Nickel (78 – 2260 ppm), Chromium (120 - 2760 ppm), and Cobalt (23.1 – 132 ppm) relative to ordinary crustal rocks. However significant differences were observed within different lithostratigraphic layers of the ophiolite, with serpentine-bearing layers generally more enriched in metals than other rock types (**Table A.2**). Chromium is primarily concentrated in minerals such as chlorite and magnetite, both found at the site with the former is found on average below 20 m depth. Clay minerals are also readily identified within the core strata. These minerals have high adsorption properties because of their charge and crystallographic structure. In both serpentines and other metal-enriched systems like industrial wastes, clays have been shown to preferentially adsorb significant proportions of chromium, nickel and other heavy metals compared to surrounding soils or minerals (*314*, *328*). Surface soils from CROMO contained relatively lower concentrations of Ni, Cr, and Co (**Table 9, Table A.1**). These variations speak to the importance of local mineral assemblages as sources of these heavy metals as well as loss processes for metals during the weathering of ophiolites to serpentine soils such as fluid transport and

biological uptake, amongst other factors. These results are consistent with nickel and chromium concentrations previously detected in soils from the CROMO study region (*329*).

Wells within the CROMO network draw from an exceptionally low permeability aquifer, where distinct fluid chemistries are preserved both vertically and laterally. While fluids are generally more reducing and saline in deeper wells, other parameters like hyperalkaline pH persist in near surface aquifers. Nickel concentrations in CROMO groundwater range from 67 – 629 ppb and Chromium concentrations from 16 – 139 ppb (**Table A.3**). These values are comparable to earlier measurements of Cr in groundwater in California serpentinites and other locations, and exceed limits recommended by the World Health Organization (*314*).

Interestingly, analyses of measured physical and chemical data from CROMO fluids lack a strong correlation with Ni and Cr concentrations with the strongest relationship between the heavy metals themselves. While this may seem counterintuitive given the influences of ORP and pH upon metal mobility, an explanation may lie in the lithological variability in the CROMO subsurface and the sources of these metals to groundwater. Each well is emplaced within a relatively isolated lithostratigraphic unit that may influence both heavy metal inputs and local geochemistry. Despite slow fluid flow rates through the CROMO aquifer of 1 km every 300 years, there is connectivity between subsurface habitats that allow for shared physiological adaptations in groundwater microbial communities (*86*). This previous study also showed correlations between the abundance and expression of membrane transport genes, particularly the multiple resistance and pH antiporter *mrp* gene and high pH (*86*, *330*),

While typically these metals are found in stable complexes within the different mineral matrices, the chemistry of pore water can influence metal mobility. Ni and Cr both show increased solubility at high pH, as is typical of serpentinization influenced fluids. Further, metals

may be complexed by hydroxide ions which may enhance solubility. The valence state of transition metals also has a strong influence on metal mobility and toxicity. Chromium for the most part can be found in Cr(III) and Cr(VI) forms, however the former is much less mobile at the alkaline pH found within CROMO, while the latter can both be found as a result of natural oxidation processes as well as industrial inputs and is much more mobile and labile in subsurface pore-waters (*331*). Fluids percolating through serpentine soils are more neutral than the underlying groundwater, while sequestering carbon dioxide into carbonate minerals. At CROMO this may result in a gradient of metal mobility depending on the specific environment and local fluid chemistry (*319, 331*). Seasonal hydrology at CROMO may also play an important role in metal mobility, including strong seasonal wet/dry cycles that periodically saturated the soils, and long fluid residence times in subsurface aquifers. These conditions may result in sustained exposure of subsurface microbial communities to elevated metal concentrations as they are not easily moved out of the system during groundwater recharge (*86, 321*).

Microbial Community Adapted to High Metal Background

From the cores, five samples with archaeal 16S rRNA amplicon sequences and eight samples with bacterial amplicons were compared to existing geochemical and trace metal data. An initial survey of cobalt, chromium and nickel concentrations showed a marked increase in all three with well depth as measured in each of our cored samples (**figure 27**). The total community abundance for bacteria and archaea between both sites shows generally similar make-up with differences in compositional abundance with depth (**figures 28 – 31**). Archaeal amplicons with >1% relative abundance in the samples included members of the Bathyarchaeia, Nitrososphaerales, Methanococcales, and Methanosarcinales and abundant bacteria in the core samples included Actinobacteria, Burkholderiales, and Rhizobiales. No correlations could be

established within our cutoff metrics ($p < 0.05$ and $q < 0.05$), however this might be unsurprising given the large concentration of all three metals overall. Rather, some of the taxa were correlated with less abundant metals including Be, Pb, Au, and Ag- although exploring these relationships in detail is beyond the scope of this study. Geochemical and microbial modeling previously conducted at CROMO highlight the selective pressures imposed by the high alkalinity within the subsurface environment contributing to low diversity communities dominated by well-adapted endemic taxa (*86*). This results in microbial populations that remain consistent over time, with compositional changes likely related to those additional variables secondary to pH. The absence of any correlation is indicative of a largely well adapted community that has already been structured against the metal background, with little notable variability under an already high condition. Many constituents of the community have been previously associated with adaptions to environmental perturbations such as heavy metal contamination. *Cutibacterium* and *Micrococcus* genera are such taxa known to be abundant within soils high in metal content, active oil fields, mining regions and compose notable fraction of the core population at CROMO (*332–336*). Many strains have been in particular isolated for their resistance to chromium, nickel and other heavy metal contaminants and their potential in bioremediation efforts and increasing crop resilience (*337–339*). The family Sphingomonadaceae microbes are another CROMO constituent and are prolific as members of the expansive Proteobacteria phylum, making appearances in nearly every environment. Many strains identified are commonly found in soils and sediments, with a large number regularly identified in ocean environments. In instances of heavy metal contamination or large environmental perturbations, many taxa are enriched in abundance relative to the remaining community (*340–342*). Some species have been studied heavily for metabolic adaptations to these environmental stressors and as such are of great

interest in strategies for mitigating the environmental impacts of toxic industrial wastes or pollution, such as the removal of plastic derived endocrine disruptor bisphenol-A (*343*).

A similar analysis of CROMO fluids collected in May/June 2016 finds very high concentrations of chromium and nickel, with limited data available for cobalt to primarily due to its likely dominance in the solid phase rather than fluid (**figure 32**). In the CROMO groundwater, some of the most abundant taxa included populations related to *Serpentinomonas*, *Dethiobacter*, and *Truepera*, consistent with earlier reports and in some instances composing more than 50% of well sample microbes making them the most dominant in an already low-diversity consortia (**figure 33**) (*320*). Like the core samples, there were no strong correlations between these taxa and heavy metal concentrations, despite the fact that other geochemical parameters (e.g., pH, ORP, well depth) have been shown to influence microbial community composition at the CROMO site. These results may be explained by the pervasively high concentrations of these metals across the site, and the demonstrated connectivity between the aquifers, despite their contrasting physical chemical conditions (*86*). High metal concentrations across the site impact all of the populations in groundwater and rock-hosted environments, despite the local specificities, and demand adaptation to metal stress, as explored further through metagenomic and metatranscriptomic approaches.

Metal Related Genes in the Context of Groundwater Geochemistry

An analysis was carried out comparing metal transporter and resistance genes present in multiple samples of the well fluids from the Quarry Valley (QV) and Core Shed Well (CSW) clusters of CROMO. This included 27 metagenomes and 8 metatranscriptomes from samples collected between 2011 and 2016 and analyzed in previous publications (*24*, *86*, *290*, *320*). Like the analyses of cores, our focus was on chromium and nickel resistance and adaptation. The three

genes of the heavy metal efflux system hitherto called *czcCBA*, function to prevent cell accumulation of cobalt, zinc and cadmium as a unified complex, and confer resistance at different sensitivities to each metal (*344–346*). Analysis of the distribution of the genes involved in the *czc* operon, which can also mediate Ni removal, found that these genes were much more abundant in the metagenomes of the QV well cluster (**figure 34**). The expression of these genes was also found to be differentially more abundant in the QV wells sampled. The genes *nrsD/nreB* and *rcnA* confer nickel and cobalt resistance, respectively, in a feedback loop increasing nickel efflux activity, with the latter exerting control of efflux on both metals (*347*, *348*). Higher *nrsD/nreB* detections were found in the CSW wells and in a profile through the water column of CSW1.1, which may reflect the relative abundance of the genus *Truepera* in these wells.

nikA/*cntA* (K15584) codes for a necessary nickel binding protein component of the nikABCDE nickel transporter complex, critical for uptake and incorporation of the metal in an array of metalloenzymes (*349*). This gene was prevalent across many of the CSW and QV wells, with higher abundances in metagenomes of the QV well cluster. Curiously, the highest expression of *nikA* was found in the CSWold well, the deepest well with the highest abundance of the genus Dethiobacter a widespread anaerobe that utilizes the Wood-Ljungdahl pathway for acetogenesis.. Paradoxically, high nickel concentrations (>200ppm) have been shown to limit or entirely inhibit *nikA* activity (*350*). Consequently, organisms must balance Ni uptake for utilization against its toxicity.

hoxN/nixA (K07241)transports internally bioavailable nickel and is considered to be highly efficient in environmental nickel removal (*351*). This gene was found to be most abundant in the moderately alkaline wells (pH 9-10), that also had some of the consistently highest Ni

levels at the site, generally >500 ppb. ABC.PE.S (K02035), a combined nickel/peptide transporter showed the highest detection levels of any metal-responsive gene in the dataset, particularly in the extremely high pH CSW1.1 fluids This gene codes for a membrane bound protein mediating biding nickel binding for cellular uptake (*352*). And was found in MAGs of all 3 of the major taxa at the site.

Although relatively few known chromium related genes were detected in the metagenomic dataset, the chromate transporter (*chrA*) was found to be common is across all the high pH wells of CROMO. All three of the major taxa across the CROMO wells were found to contain *chrA*. This gene was particularly highly expressed in the QV1,1 well. Interestingly, QV1,1 had some of the lowest measured chromium concentrations, potentially indicating active chromate reduction and immobilization relative to other wells.

Although we did not directly measure dissolved cobalt in this study, Co is known to be enriched in serpentinization influence fluids, as is critical as a metal cofactor. We examined key genes involved in cobalt metabolism in the metagenomic dataset. The genes *cbiK, cbiL* and *cbiN* are key constituents of prokaryotic cobalt chelation and the cobalamin synthesis pathway, with *cbiK* (*353, 354*). Notably, *cbiK* can encode for different serotypes targeting different metals for chelation, such as cobalt in the cytoplasmic space and iron in the periplasmic space cells (*355*). *cbiN* codes for a required member of the cobalt chelation complex and may be a secondary indication of increased cobalt uptake activity (*356*). These genes were generally more abundant in the moderate pH well CSWold, and the wells of the QV cluster. In contrast, *tlyC* (K03699) a putative magnesium / cobalt exporter shows elevated detection levels in the hyperalkaline (pH >12) groundwater of the CSW1,1 well as was found in all of the major taxa. These findings point

to the balance between metal uptake to sustain enzymatic activity and metal efflux to mediate metal toxicity across the site.

An examination of metal resistance genes in the context of 3 of the major taxa found at CROMO, *Serpentinomonas*, *Truepera*, and *Dethiobacter*, was conducted to better understand the relationship between metals and other physiological features. An earlier study outlined key metabolic and physiological traits for these taxa using MAGs (*172*). In brief, some metal resistance genes were found to be restricted to groups of organisms, such ABC transporters related to nickel in *Dethiobacter*, and heavy metal efflux systems in *Serpentinomonas* (**Table A.4**). The abundance of these genes as compared to the physical-chemical characteristics of the groundwater was consistent with what is known about the physiology of these species; that Dethiobacter is favored in more reducing, deeper parts of the ecosystem, whereas Serpentinomonas thrives at an interface environment. On the other hand, some metal resistance mechanisms were present in all three of the major taxonomic groups and were in high abundance in environmental samples. These include the substrate binding Nickel-peptide transport system, and the chromate transporter *chrA* genes.

The data suggests a greater metal response in QV fluids despite higher detected metals in the CSW wells for nickel. In the limited analysis of these metal related genes, what becomes apparent is an inherent redundancy in metal resistance and adaptation at work within the serpentinite environment. These data hint at a fine balance between utilizing a rich source of biochemically necessary transition metals while preventing their cytotoxic effects. The appearance of multiple nickel and cobalt transporters that may function similarly, even if with less sensitivity, on other metals could be representative of a complex adaptive strategy for survival in otherwise toxic environments (*357*). Overall, the occurrence and expression of metal

resistance genes across the major taxonomic groups at the site, coupled with high *in situ* metal concentrations, points to the requirement and likely demands of these genes for survival in the serpentinite subsurface habitat.

Broader Implications for Environmental Health and Remediation

Serpentine landscapes contain some of the highest soil metal concentrations measured, particularly for the metals Ni, Cr, and Co, yet host well-adapted and long-lived ecosystems. This community of microscopic and macroscopic organisms have deployed strategies for the cycling and removal of metals for their own survival against an already unique backdrop of pH stress and nutrient limitation. While our analysis was restricted in scope, it highlights the potential for delineating the most sensitive organisms and adaptations to the metal variables analyzed. Some may function as indicators of toxicity and soil health, such as we found related to high nickel and chromium concentrations, or it may highlight where further information is needed on the mechanism and distribution of metal resistance processes. The long-term effects of metal accumulation in soils or how they will be exacerbated with the changing global climate are only now being studied. Altered seasonal precipitation, decreased nutrient turnover, increased erosion and release of previously buried carbon deposits are all bound to impact metal mobility and accumulation in serpentine landscapes. Early indicators of health of these systems via their changing microbial community population would serve not only as metrics for maintaining health, but also as a toolbox for enhancing the soil productivity and resilience of at-risk ecosystems.

With the increasing deposition of industrial waste products into the environment and its compounded effects on soil and faunal health taking place at times over generations, it is critical to identify strategies for mitigating their effects before any catastrophic thresholds are reached.

Increasingly, microbes capable of breaking down pollutants into inert products are being found in soils and sludge ecosystems in part due to higher throughput sequencing efforts and lowered sampling and analysis costs. While many microorganisms continue to evade cultivation, their biochemical responses to the different pollutants are of critical interest, and absent an ability to classically test their metabolic activity, changes in their abundance or gene expression within the very environment they are found become a great utility in identifying novel response targets for further study towards bioremediation. Even without organisms in culture, genes and pathways identified through metagenomic approaches may be integrated through synthetic biology into chassis organisms that can be used in metal extraction and remediation. This has yielded a rapidly growing body of work aimed at extracting and purifying gene products as tools in environmental remediation and in engineering more resilient agricultural products. Understanding microbial adaptations to these extreme environments adds to the toolbox of potential strategies that can be used to overcome the environmental challenges of present and future.

Tables

Table 8 - A comparison of ICP-MS detected metal range between all available CROMO fluid samples.

Well	Cr 52 (ppb)	Ni 60 (ppb)
CSW 1,1	130	526
CSW 1,1	16	67
CSW 1,2	16.3	79.2
CSW 1,2	16	95.3
CSW 1,3	17.2	132
CSW 1,3	16	80.6
CSW 1,4	133	546
CSW 1,4	131	540
CSW 1,5	16	79.5
CSW 1,5	18.9	79.5
CSW OLD	139	589
CSW OLD	26.5	139
N08A	138	629
N08A	132	587
N08B	20.8	79.8
N08B	15.2	78.6
N08C	128	567
N08C	17.5	74.1
QV 1,2	129	514
QV 1,2	133	533
QV 1,3	131	531
QV 1,3	131	542
QV 1,1	16.2	154
QV 1,1	16.7	154

Table 9 - Sample depth and metal concentrations as detected in selected cores subset.

Core Sample	Avg Depth (cm)	Zr (ppm)	Sr (ppm)	Rb (ppm)	Pb (ppm)	Zn (ppm)	Ni (ppm)	Ca (ppm)	Fe (ppm)	Mn (ppm)	Cr (ppm)	V (ppm)	Ti (ppm)	Th (ppm)	As (ppm)	Cu (ppm)	Co (ppm)
CSW1R	Surface	104	105	26	0	49	128	5166	33183	322	149	104	2207	-	-	-	-
CSW2R	Surface	168	538	18	0	51	413	42418	66822	1177	1280	206	3779	-	-	-	-
CSW10R	1910	0	124	0	0	0	3754	8277	53873	866	1827	85	752	-	-	-	-
QV30R	3083	91	238	20	0	52	0	21510	61192	1592	58	254	4193	0	10	40	0
QV42R	4329	0	12	0	0	0	2403	443	48289	642	2450	0	129	-	-	-	-

Table 10 - A survey of typical metal concentrations found in groundwater, soils and in serpentinite environments. Included are the permissible levels recommended by the World Health Organization (WHO) and Regulatory Guidance Values (RGV) that are commonly used across multiple regulatory agencies, though are less stringent than WHO (*281*, *358–362*).

Category	Ni	Cr	Co
Typical Groundwater	2 ppb	2 - 10 ppb	<1 ppb
Serpentinite Groundwater	up to 51 ppb	25 - 172 ppb	30 - 74 ppb
Typical Soils	3 - 1000 ppm	<500 ppm	1 - 17 ppm
Serpentinite Soils	1993 ppm	2753 ppm	>100 ppm
RGV Permissible Levels	112 ppm	250 ppm	50 ppm
WHO Permissible Levels	20 ppb	50 ppb	40 ppb

Figures

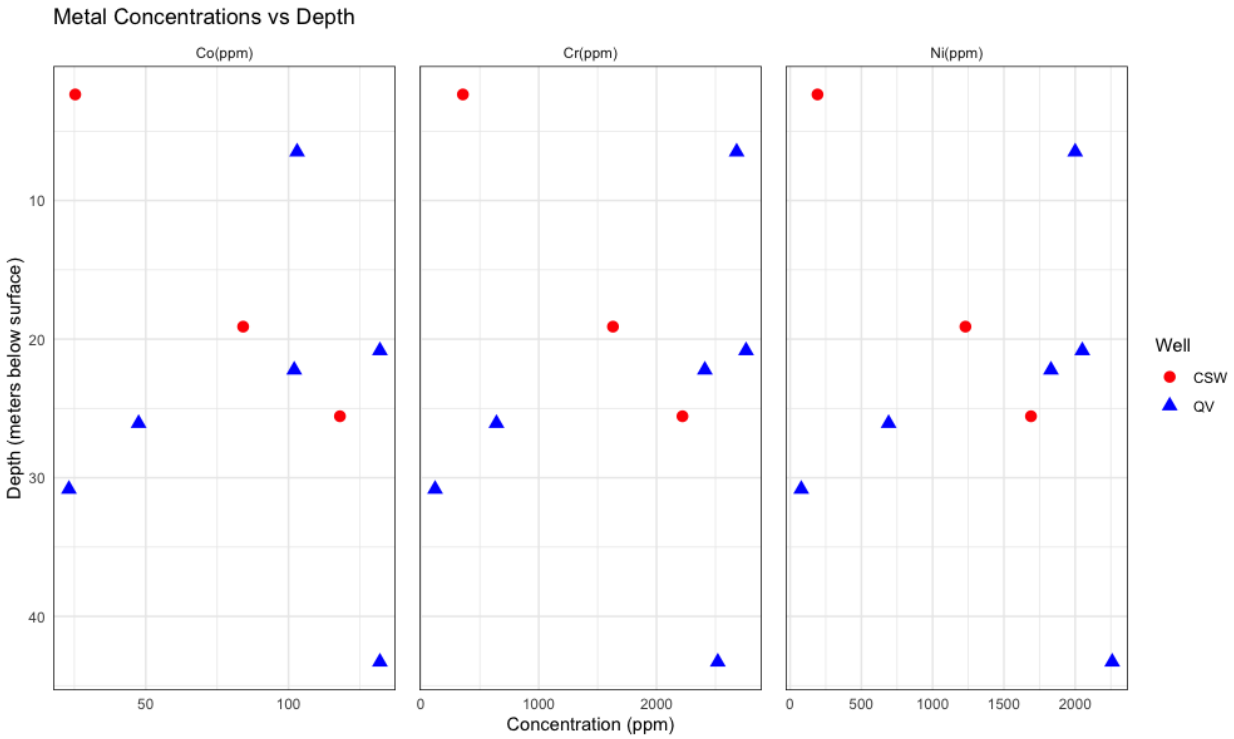

Figure 27 - Well cores showing increased concentrations of cobalt, chromium and nickel with depth between CSW and QV wells.

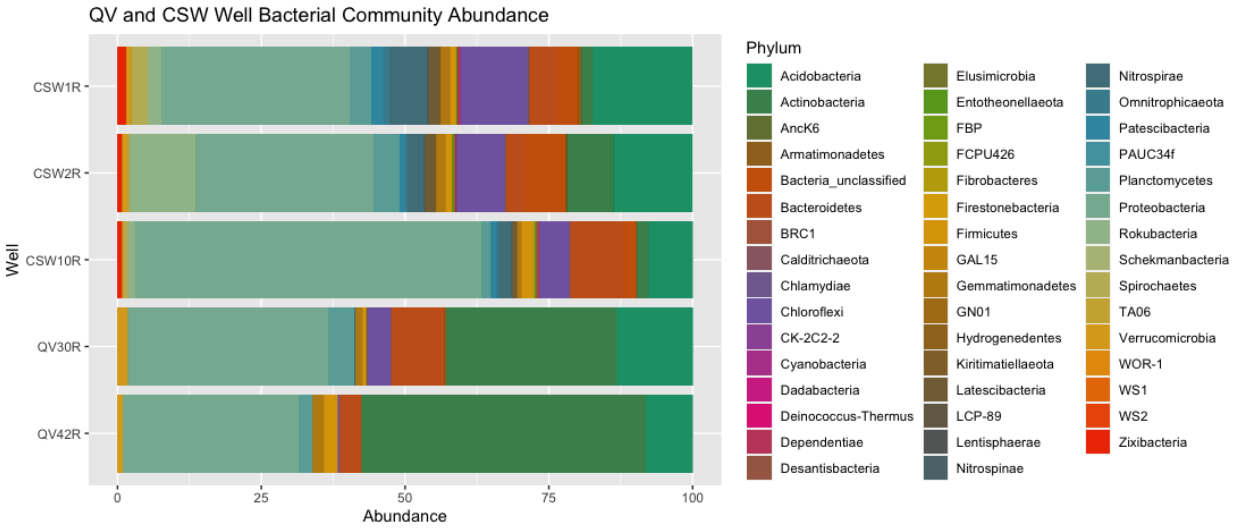

Figure 28 - A survey of bacterial phyla abundance and comparison between each core sample.

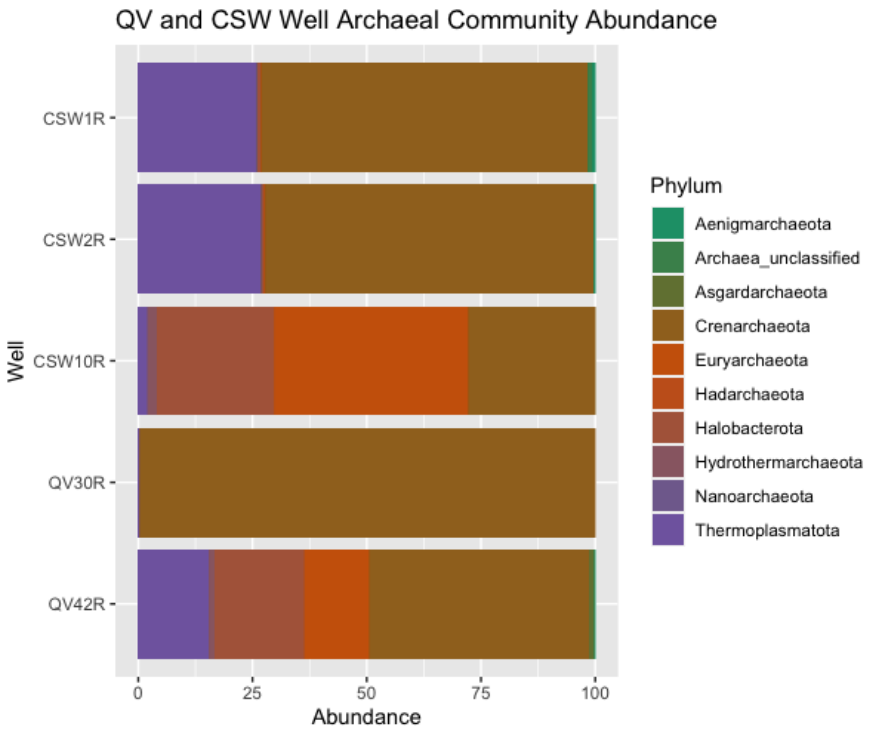

Figure 29 - Archaeal community phyla abundance compared between each core sample.

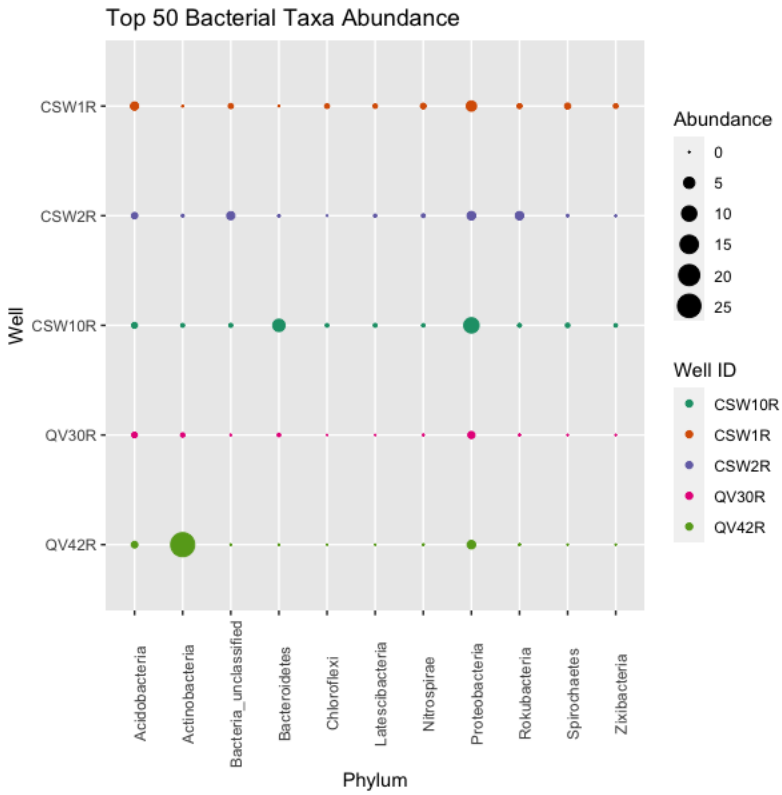

Figure 30 - The top 50 bacteria taxa showing their total relative phyla count percent abundance between each core sample.

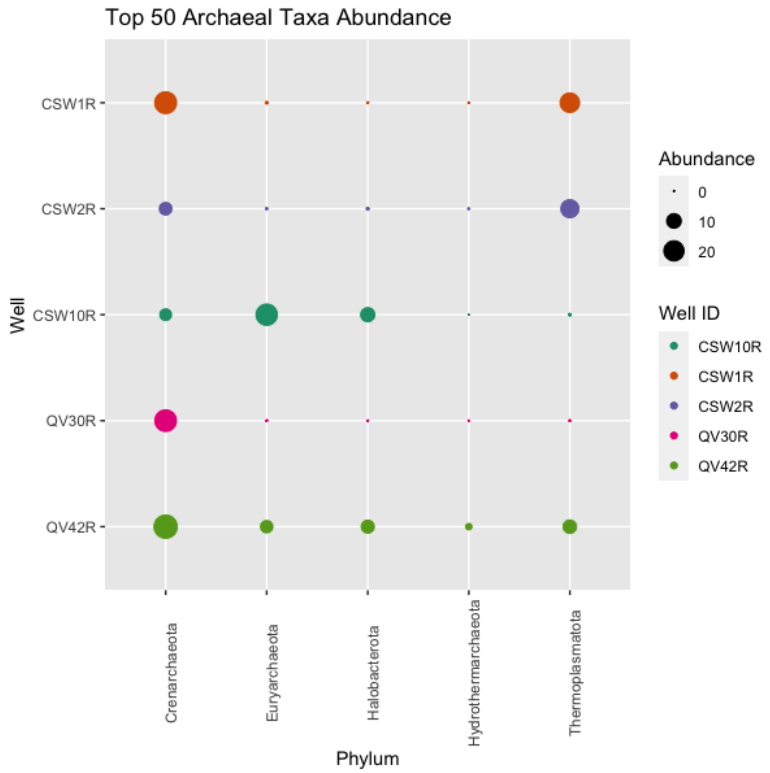

Figure 31 - The top 50 archaeal taxa showing their total relative phyla count percent abundance between each core sample.

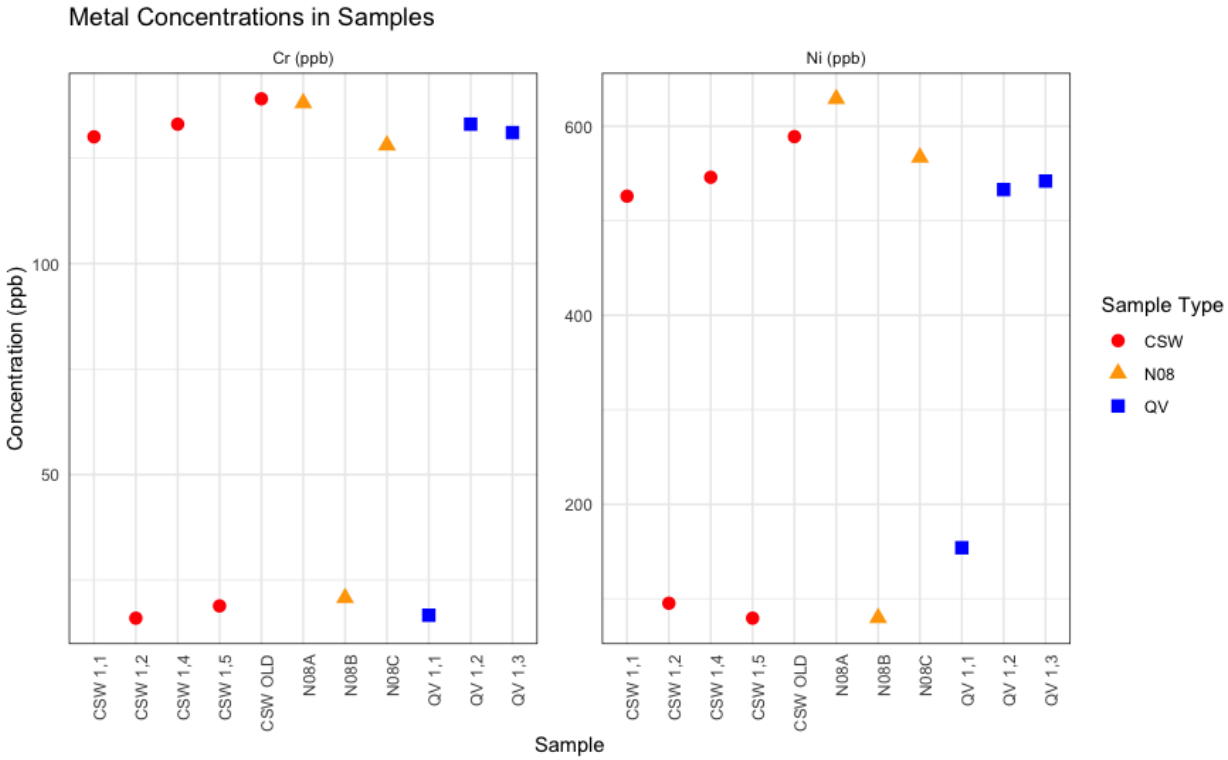

Figure 32 - Chromium and nickel concentrations measured in all the well fluids from CSW, N08 and QV wells across CROMO showing relatively high levels in most samples.

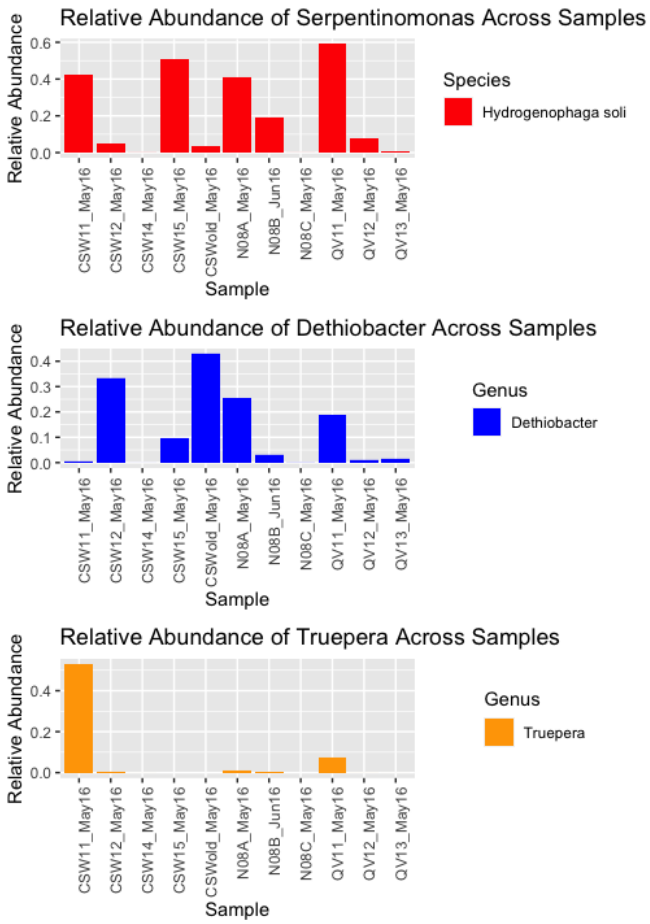

Figure 33 - The most dominant taxa in CROMO fluids are Serpentinomonas (previously classified as Hydrogenophaga soli), Dethiobacter and Truepera that in some samples compose over 50% of the population in an already low-diversity setting.

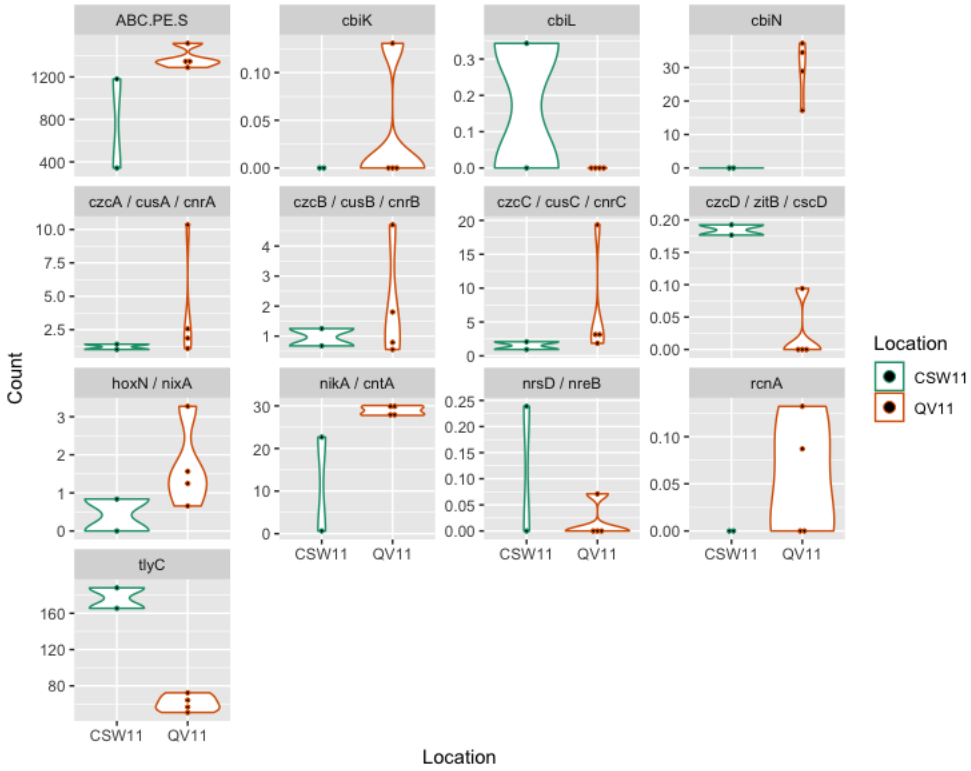

Figure 34 - A comparison of identified metal responsive genes and their counts (FPKM) in CSW and QV fluid samples.

FUTURE WORK

This work contributes important knowledge related to the habitat characteristics and microbial ecology of rocks associated with serpentinization, which may comprise vast portions of Earth's deep biosphere. Serpentinization provides prolific fuel for microbial communities, such as hydrogen and carbon liberated from the Earth's mantle but can also challenge organisms with hyperalkaline pH, low dissolved inorganic carbon concentrations, low concentrations of potential oxidants, and both metal limitation and metal stress (*24*, *86*). In extreme environments, like those associated with serpentinization, survival and growth is a precarious balance between energy and resource supply and demand, which becomes complicated by their delivery through fractal and heterogeneous pore networks (*2*). As such, it is critical to understand micro-scale habitat characteristics that may shape the distribution of microbial communities within rock-hosted environments, which has implications for the habitability of the deep biosphere writ large (*30*).

Throughout this research, we combined microscopic and metagenomic approaches to infer the relationship between microorganisms and their environment, moving towards higher resolution understanding of their *in-situ* locales. This was all nested against the clues that mineralogy and trace metal geochemistry provide about environmental context in rock-hosted environments, such as contact with recent hydrothermal fluid flow. Microbial communities within active hydrothermal chimney structures were shown to be enriched along regions of active hydrothermal fluid emissions, and their metabolic capabilities reflected utilization of hydrothermally derived energy sources. Additionally, trace metals were found to coincide with regions of elevated biofilm density, pointing to the importance of these metals as enzymatic co-factors. This idea was further supported by examination of metagenomic data from the same

samples that showed the occurrence of genes related to the transport and utilization of these specific samples. In contrast, microbial communities in an ophiolite complex, that could be considered analogous to the rock at the base of the LCHF system, showed evidence of metal stress that was reflected in the efflux systems and resistance mechanisms present at the site. Together, this work shows that local conditions, including pore structure, mineralogy, and trace metals can strongly influence the diversity and distribution of microorganisms in natural rock-hosted habitats.

Future work based upon this research would comprise many different areas of investigation. For one, metal enriched pore spaces in carbonate hydrothermal chimneys like the LCHF are key components of leading origins-of-life theories (*204*, *363*, *364*). It would be valuable to compare, in detail, the mineralogy and metal chemistry around pore spaces at the LCHF to these theoretical models, using techniques such as high-resolution TEM and synchrotron-based methods, in addition to determining their relationships to organic deposition, accumulation and oligomerization. Additionally, it would be valuable to carry out detailed phylogenetic studies of genes with a high metal demand within the LCHF chimneys to study evolution and diversification, particularly their lateral transfer pathways that led to their conservation and evolution. Earlier work showed a high diversity of nitrogenases and transposases with the LCHF metagenomes, despite very low taxonomic diversity (*55*). It would be valuable to determine whether these diverse functional genes reflected different trace metal utilization patterns, or the versality to use multiple metal co-factors to carry out the same process and the factors determining metal choice. The observations of microbe-metal and microbe-mineral relationships could also be used to guide new cultivation strategies from the LCHF, as to-date (over the past 20 years) efforts have been largely unsuccessful. In the ophiolitic system,

different questions remain, such as “Does the ability to detoxify heavy metals limit microbial taxonomic diversity?” It is also interesting to consider whether metal resistance genes are horizontally transferred between microbial communities in serpentinizing ophiolites, and whether the same resistance mechanisms are used in different ophiolitic complexes worldwide. Finally, the heterogeneous distribution and formation of biofilms within pore-spaces may also depend on physical environmental signals such as fluid flow, turbulence or local topography. How this, combined with the chemical microenvironment convert to attachment and growth signals remain to be studies in extreme systems such as these, and may shed light on the complex array of environmental factors that lead a microbe to select one location or another to colonize.

Overall, this work contributes important information relevant to the understanding of microbial ecology in rock-hosted geologic environments, particularly those associated with serpentinization. This is important to our consideration of both the extent of life on Earth, but also the pre-photosynthesis early evolution of the biosphere, and the possibility of life elsewhere. Knowing specifically how microorganisms are adapted to their environment, and their interaction with inorganic metals and mineral complexes will help us more fully understand the extent of habitability as well as the signatures of biological processes in these confounding systems.

BIBLIOGRAPHY

1. N. Merino, H. S. Aronson, D. P. Bojanova, J. Feyhl-Buska, M. L. Wong, S. Zhang, D. Giovannelli, Living at the Extremes: Extremophiles and the Limits of Life in a Planetary Context. *Front. Microbiol.* **10**, 780 (2019).

2. T. M. Hoehler, B. B. Jørgensen, Microbial life under extreme energy limitation. *Nat. Rev. Microbiol.* **11**, 83–94 (2013).

3. L. J. Rothschild, R. L. Mancinelli, Life in extreme environments. *Nature* **409**, 1092–1101 (2001).

4. F. Canganella, J. Wiegel, Extremophiles: from abyssal to terrestrial ecosystems and possibly beyond. *Sci. Nat.* **98**, 253–279 (2011).

5. S. M. Soucy, J. Huang, J. P. Gogarten, Horizontal gene transfer: building the web of life. *Nat. Rev. Genet.* **16**, 472–482 (2015).

6. C. Magnabosco, L.-H. Lin, H. Dong, M. Bomberg, W. Ghiorse, H. Stan-Lotter, K. Pedersen, T. L. Kieft, E. van Heerden, T. C. Onstott, The biomass and biodiversity of the continental subsurface. *Nat. Geosci.* **11**, 707–717 (2018).

7. R. L. Mancinelli, T. F. Fahlen, R. Landheim, M. R. Klovstad, Brines and evaporites: analogs for Martian life. *Adv. Space Res.* **33**, 1244–1246 (2004).

8. C. C. Porco, L. Dones, C. Mitchell, Could It Be Snowing Microbes on Enceladus? Assessing Conditions in Its Plume and Implications for Future Missions. *Astrobiology* **17**, 876–901 (2017).

9. D. Deamer, B. Damer, Can Life Begin on Enceladus? A Perspective from Hydrothermal Chemistry. *Astrobiology* **17**, 834–839 (2017).

10. C. Oze, M. Sharma, Serpentinization and the inorganic synthesis of H2 in planetary surfaces. *Icarus* **186**, 557–561 (2007).

11. N. G. Holm, C. Oze, O. Mousis, J. H. Waite, A. Guilbert-Lepoutre, Serpentinization and the Formation of H2 and CH4 on Celestial Bodies (Planets, Moons, Comets). *Astrobiology* **15**, 587–600 (2015).

12. C. Neal, G. Stanger, Calcium and magnesium hydroxide precipitation from alkaline groundwaters in Oman, and their significance to the process of serpentinization. *Mineral. Mag.* **48**, 237–241 (1984).

13. D. S. Kelley, J. A. Karson, G. L. Früh-Green, D. R. Yoerger, T. M. Shank, D. A. Butterfield, J. M. Hayes, M. O. Schrenk, E. J. Olson, G. Proskurowski, M. Jakuba, A. Bradley, B. Larson, K. Ludwig, D. Glickson, K. Buckman, A. S. Bradley, W. J. Brazelton, K. Roe, M. J. Elend, A. Delacour, S. M. Bernasconi, M. D. Lilley, J. A. Baross, R. E.

Summons, S. P. Sylva, A serpentinite-hosted ecosystem: the Lost City hydrothermal field. *Science* **307**, 1428–1434 (2005).

14. O. Plümper, H. E. King, T. Geisler, Y. Liu, S. Pabst, I. P. Savov, D. Rost, T. Zack, Subduction zone forearc serpentinites as incubators for deep microbial life. *Proc. Natl. Acad. Sci. U. S. A.* **114**, 4324–4329 (2017).

15. S. Q. Lang, G. L. Früh-Green, S. M. Bernasconi, W. J. Brazelton, M. O. Schrenk, J. M. McGonigle, Deeply-sourced formate fuels sulfate reducers but not methanogens at Lost City hydrothermal field. *Sci. Rep.* **8**, 755 (2018).

16. M. J. Russell, A. J. Hall, W. Martin, Serpentinization as a source of energy at the origin of life: Serpentinization and the emergence of life. *Geobiology* **8**, 355–371 (2010).

17. M. Schulte, D. Blake, T. Hoehler, T. McCollom, Serpentinization and its implications for life on the early Earth and Mars. *Astrobiology* **6**, 364–376 (2006).

18. D. Z. Oehler, G. Etiope, Methane Seepage on Mars: Where to Look and Why. *Astrobiology* **17**, 1233–1264 (2017).

19. C. R. Glein, F. Postberg, S. D. Vance, "The Geochemistry of Enceladus: Composition and Controls" in *Enceladus and the Icy Moons of Saturn* (The University of Arizona Press, 2018).

20. P. M. Schenk, R. N. Clark, C. J. A. Howett, A. J. Verbiscer, J. Hunter Waite, *Enceladus and the Icy Moons of Saturn* (University of Arizona Press, 2018)vol. 24.

21. M. O. Schrenk, W. J. Brazelton, S. Q. Lang, Serpentinization, Carbon, and Deep Life. *Reviews in Mineralogy and Geochemistry* **75**, 575–606 (2013).

22. L. Preiss, D. B. Hicks, S. Suzuki, T. Meier, T. A. Krulwich, Alkaliphilic bacteria with impact on industrial applications, concepts of early life forms, and bioenergetics of ATP synthesis. *Front. Bioeng. Biotechnol.* **3**, 75 (2015).

23. S. Suzuki, J. G. Kuenen, K. Schipper, S. van der Velde, S. Ishii, A. Wu, D. Y. Sorokin, A. Tenney, X. Meng, P. L. Morrill, Y. Kamagata, G. Muyzer, K. H. Nealson, Physiological and genomic features of highly alkaliphilic hydrogen-utilizing Betaproteobacteria from a continental serpentinizing site. *Nat. Commun.* **5**, 3900 (2014).

24. L. M. Seyler, W. J. Brazelton, C. McLean, L. I. Putman, A. Hyer, M. D. Y. Kubo, T. Hoehler, D. Cardace, M. O. Schrenk, Carbon assimilation strategies in ultrabasic groundwater: Clues from the integrated study of a serpentinization-influenced aquifer. *mSystems* **5** (2020).

25. I. A. Berg, D. Kockelkorn, W. H. Ramos-Vera, R. F. Say, J. Zarzycki, M. Hügler, B. E. Alber, G. Fuchs, Autotrophic carbon fixation in archaea. *Nat. Rev. Microbiol.* **8**, 447–460 (2010).

26. J. B. Glass, V. J. Orphan, Trace metal requirements for microbial enzymes involved in the production and consumption of methane and nitrous oxide. *Front. Microbiol.* **3**, 61 (2012).

27. A. Farough, D. E. Moore, D. A. Lockner, R. P. Lowell, Evolution of fracture permeability of ultramafic rocks undergoing serpentinization at hydrothermal conditions: An experimental study. *Geochem. Geophys. Geosyst.* **17**, 44–55 (2016).

28. K. Junge, H. Eicken, J. W. Deming, Bacterial Activity at -2 to -20 degrees C in Arctic wintertime sea ice. *Appl. Environ. Microbiol.* **70**, 550–557 (2004).

29. Z. S. Cooper, J. Z. Rapp, S. D. Carpenter, G. Iwahana, H. Eicken, J. W. Deming, Distinctive microbial communities in subzero hypersaline brines from Arctic coastal sea ice and rarely sampled cryopegs. *FEMS Microbiol. Ecol.* **95**, fiz166 (2019).

30. Y. Suzuki, S. Yamashita, M. Kouduka, Y. Ao, H. Mukai, S. Mitsunobu, H. Kagi, S. D'Hondt, F. Inagaki, Y. Morono, T. Hoshino, N. Tomioka, M. Ito, Deep microbial proliferation at the basalt interface in 33.5-104 million-year-old oceanic crust. *Commun. Biol.* **3**, 136 (2020).

31. J. Leloup, A. Loy, N. J. Knab, C. Borowski, M. Wagner, B. B. Jørgensen, Diversity and abundance of sulfate-reducing microorganisms in the sulfate and methane zones of a marine sediment, Black Sea. *Environmental Microbiology* **9**, 131–142 (2007).

32. B. J. Baker, C. S. Lazar, A. P. Teske, G. J. Dick, Genomic resolution of linkages in carbon, nitrogen, and sulfur cycling among widespread estuary sediment bacteria. *Microbiome* **3**, 14 (2015).

33. C. T. Skennerton, K. Chourey, R. Iyer, R. L. Hettich, G. W. Tyson, V. J. Orphan, Methane-Fueled Syntrophy through Extracellular Electron Transfer: Uncovering the Genomic Traits Conserved within Diverse Bacterial Partners of Anaerobic Methanotrophic Archaea. *MBio* **8**, e00530-17 (2017).

34. S. Bhattarai, C. Cassarini, P. N. L. Lens, Physiology and Distribution of Archaeal Methanotrophs That Couple Anaerobic Oxidation of Methane with Sulfate Reduction. *Microbiol Mol Biol Rev* **83** (2019).

35. M. Thommes, T. Wang, Q. Zhao, I. C. Paschalidis, D. Segrè, Designing metabolic division of labor in microbial communities, *bioRxiv* (2018)p. 442376.

36. R. Tsoi, F. Wu, C. Zhang, S. Bewick, D. Karig, L. You, Metabolic division of labor in microbial systems. *Proc. Natl. Acad. Sci. U. S. A.* **115**, 2526–2531 (2018).

37. S. Kato, K. Nakamura, T. Toki, J.-I. Ishibashi, U. Tsunogai, A. Hirota, M. Ohkuma, A. Yamagishi, Iron-based microbial ecosystem on and below the seafloor: a case study of hydrothermal fields of the southern mariana trough. *Front. Microbiol.* **3**, 89 (2012).

38. A.-E. Rotaru, P. M. Shrestha, F. Liu, B. Markovaite, S. Chen, K. P. Nevin, D. R. Lovley, Direct interspecies electron transfer between Geobacter metallireducens and Methanosarcina barkeri. *Appl. Environ. Microbiol.* **80**, 4599–4605 (2014).

39. G. Wegener, V. Krukenberg, D. Riedel, H. E. Tegetmeyer, A. Boetius, Intercellular wiring enables electron transfer between methanotrophic archaea and bacteria. *Nature* **526**, 587–590 (2015).

40. F. Wang, Y. Gu, J. P. O'Brien, S. M. Yi, S. E. Yalcin, V. Srikanth, C. Shen, D. Vu, N. L. Ing, A. I. Hochbaum, E. H. Egelman, N. S. Malvankar, Structure of Microbial Nanowires Reveals Stacked Hemes that Transport Electrons over Micrometers. *Cell* **177**, 361-369.e10 (2019).

41. A. Templeton, E. Knowles, Microbial Transformations of Minerals and Metals: Recent Advances in Geomicrobiology Derived from Synchrotron-Based X-Ray Spectroscopy and X-Ray Microscopy. *Annu. Rev. Earth Planet. Sci.* **37**, 367–391 (2009).

42. V. S. Coker, J. M. Byrne, N. D. Telling, G. VAN DER Laan, J. R. Lloyd, A. P. Hitchcock, J. Wang, R. A. D. Pattrick, Characterisation of the dissimilatory reduction of Fe(III)-oxyhydroxide at the microbe-mineral interface: the application of STXM-XMCD: STXM-XMCD of microbial Fe(III)-reduction. *Geobiology* **10**, 347–354 (2012).

43. S. Mitsunobu, M. Zhu, Y. Takeichi, T. Ohigashi, H. Suga, H. Makita, M. Sakata, K. Ono, K. Mase, Y. Takahashi, Nanoscale identification of extracellular organic substances at the microbe–mineral interface by scanning transmission X-ray microscopy. *Chem. Lett.* **44**, 91–93 (2015).

44. K. T. Konstantinidis, J. M. Tiedje, Prokaryotic taxonomy and phylogeny in the genomic era: advancements and challenges ahead. *Curr Opin Microbiol* **10**, 504–509 (2007).

45. D. Chivian, E. L. Brodie, E. J. Alm, D. E. Culley, P. S. Dehal, T. Z. DeSantis, T. M. Gihring, A. Lapidus, L.-H. Lin, S. R. Lowry, D. P. Moser, P. M. Richardson, G. Southam, G. Wanger, L. M. Pratt, G. L. Andersen, T. C. Hazen, F. J. Brockman, A. P. Arkin, T. C. Onstott, Environmental genomics reveals a single-species ecosystem deep within Earth. *Science* **322**, 275–278 (2008).

46. E. A. Franzosa, T. Hsu, A. Sirota-Madi, A. Shafquat, G. Abu-Ali, X. C. Morgan, C. Huttenhower, Sequencing and beyond: integrating molecular "omics" for microbial community profiling. *Nat. Rev. Microbiol.* **13**, 360–372 (2015).

47. T. Samuels, C. Bryce, H. Landenmark, C. Marie-Loudon, N. Nicholson, A. H. Stevens, C. Cockell, "Microbial weathering of minerals and rocks in natural environments" in *Biogeochemical Cycles* (John Wiley & Sons, Inc., Hoboken, NJ, USA, 2020), pp. 59–79.

48. H.-C. Flemming, EPS-Then and Now. *Microorganisms* **4** (2016).

49. A. B. Fulke, A. Kotian, M. D. Giripunje, Marine microbial response to heavy metals: Mechanism, implications and future prospect. *Bull. Environ. Contam. Toxicol.* **105**, 182–197 (2020).

50. S. Yazdi, A. M. Ardekani, Bacterial aggregation and biofilm formation in a vortical flow. *Biomicrofluidics* **6**, 44114 (2012).

51. E. Tsagkari, S. Connelly, Z. Liu, A. McBride, W. T. Sloan, The role of shear dynamics in biofilm formation. *NPJ Biofilms Microbiomes* **8**, 33 (2022).

52. K. Sauer, P. Stoodley, D. M. Goeres, L. Hall-Stoodley, M. Burmølle, P. S. Stewart, T. Bjarnsholt, The biofilm life cycle: expanding the conceptual model of biofilm formation. *Nat. Rev. Microbiol.* **20**, 608–620 (2022).

53. P. Stoodley, K. Sauer, D. G. Davies, J. W. Costerton, Biofilms as Complex Differentiated Communities. *Annu. Rev. Microbiol.* **56**, 187–209 (2002).

54. T. K. Teal, D. P. Lies, B. J. Wold, D. K. Newman, Spatiometabolic Stratification of *Shewanella oneidensis* Biofilms. *Appl Environ Microbiol* **72**, 7324–7330 (2006).

55. W. J. Brazelton, M. P. Mehta, D. S. Kelley, J. A. Baross, Physiological differentiation within a single-species biofilm fueled by serpentinization. *MBio* **2**, 1–9 (2011).

56. J. V. Bailey, V. J. Orphan, S. B. Joye, F. A. Corsetti, Chemotrophic microbial mats and their potential for preservation in the rock record. *Astrobiology* **9**, 843–859 (2009).

57. K. Bemis, R. P. Lowell, A. Farough, On and Around Hydrothermal Vents at Mid-Ocean Ridges. *Oceanography* **25**, 182–191 (2012).

58. G. J. Dick, The microbiomes of deep-sea hydrothermal vents: distributed globally, shaped locally. *Nat. Rev. Microbiol.* **17**, 271–283 (2019).

59. W. Martin, J. Baross, D. Kelley, M. J. Russell, Hydrothermal vents and the origin of life. *Nat. Rev. Microbiol.* **6**, 805–814 (2008).

60. B. Herschy, A. Whicher, E. Camprubi, C. Watson, L. Dartnell, J. Ward, J. R. G. Evans, N. Lane, An origin-of-life reactor to simulate alkaline hydrothermal vents. *J. Mol. Evol.* **79**, 213–227 (2014).

61. B. T. Burcar, L. M. Barge, D. Trail, E. B. Watson, M. J. Russell, L. B. McGown, RNA oligomerization in laboratory analogues of alkaline hydrothermal vent systems. *Astrobiology* **15**, 509–522 (2015).

62. V. Sojo, B. Herschy, A. Whicher, E. Camprubí, N. Lane, The Origin of Life in Alkaline Hydrothermal Vents. *Astrobiology* **16**, 181–197 (2016).

63. L. M. Barge, L. M. White, Experimentally Testing Hydrothermal Vent Origin of Life on Enceladus and Other Icy/Ocean Worlds. *Astrobiology* **17**, 820–833 (2017).

64. L. M. Barge, E. Flores, M. M. Baum, D. G. VanderVelde, M. J. Russell, Redox and pH gradients drive amino acid synthesis in iron oxyhydroxide mineral systems. *Proc. Natl. Acad. Sci. U. S. A.* **116**, 4828–4833 (2019).

65. C. Konn, J. L. Charlou, N. G. Holm, O. Mousis, The production of methane, hydrogen, and organic compounds in ultramafic-hosted hydrothermal vents of the Mid-Atlantic Ridge. *Astrobiology* **15**, 381–399 (2015).

66. T. M. McCollom, C. Donaldson, Generation of Hydrogen and Methane during Experimental Low-Temperature Reaction of Ultramafic Rocks with Water. *Astrobiology* **16**, 389–406 (2016).

67. C. Wang, R. Tao, J. B. Walters, T. Ren, J. Nan, L. Zhang, Deciphering the Origin of Abiotic Organic Compounds on Earth: Review and Future Prospects. *Acta Geologica Sinica (Eng)* **97**, 288–308 (2023).

68. S. Q. Lang, W. J. Brazelton, Habitability of the marine serpentinite subsurface: a case study of the Lost City hydrothermal field. *Philos. Trans. A Math. Phys. Eng. Sci.* **378**, 20180429 (2020).

69. M. C. Weiss, F. L. Sousa, N. Mrnjavac, S. Neukirchen, M. Roettger, S. Nelson-Sathi, W. F. Martin, The physiology and habitat of the last universal common ancestor. *Nat Microbiol* **1**, 16116 (2016).

70. M. Brasier, N. McLoughlin, O. Green, D. Wacey, A fresh look at the fossil evidence for early Archaean cellular life. *Philos. Trans. R. Soc. Lond. B Biol. Sci.* **361**, 887–902 (2006).

71. M. S. Dodd, D. Papineau, T. Grenne, J. F. Slack, M. Rittner, F. Pirajno, J. O'Neil, C. T. S. Little, Evidence for early life in Earth's oldest hydrothermal vent precipitates. *Nature* **543**, 60–64 (2017).

72. K. A. Ludwig, C.-C. Shen, D. S. Kelley, H. Cheng, R. L. Edwards, U–Th systematics and 230Th ages of carbonate chimneys at the Lost City Hydrothermal Field. *Geochim. Cosmochim. Acta* **75**, 1869–1888 (2011).

73. W. J. Brazelton, K. A. Ludwig, M. L. Sogin, E. N. Andreishcheva, D. S. Kelley, C.-C. Shen, R. L. Edwards, J. A. Baross, Archaea and bacteria with surprising microdiversity show shifts in dominance over 1,000-year time scales in hydrothermal chimneys. *Proc. Natl. Acad. Sci. U. S. A.* **107**, 1612–1617 (2010).

74. F. Lartaud, C. T. S. Little, M. de Rafelis, G. Bayon, J. Dyment, B. Ildefonse, V. Gressier, Y. Fouquet, F. Gaill, N. Le Bris, Fossil evidence for serpentinization fluids fueling chemosynthetic assemblages. *Proc. Natl. Acad. Sci. U.S.A.* **108**, 7698–7703 (2011).

75. F. Lartaud, M. de Rafélis, C. T. S. Little, J. Dyment, G. Bayon, B. Ildefonse, N. Le Bris, Ultramafic hydrothermal systems on the Rainbow abyssal hill: a wide variety of active and fossil chemosynthetic habitats. *InterRidge News* **20**, 32–36 (2011).

76. A. Lecoeuvre, B. Ménez, M. Cannat, V. Chavagnac, E. Gérard, Microbial ecology of the newly discovered serpentinite-hosted Old City hydrothermal field (southwest Indian ridge). *ISME J.*, doi: 10.1038/s41396-020-00816-7 (2020).

77. N. Szponar, W. J. Brazelton, M. O. Schrenk, D. M. Bower, A. Steele, P. L. Morrill, Geochemistry of a continental site of serpentinization, the Tablelands Ophiolite, Gros Morne National Park: A Mars analogue. *Icarus* **224**, 286–296 (2013).

78. M. C. Cook, J. G. Blank, A. Rietze, S. Suzuki, K. H. Nealson, P. L. Morrill, A geochemical comparison of three terrestrial sites of serpentinization: The tablelands, the Cedars, and aqua de Ney. *J. Geophys. Res. Biogeosci.* **126**, e2021JG006316 (2021).

79. D. Mège, J. Gurgurewicz, M. Massironi, R. Pozzobon, G. Tognon, M. Pajola, L. L. Tornabene, A. Lucchetti, B. Baschetti, J. M. Davis, E. Hauber, B. De Toffoli, S. Douté, L. Keszthelyi, L. Marinangeli, J. Perry, A. Pommerol, L. Pompilio, A. P. Rossi, F. Seelos, F. Sauro, R. Ziethe, G. Cremonese, N. Thomas, Hydrothermal Alteration of Ultramafic Rocks in Ladon Basin, Mars—Insights From CaSSIS, HiRISE, CRISM, and CTX. *JGR Planets* **128** (2023).

80. Y. Quesnel, C. Sotin, B. Langlais, S. Costin, M. Mandea, M. Gottschalk, J. Dyment, Serpentinization of the martian crust during Noachian. *Earth Planet. Sci. Lett.* **277**, 184–193 (2009).

81. J. J. Marlow, D. E. LaRowe, B. L. Ehlmann, J. P. Amend, V. J. Orphan, The Potential for Biologically Catalyzed Anaerobic Methane Oxidation on Ancient Mars. *Astrobiology* **14**, 292–307 (2014).

82. E. Chassefière, J. Lasue, B. Langlais, Y. Quesnel, Early Mars serpentinization-derived CH_4 reservoirs, H_2-induced warming and paleopressure evolution. *Meteorit & Planetary Scien* **51**, 2234–2245 (2016).

83. C. R. Glein, J. H. Waite, The carbonate geochemistry of Enceladus' ocean. *Geophys. Res. Lett.* **47** (2020).

84. J. M. McGonigle, S. Q. Lang, W. J. Brazelton, Genomic Evidence for Formate Metabolism by Chloroflexi as the Key to Unlocking Deep Carbon in Lost City Microbial Ecosystems, *Appl. Environ. Microbiol.* (2020)p. 831230.

85. W. J. Brazelton, J. M. McGonigle, S. Motamedi, H. L. Pendleton, K. I. Twing, B. C. Miller, W. J. Lowe, A. M. Hoffman, C. A. Prator, G. L. Chadwick, R. E. Anderson, E. Thomas, D. A. Butterfield, K. A. Aquino, G. L. Früh-Green, M. O. Schrenk, S. Q. Lang, Metabolic Strategies Shared by Basement Residents of the Lost City Hydrothermal Field. *Appl. Environ. Microbiol.* **88**, e0092922 (2022).

86. L. I. Putman, M. C. Sabuda, W. J. Brazelton, M. D. Kubo, T. M. Hoehler, T. M. McCollom, D. Cardace, M. O. Schrenk, Microbial Communities in a Serpentinizing Aquifer Are Assembled through Strong Concurrent Dispersal Limitation and Selection. *mSystems* **6**, e0030021 (2021).

87. M. P. Mehta, D. A. Butterfield, J. A. Baross, Phylogenetic Diversity of Nitrogenase (*nifH*) Genes in Deep-Sea and Hydrothermal Vent Environments of the Juan de Fuca Ridge. *Appl Environ Microbiol* **69**, 960–970 (2003).

88. M. P. Mehta, J. A. Baross, Nitrogen fixation at 92 degrees C by a hydrothermal vent archaeon. *Science* **314**, 1783–1786 (2006).

89. E. Frouin, A. Lecoeuvre, F. Armougom, M. O. Schrenk, G. Erauso, Comparative metagenomics highlight a widespread pathway involved in catabolism of phosphonates in marine and terrestrial serpentinizing ecosystems. *mSystems* **7**, e0032822 (2022).

90. M. Crespo-Medina, K. I. Twing, M. D. Y. Kubo, T. M. Hoehler, D. Cardace, T. McCollom, M. O. Schrenk, Insights into environmental controls on microbial communities in a continental serpentinite aquifer using a microcosm-based approach. *Front. Microbiol.* **5**, 604 (2014).

91. E. Frouin, M. Bes, B. Ollivier, M. Quéméneur, A. Postec, D. Debroas, F. Armougom, G. Erauso, Diversity of Rare and Abundant Prokaryotic Phylotypes in the Prony Hydrothermal Field and Comparison with Other Serpentinite-Hosted Ecosystems. *Front. Microbiol.* **9**, 102 (2018).

92. K. J. Edwards, K. Becker, F. Colwell, The Deep, Dark Energy Biosphere: Intraterrestrial Life on Earth. doi: 10.1146/annurev-earth-042711-105500 (2012).

93. E. D. Becraft, M. C. Y. Lau Vetter, O. K. I. Bezuidt, J. M. Brown, J. M. Labonté, K. Kauneckaite-Griguole, R. Salkauskaite, G. Alzbutas, J. D. Sackett, B. R. Kruger, V. Kadnikov, E. van Heerden, D. Moser, N. Ravin, T. Onstott, R. Stepanauskas, Evolutionary stasis of a deep subsurface microbial lineage. *ISME J.* **15**, 2830–2842 (2021).

94. B. E. L. Morris, R. Henneberger, H. Huber, C. Moissl-Eichinger, Microbial syntrophy: interaction for the common good. *FEMS Microbiol. Rev.* **37**, 384–406 (2013).

95. M. J. Russell, A. J. Hall, The emergence of life from iron monosulphide bubbles at a submarine hydrothermal redox and pH front. *J. Geol. Soc. London* **154**, 377–402 (1997).

96. M.-P. Zorzano, G. Martínez, J. Polkko, L. K. Tamppari, C. Newman, H. Savijärvi, Y. Goreva, D. Viúdez-Moreiras, T. Bertrand, M. Smith, E. M. Hausrath, S. Siljeström, K. Benison, T. Bosak, A. D. Czaja, V. Debaille, C. D. K. Herd, L. Mayhew, M. A. Sephton, D. Shuster, J. I. Simon, B. Weiss, N. Randazzo, L. Mandon, A. Brown, M. H. Hecht, J. Martínez-Frías, Present-day thermal and water activity environment of the Mars Sample Return collection. *Sci. Rep.* **14**, 7175 (2024).

97. J. B. Corliss, J. Dymond, L. I. Gordon, J. M. Edmond, R. P. von Herzen, R. D. Ballard, K. Green, D. Williams, A. Bainbridge, K. Crane, T. H. van Andel, Submarine thermal sprirngs on the galapagos rift. *Science* **203**, 1073–1083 (1979).

98. G. L. Früh-Green, D. S. Kelley, M. D. Lilley, M. Cannat, V. Chavagnac, J. A. Baross, Diversity of magmatism, hydrothermal processes and microbial interactions at mid-ocean ridges. *Nature Reviews Earth & Environment* **3**, 852–871 (2022).

99. K. Ding, W. E. Seyfried, Z. Zhang, M. K. Tivey, K. L. Von Damm, A. M. Bradley, The in situ pH of hydrothermal fluids at mid-ocean ridges. *Earth Planet. Sci. Lett.* **237**, 167–174 (2005).

100. K. A. Ludwig, D. S. Kelley, D. A. Butterfield, B. K. Nelson, G. Früh-Green, Formation and evolution of carbonate chimneys at the Lost City Hydrothermal Field. *Geochim. Cosmochim. Acta* **70**, 3625–3645 (2006).

101. S. G. Sander, A. Koschinsky, Metal flux from hydrothermal vents increased by organic complexation. *Nat. Geosci.* **4**, 145–150 (2011).

102. J. A. Resing, P. N. Sedwick, C. R. German, W. J. Jenkins, J. W. Moffett, B. M. Sohst, A. Tagliabue, Basin-scale transport of hydrothermal dissolved metals across the South Pacific Ocean. *Nature* **523**, 200–203 (2015).

103. S. Nakagawa, K. Takai, Deep-sea vent chemoautotrophs: diversity, biochemistry and ecological significance. *FEMS Microbiol. Ecol.* **65**, 1–14 (2008).

104. R. E. Anderson, M. L. Sogin, J. A. Baross, Biogeography and ecology of the rare and abundant microbial lineages in deep-sea hydrothermal vents. *FEMS Microbiol. Ecol.* **91**, 1–11 (2015).

105. M. Jebbar, B. Franzetti, E. Girard, P. Oger, Microbial diversity and adaptation to high hydrostatic pressure in deep-sea hydrothermal vents prokaryotes. *Extremophiles* **19**, 721–740 (2015).

106. D. V. Meier, P. Pjevac, W. Bach, S. Hourdez, P. R. Girguis, C. Vidoudez, R. Amann, A. Meyerdierks, Niche partitioning of diverse sulfur-oxidizing bacteria at hydrothermal vents. *ISME J.* **11**, 1545–1558 (2017).

107. B. Kristall, D. S. Kelley, M. D. Hannington, Growth history of a diffusely venting sulfide structure from the Juan de Fuca Ridge: a petrological and geochemical study. *Geochem. Explor. Environ. Analy.*, doi: 10.1029/2005GC001166 (2006).

108. F. Wang, H. Zhou, J. Meng, X. Peng, L. Jiang, P. Sun, C. Zhang, J. D. Van Nostrand, Y. Deng, Z. He, L. Wu, J. Zhou, X. Xiao, GeoChip-based analysis of metabolic diversity of microbial communities at the Juan de Fuca Ridge hydrothermal vent. *Proc. Natl. Acad. Sci. U. S. A.* **106**, 4840–4845 (2009).

109. H. Harmsen, D. Prieur, C. Jeanthon, Distribution of microorganisms in deep-sea hydrothermal vent chimneys investigated by whole-cell hybridization and enrichment culture of thermophilic subpopulations. *Appl. Environ. Microbiol.* **63**, 2876–2883 (1997).

110. K. Takai, T. Komatsu, F. Inagaki, K. Horikoshi, Distribution of archaea in a black smoker chimney structure. *Appl. Environ. Microbiol.* **67**, 3618–3629 (2001).

111. M. O. Schrenk, D. S. Kelley, J. R. Delaney, J. A. Baross, Incidence and diversity of microorganisms within the walls of an active deep-sea sulfide chimney. *Appl. Environ. Microbiol.* **69**, 3580–3592 (2003).

112. D. Prieur, Microbiology of deep-sea hydrothermal vents. *Trends in Biotechnology* **15**, 242–244 (1997).

113. M. Gadanho, J. P. Sampaio, Occurrence and diversity of yeasts in the mid-atlantic ridge hydrothermal fields near the Azores Archipelago. *Microb. Ecol.* **50**, 408–417 (2005).

114. R. Wirth, Colonization of Black Smokers by Hyperthermophilic Microorganisms. *Trends Microbiol* **25**, 92–99 (2017).

115. Y.-W. Zhong, P. Zhou, H. Cheng, Y.-D. Zhou, J. Pan, L. Xu, M. Li, C.-H. Tao, Y.-H. Wu, X.-W. Xu, Metagenomic Features Characterized with Microbial Iron Oxidoreduction and Mineral Interaction in Southwest Indian Ridge. *Microbiol Spectr* **10**, e0061422 (2022).

116. V. Chavagnac, G. Ceuleneer, C. Monnin, B. Lansac, G. Hoareau, C. Boulart, Mineralogical assemblages forming at hyperalkaline warm springs hosted on ultramafic rocks: A case study of Oman and Ligurian ophiolites. *Geochem. Geophys. Geosyst.* **14**, 2474–2495 (2013).

117. B. M. Tutolo, A. J. Luhmann, N. J. Tosca, W. E. Seyfried, Serpentinization as a reactive transport process: The brucite silicification reaction. *Earth Planet. Sci. Lett.* **484**, 385–395 (2018).

118. K. A. Aquino, G. L. Fruh-Green, S. M. Bernasconi, Fluid mixing and spatial geochemical variability in the Lost City hydrothermal field chimneys. *Authorea*, doi: 10.22541/essoar.168286676.60387966 (2023).

119. K. A. Aquino, G. L. Fruh-Green, S. M. Bernasconi, Linking mineral formation and microbes in high pH fluids: Constraints from the Lost City hydrothermal field. *Authorea*, doi: 10.22541/essoar.168286823.37608718 (2023).

120. W. J. Brazelton, M. O. Schrenk, D. S. Kelley, J. A. Baross, Methane- and sulfur-metabolizing microbial communities dominate the Lost City hydrothermal field ecosystem. *Appl. Environ. Microbiol.* **72**, 6257–6270 (2006).

121. M. Takashima, K. Shimada, R. E. Speece, Minimum requirements for trace metals (iron, nickel, cobalt, and zinc) in thermophilic and mesophilic methane fermentation from glucose. *Water Environ. Res.* **83**, 339–346 (2011).

122. J. Schijf, E. A. Christenson, R. H. Byrne, YREE scavenging in seawater: A new look at an old model. *Mar. Chem.* **177**, 460–471 (2015).

123. J. Zwicker, D. Smrzka, I. Vadillo, P. Jiménez-Gavilán, M. Giampouras, J. Peckmann, W. Bach, Trace and rare earth element distribution in hyperalkaline serpentinite-hosted spring waters and associated authigenic carbonates from the Ronda peridotite. *Applied Geochemistry* **147**, 105492 (2022).

124. P. Vasudevan, V. Padmavathy, S. C. Dhingra, Biosorption of monovalent and divalent ions on baker's yeast. *Bioresour. Technol.* **82**, 285–289 (2002).

125. J. Samuel, M. L. Paul, M. Pulimi, M. J. Nirmala, N. Chandrasekaran, A. Mukherjee, Hexavalent Chromium Bioremoval through Adaptation and Consortia Development from Sukinda Chromite Mine Isolates. *Ind. Eng. Chem. Res.* **51**, 3740–3749 (2012).

126. E. S. Boyd, A. M. G. Costas, T. L. Hamilton, F. Mus, J. W. Peters, Evolution of molybdenum nitrogenase during the transition from anaerobic to aerobic metabolism. *J. Bacteriol.* **197**, 1690–1699 (2015).

127. M. Fadel, N. M. Hassanein, M. M. Elshafei, A. H. Mostafa, M. A. Ahmed, H. M. Khater, Biosorption of manganese from groundwater by biomass of Saccharomyces cerevisiae. *HBRC Journal* **13**, 106–113 (2017).

128. F. Mus, D. R. Colman, J. W. Peters, E. S. Boyd, Geobiological feedbacks, oxygen, and the evolution of nitrogenase. *Free Radic. Biol. Med.* **140**, 250–259 (2019).

129. J. Liang, Y. Bai, Y. Men, J. Qu, Microbe-microbe interactions trigger Mn(II)-oxidizing gene expression. *ISME J.* **11**, 67–77 (2017).

130. T. M. McCollom, E. L. Shock, Geochemical constraints on chemolithoautotrophic metabolism by microorganisms in seafloor hydrothermal systems. *Geochim. Cosmochim. Acta* **61**, 4375–4391 (1997).

131. D. Bianchi, T. S. Weber, R. Kiko, C. Deutsch, Global niche of marine anaerobic metabolisms expanded by particle microenvironments. *Nat. Geosci.* **11**, 263–268 (2018).

132. S. Motamedi, B. N. Orcutt, G. L. Früh-Green, K. I. Twing, H. L. Pendleton, W. J. Brazelton, Microbial Residents of the Atlantis Massif's Shallow Serpentinite Subsurface. *Appl. Environ. Microbiol.* **86** (2020).

133. K. A. Aquino, G. L. Früh-Green, Controls on mineral formation in high pH fluids from the Lost City hydrothermal field. *Geochem. Explor. Environ. Analy.* (2024).

134. K. A. Aquino, G. L. Früh-Green, Fluid mixing and spatial geochemical variability in the Lost City hydrothermal field chimneys. *Geochem. Explor. Environ. Analy.* (2024).

135. N. Rohland, D. Reich, Cost-effective, high-throughput DNA sequencing libraries for multiplexed target capture. *Genome Res.* **22**, 939–946 (2012).

136. B. Bushnell, J. Rood, E. Singer, BBMerge – Accurate paired shotgun read merging via overlap. *PLoS One* **12**, e0185056 (2017).

137. C. N. Thornton, W. D. Tanner, J. A. VanDerslice, W. J. Brazelton, Localized effect of treated wastewater effluent on the resistome of an urban watershed. *Gigascience* **9** (2020).

138. D. Li, R. Luo, C.-M. Liu, C.-M. Leung, H.-F. Ting, K. Sadakane, H. Yamashita, T.-W. Lam, MEGAHIT v1.0: A fast and scalable metagenome assembler driven by advanced methodologies and community practices. *Methods* **102**, 3–11 (2016).

139. D. Hyatt, G.-L. Chen, P. F. Locascio, M. L. Land, F. W. Larimer, L. J. Hauser, Prodigal: prokaryotic gene recognition and translation initiation site identification. *BMC Bioinformatics* **11**, 119 (2010).

140. B. Buchfink, K. Reuter, H.-G. Drost, Sensitive protein alignments at tree-of-life scale using DIAMOND. *Nat. Methods* **18**, 366–368 (2021).

141. B. Langmead, S. L. Salzberg, Fast gapped-read alignment with Bowtie 2. *Nat. Methods* **9**, 357–359 (2012).

142. E. D. Graham, J. F. Heidelberg, B. J. Tully, BinSanity: unsupervised clustering of environmental microbial assemblies using coverage and affinity propagation. *PeerJ* **5**, e3035 (2017).

143. P.-A. Chaumeil, A. J. Mussig, P. Hugenholtz, D. H. Parks, GTDB-Tk: a toolkit to classify genomes with the Genome Taxonomy Database. *Bioinformatics* **36**, 1925–1927 (2019).

144. D. H. Parks, M. Imelfort, C. T. Skennerton, P. Hugenholtz, G. W. Tyson, CheckM: assessing the quality of microbial genomes recovered from isolates, single cells, and metagenomes. *Genome Res.* **25**, 1043–1055 (2015).

145. A. R. Quinlan, I. M. Hall, BEDTools: a flexible suite of utilities for comparing genomic features. *Bioinformatics* **26**, 841–842 (2010).

146. P. J. McMurdie, S. Holmes, phyloseq: an R package for reproducible interactive analysis and graphics of microbiome census data. *PLoS One* **8**, e61217 (2013).

147. S. Q. Lang, M. D. Lilley, T. Baumberger, G. L. Früh-Green, S. L. Walker, W. J. Brazelton, D. S. Kelley, M. Elend, D. A. Butterfield, A. J. Mau, Extensive decentralized hydrogen export from the Atlantis Massif. *Geology* **49**, 851–856 (2021).

148. C. S. Sheik, B. K. Reese, K. I. Twing, J. B. Sylvan, S. L. Grim, M. O. Schrenk, M. L. Sogin, F. S. Colwell, Identification and Removal of Contaminant Sequences From Ribosomal Gene Databases: Lessons From the Census of Deep Life. *Front. Microbiol.* **9**, 840 (2018).

149. R Core Team, R: A Language and Environment for Statistical Computing. R Foundation for Statistical Computing [Preprint] (2022). https://www.R-project.org/.

150. L. Shenhav, M. Thompson, T. A. Joseph, L. Briscoe, O. Furman, D. Bogumil, I. Mizrahi, I. Pe'er, E. Halperin, FEAST: fast expectation-maximization for microbial source tracking. *Nat. Methods* **16**, 627–632 (2019).

151. D. Rizopoulos, ltm: An R Package for Latent Variable Modeling and Item Response Analysis. *J. Stat. Softw.* **17**, 1–25 (2007).

152. J. D. Storey, A Direct Approach to False Discovery Rates. *J. R. Stat. Soc. Series B Stat. Methodol.* **64**, 479–498 (2002).

153. J. D. Storey, R. Tibshirani, Statistical significance for genomewide studies. *Proc. Natl. Acad. Sci. U. S. A.* **100**, 9440–9445 (2003).

154. M. Kanehisa, S. Goto, KEGG: kyoto encyclopedia of genes and genomes. *Nucleic Acids Res.* **28**, 27–30 (2000).

155. K. A. Aquino, G. L. Früh-Green, J. Rickli, S. M. Bernasconi, S. Q. Lang, M. D. Lilley, D. A. Butterfield, Multi-stage evolution of the Lost City hydrothermal vent fluids. *Geochim. Cosmochim. Acta*, doi: 10.1016/j.gca.2022.06.027 (2022).

156. M. O. Schrenk, D. S. Kelley, S. A. Bolton, Low archaeal diversity linked to subseafloor geochemical processes at the Lost City Hydrothermal Field, Mid-Atlantic Ridge. *Environmentalist* (2004).

157. G. E. Hutchinson, The paradox of the plankton. *Am. Nat.* **95**, 137–145 (1961).

158. P. B. Price, T. Sowers, Temperature dependence of metabolic rates for microbial growth, maintenance, and survival. *Proc. Natl. Acad. Sci. U. S. A.* **101**, 4631–4636 (2004).

159. C. A. Fuchsman, R. E. Collins, G. Rocap, W. J. Brazelton, Effect of the environment on horizontal gene transfer between bacteria and archaea. *PeerJ* **5**, e3865 (2017).

160. D. R. Colman, S. Poudel, T. L. Hamilton, J. R. Havig, M. J. Selensky, E. L. Shock, E. S. Boyd, Geobiological feedbacks and the evolution of thermoacidophiles. *ISME J.* **12**, 225–236 (2018).

161. D. Verma, V. Kumar, T. Satyanarayana, Genomic attributes of thermophilic and hyperthermophilic bacteria and archaea. *World J. Microbiol. Biotechnol.* **38**, 135 (2022).

162. L. M. Guibert, C. L. Loviso, M. S. Marcos, M. G. Commendatore, H. M. Dionisi, M. Lozada, Alkane biodegradation genes from chronically polluted subantarctic coastal sediments and their shifts in response to oil exposure. *Microb. Ecol.* **64**, 605–616 (2012).

163. J. T. Hestetun, M. Fourt, J. Vacelet, N. Boury-Esnault, H. T. Rapp, Cladorhizidae (Porifera, Demospongiae, Poecilosclerida) of the deep Atlantic collected during Ifremer cruises, with a biogeographic overview of the Atlantic species. *J. Mar. Biol. Assoc. U. K.* **95**, 1311–1342 (2015).

164. J. T. P. Verhoeven, A. N. Kavanagh, S. C. Dufour, Microbiome analysis shows enrichment for specific bacteria in separate anatomical regions of the deep-sea carnivorous sponge Chondrocladia grandis. *FEMS Microbiol. Ecol.* **93** (2017).

165. H. P. Bacosa, D. L. Erdner, B. E. Rosenheim, P. Shetty, K. W. Seitz, B. J. Baker, Z. Liu, Hydrocarbon degradation and response of seafloor sediment bacterial community in the northern Gulf of Mexico to light Louisiana sweet crude oil. *ISME J.* **12**, 2532–2543 (2018).

166. R. Sousa, J. Vasconcelos, I. Vera-Escalona, J. Delgado, M. Freitas, J. A. González, R. Riera, Major ocean currents may shape the microbiome of the topshell Phorcus sauciatus in the NE Atlantic Ocean. *Sci. Rep.* **11**, 12480 (2021).

167. D. R. Nemergut, S. P. Anderson, C. C. Cleveland, A. P. Martin, A. E. Miller, A. Seimon, S. K. Schmidt, Microbial community succession in an unvegetated, recently deglaciated soil. *Microb. Ecol.* **53**, 110–122 (2007).

168. S. Tarlera, K. Jangid, A. H. Ivester, W. B. Whitman, M. A. Williams, Microbial community succession and bacterial diversity in soils during 77,000 years of ecosystem development. *FEMS Microbiol. Ecol.* **64**, 129–140 (2008).

169. W. Qin, K. R. Heal, R. Ramdasi, J. N. Kobelt, W. Martens-Habbena, A. D. Bertagnolli, S. A. Amin, C. B. Walker, H. Urakawa, M. Könneke, A. H. Devol, J. W. Moffett, E. V. Armbrust, G. J. Jensen, A. E. Ingalls, D. A. Stahl, Nitrosopumilus maritimus gen. nov., sp. nov., Nitrosopumilus cobalaminigenes sp. nov., Nitrosopumilus oxyclinae sp. nov., and Nitrosopumilus ureiphilus sp. nov., four marine ammonia-oxidizing archaea of the phylum Thaumarchaeota. *Int. J. Syst. Evol. Microbiol.* **67**, 5067–5079 (2017).

170. E. E. Rios-Del Toro, E. I. Valenzuela, J. E. Ramírez, N. E. López-Lozano, F. J. Cervantes, Anaerobic Ammonium Oxidation Linked to Microbial Reduction of Natural Organic Matter in Marine Sediments. *Environ. Sci. Technol. Lett.* **5**, 571–577 (2018).

171. H. Zhong, L. Lehtovirta-Morley, J. Liu, Y. Zheng, H. Lin, D. Song, J. D. Todd, J. Tian, X.-H. Zhang, Novel insights into the Thaumarchaeota in the deepest oceans: their metabolism and potential adaptation mechanisms. *Microbiome* **8**, 78 (2020).

172. M. C. Sabuda, W. J. Brazelton, L. I. Putman, T. M. McCollom, T. M. Hoehler, M. D. Y. Kubo, D. Cardace, M. O. Schrenk, A dynamic microbial sulfur cycle in a serpentinizing continental ophiolite. *Environ. Microbiol.*, doi: 10.1111/1462-2920.15006 (2020).

173. D. A. Gittins, P.-A. Desiage, N. Morrison, J. E. Rattray, S. Bhatnagar, A. Chakraborty, J. Zorz, C. Li, O. Horanszky, M. A. Cramm, F. Bisiach, R. Bennett, J. Webb, A. MacDonald, M. Fowler, D. C. Campbell, C. R. J. Hubert, Geological processes mediate a microbial dispersal loop in the deep biosphere. *Sci Adv* **8**, eabn3485 (2022).

174. S. Mino, H. Kudo, T. Arai, T. Sawabe, K. Takai, S. Nakagawa, Sulfurovum aggregans sp. nov., a hydrogen-oxidizing, thiosulfate-reducing chemolithoautotroph within the Epsilonproteobacteria isolated from a deep-sea hydrothermal vent chimney, and an

emended description of the genus Sulfurovum. *Int. J. Syst. Evol. Microbiol.* **64**, 3195–3201 (2014).

175. R. E. Anderson, J. Reveillaud, E. Reddington, T. O. Delmont, A. M. Eren, J. M. McDermott, J. S. Seewald, J. A. Huber, Genomic variation in microbial populations inhabiting the marine subseafloor at deep-sea hydrothermal vents. *Nat. Commun.* **8**, 1114 (2017).

176. K. Mori, K. Yamaguchi, S. Hanada, Sulfurovum denitrificans sp. nov., an obligately chemolithoautotrophic sulfur-oxidizing epsilonproteobacterium isolated from a hydrothermal field. *Int. J. Syst. Evol. Microbiol.* **68**, 2183–2187 (2018).

177. Q.-L. Sun, J. Zhang, M.-X. Wang, L. Cao, Z.-F. Du, Y.-Y. Sun, S.-Q. Liu, C.-L. Li, L. Sun, High-Throughput Sequencing Reveals a Potentially Novel Sulfurovum Species Dominating the Microbial Communities of the Seawater--Sediment Interface of a Deep-Sea Cold Seep in South China Sea. *Microorganisms* **8**, 687 (2020).

178. C. Dupraz, P. T. Visscher, L. K. Baumgartner, R. P. Reid, Microbe–mineral interactions: early carbonate precipitation in a hypersaline lake (Eleuthera Island, Bahamas). *Sedimentology* **51**, 745–765 (2004).

179. J. B. Ries, M. A. Anderson, R. T. Hill, Seawater Mg/Ca controls polymorph mineralogy of microbial CaCO3: a potential proxy for calcite-aragonite seas in Precambrian time. *Geobiology* **6**, 106–119 (2008).

180. C. Pisapia, E. Gérard, M. Gérard, L. Lecourt, S. Q. Lang, B. Pelletier, C. E. Payri, C. Monnin, L. Guentas, A. Postec, M. Quéméneur, G. Erauso, B. Ménez, Mineralizing Filamentous Bacteria from the Prony Bay Hydrothermal Field Give New Insights into the Functioning of Serpentinization-Based Subseafloor Ecosystems. *Front. Microbiol.* **8**, 57 (2017).

181. S. Krause, V. Liebetrau, C. R. Löscher, F. Böhm, S. Gorb, A. Eisenhauer, T. Treude, Marine ammonification and carbonic anhydrase activity induce rapid calcium carbonate precipitation. *Geochim. Cosmochim. Acta* **243**, 116–132 (2018).

182. S. Sundaram, I. S. Thakur, Induction of calcite precipitation through heightened production of extracellular carbonic anhydrase by CO2 sequestering bacteria. *Bioresour Technol* **253**, 368–371 (2018).

183. S. Wei, H. Cui, Z. Jiang, H. Liu, H. He, N. Fang, Biomineralization processes of calcite induced by bacteria isolated from marine sediments. *Braz. J. Microbiol.* **46**, 455–464 (2015).

184. W. J. Brazelton, J. A. Baross, Metagenomic comparison of two Thiomicrospira lineages inhabiting contrasting deep-sea hydrothermal environments. *PLoS One* **5**, e13530 (2010).

185. A. A. Larkin, A. C. Martiny, Microdiversity shapes the traits, niche space, and biogeography of microbial taxa. *Environ. Microbiol. Rep.* **9**, 55–70 (2017).

186. N. García-García, J. Tamames, A. M. Linz, C. Pedrós-Alió, F. Puente-Sánchez, Microdiversity ensures the maintenance of functional microbial communities under changing environmental conditions. *ISME J.* **13**, 2969–2983 (2019).

187. S. Fodelianakis, A. D. Washburne, M. Bourquin, P. Pramateftaki, T. J. Kohler, M. Styllas, M. Tolosano, V. De Staercke, M. Schön, S. B. Busi, J. Brandani, P. Wilmes, H. Peter, T. J. Battin, Microdiversity characterizes prevalent phylogenetic clades in the glacier-fed stream microbiome. *ISME J.* **16**, 666–675 (2022).

188. J. B. H. Martiny, A. C. Martiny, E. Brodie, A. B. Chase, A. Rodríguez-Verdugo, K. K. Treseder, S. D. Allison, Investigating the eco-evolutionary response of microbiomes to environmental change. *Ecol. Lett.* **26 Suppl 1**, S81–S90 (2023).

189. R. N. Mourgela, A. Kioukis, M. Pourjam, I. Lagkouvardos, Large-Scale Integration of Amplicon Data Reveals Massive Diversity within Saprospirales, Mostly Originating from Saline Environments. *Microorganisms* **11** (2023).

190. R. León-Zayas, L. Peoples, J. F. Biddle, S. Podell, M. Novotny, J. Cameron, R. S. Lasken, D. H. Bartlett, The metabolic potential of the single cell genomes obtained from the Challenger Deep, Mariana Trench within the candidate superphylum Parcubacteria (OD1). *Environ. Microbiol.* **19**, 2769–2784 (2017).

191. S. Suzuki, S. Ishii, T. Hoshino, A. Rietze, A. Tenney, P. L. Morrill, F. Inagaki, J. G. Kuenen, K. H. Nealson, Unusual metabolic diversity of hyperalkaliphilic microbial communities associated with subterranean serpentinization at The Cedars. *ISME J.* **11**, 2584 (2017).

192. S. O. Han, M. Inui, H. Yukawa, Expression of Corynebacterium glutamicum glycolytic genes varies with carbon source and growth phase. *Microbiology* **153**, 2190–2202 (2007).

193. W. J. Brazelton, J. A. Baross, Abundant transposases encoded by the metagenome of a hydrothermal chimney biofilm. *ISME J.* **3**, 1420–1424 (2009).

194. R. Gaupp, S. Schlag, M. Liebeke, M. Lalk, F. Götz, Advantage of upregulation of succinate dehydrogenase in Staphylococcus aureus biofilms. *J. Bacteriol.* **192**, 2385–2394 (2010).

195. M. Aoshima, M. Ishii, Y. Igarashi, A novel enzyme, citryl-CoA synthetase, catalysing the first step of the citrate cleavage reaction in Hydrogenobacter thermophilus TK-6. *Mol. Microbiol.* **52**, 751–761 (2004).

196. G. L. Chadwick, C. T. Skennerton, R. Laso-Pérez, A. O. Leu, D. R. Speth, H. Yu, C. Morgan-Lang, R. Hatzenpichler, D. Goudeau, R. Malmstrom, W. J. Brazelton, T. Woyke, S. J. Hallam, G. W. Tyson, G. Wegener, A. Boetius, V. J. Orphan, Comparative genomics reveals electron transfer and syntrophic mechanisms differentiating methanotrophic and methanogenic archaea. *PLoS Biol.* **20**, e3001508 (2022).

197. J. Bowman, The Methanotroph s—The Fam ilies Methylococcaceae and Methylocy staceae. *Prokaryote s* **5**, 266–289 (2006).

198. Z. Yang, W. Wang, Y. He, R. Zhang, G. Liu, Effect of ammonia on methane production, methanogenesis pathway, microbial community and reactor performance under mesophilic and thermophilic conditions. *Renewable Energy* **125**, 915–925 (2018).

199. M. Quadroni, W. Staudenmann, M. Kertesz, P. James, Analysis of global responses by protein and peptide fingerprinting of proteins isolated by two-dimensional gel electrophoresis. Application to the sulfate-starvation response of Escherichia coli. *Eur. J. Biochem.* **239**, 773–781 (1996).

200. L. M. Stancik, D. M. Stancik, B. Schmidt, D. M. Barnhart, Y. N. Yoncheva, J. L. Slonczewski, pH-dependent expression of periplasmic proteins and amino acid catabolism in Escherichia coli. *J. Bacteriol.* **184**, 4246–4258 (2002).

201. T. K. Sigdel, R. Cilliers, P. R. Gursahaney, P. Thompson, J. A. Easton, M. W. Crowder, Probing the adaptive response of Escherichia coli to extracellular Zn(II). *Biometals* **19**, 461–471 (2006).

202. L. L. Demina, A. Y. Lein, S. V. Galkin, A. P. Lisitzin, Features of trace metal distribution in the components of the ecosystem of the Lost City hydrothermal vent field (North Atlantic). *Dokl. Earth Sci.*, doi: 10.1134/S1028334X1512017X (2015).

203. C. Coimbra, P. Farias, R. Branco, P. V. Morais, Tungsten accumulation by highly tolerant marine hydrothermal Sulfitobacter dubius strains carrying a tupBCA cluster. *Syst. Appl. Microbiol.* **40**, 388–395 (2017).

204. N. Kitadai, R. Nakamura, M. Yamamoto, K. Takai, N. Yoshida, Y. Oono, Metals likely promoted protometabolism in early ocean alkaline hydrothermal systems. *Sci Adv* **5**, eaav7848 (2019).

205. A. W. Foster, T. R. Young, P. T. Chivers, N. J. Robinson, Protein metalation in biology. *Curr. Opin. Chem. Biol.* **66**, 102095 (2022).

206. A. C. Rosenzweig, Metallochaperones: bind and deliver. *Chem. Biol.* **9**, 673–677 (2002).

207. M. Vargas, K. Kashefi, E. L. Blunt-Harris, D. R. Lovley, Microbiological evidence for Fe(III) reduction on early Earth. *Nature* **395**, 65–67 (1998).

208. D. E. Canfield, M. T. Rosing, C. Bjerrum, Early anaerobic metabolisms. *Philos. Trans. R. Soc. Lond. B Biol. Sci.* **361**, 1819–34; discussion 1835-6 (2006).

209. P. G. Falkowski, T. Fenchel, E. F. Delong, The microbial engines that drive Earth's biogeochemical cycles. *Science* **320**, 1034–1039 (2008).

210. C. L. Dupont, A. Butcher, R. E. Valas, P. E. Bourne, G. Caetano-Anollés, History of biological metal utilization inferred through phylogenomic analysis of protein structures. *Proc. Natl. Acad. Sci. U. S. A.* **107**, 10567–10572 (2010).

211. F. M. M. Morel, N. M. Price, The biogeochemical cycles of trace metals in the oceans. *Science* **300**, 944–947 (2003).

212. L. J. Hoffmann, E. Breitbarth, P. W. Boyd, K. A. Hunter, Influence of ocean warming and acidification on trace metal biogeochemistry. *Mar. Ecol. Prog. Ser.* **470**, 191–205 (2012).

213. J. B. Glass, R. P. Axler, S. Chandra, C. R. Goldman, Molybdenum limitation of microbial nitrogen assimilation in aquatic ecosystems and pure cultures. *Front. Microbiol.* **3**, 331 (2012).

214. S. L. Begg, The role of metal ions in the virulence and viability of bacterial pathogens. *Biochem. Soc. Trans.* **47**, 77–87 (2019).

215. E. S. Honsa, M. D. L. Johnson, J. W. Rosch, The roles of transition metals in the physiology and pathogenesis of Streptococcus pneumoniae. *Front. Cell. Infect. Microbiol.* **3**, 92 (2013).

216. L. R. Brown, R. C. Caulkins, T. E. Schartel, J. W. Rosch, E. S. Honsa, S. Schultz-Cherry, V. A. Meliopoulos, S. Cherry, J. A. Thornton, Increased Zinc Availability Enhances Initial Aggregation and Biofilm Formation of Streptococcus pneumoniae. *Front. Cell. Infect. Microbiol.* **7**, 233 (2017).

217. M. M. Haque, M. K. Mosharaf, M. A. Haque, M. Z. H. Tanvir, M. K. Alam, Biofilm Formation, Production of Matrix Compounds and Biosorption of Copper, Nickel and Lead by Different Bacterial Strains. *Front. Microbiol.* **12**, 615113 (2021).

218. F. Tian, O. B. Toon, A. A. Pavlov, H. De Sterck, A hydrogen-rich early Earth atmosphere. *Science* **308**, 1014–1017 (2005).

219. J. F. Kasting, M. T. Howard, Atmospheric composition and climate on the early Earth. *Philos. Trans. R. Soc. Lond. B Biol. Sci.* **361**, 1733–41; discussion 1741-2 (2006).

220. G. Cooper, N. Kimmich, W. Belisle, J. Sarinana, K. Brabham, L. Garrel, Carbonaceous meteorites as a source of sugar-related organic compounds for the early Earth. *Nature* **414**, 879–883 (2001).

221. B. Fleury, N. Carrasco, M. Millan, L. Vettier, C. Szopa, Organic chemistry in a CO2 rich early Earth atmosphere. *Earth Planet. Sci. Lett.* **479**, 34–42 (2017).

222. E. G. Nisbet, N. H. Sleep, The habitat and nature of early life. *Nature* **409**, 1083–1091 (2001).

223. W. Martin, M. J. Russell, On the origins of cells: a hypothesis for the evolutionary transitions from abiotic geochemistry to chemoautotrophic prokaryotes, and from prokaryotes to nucleated cells. *Philos. Trans. R. Soc. Lond. B Biol. Sci.* **358**, 59–85 (2003).

224. D. Wacey, M. R. Kilburn, M. Saunders, J. Cliff, M. D. Brasier, Microfossils of sulphur-metabolizing cells in 3.4-billion-year-old rocks of Western Australia. *Nat. Geosci.* **4**, 698–702 (2011).

225. D. Papineau, Z. She, M. S. Dodd, F. Iacoviello, J. F. Slack, E. Hauri, P. Shearing, C. T. S. Little, Metabolically diverse primordial microbial communities in Earth's oldest seafloor-hydrothermal jasper. *Sci. Adv.* **8**, eabm2296 (2022).

226. J. C. Fontecilla-Camps, Nickel and the origin and early evolution of life. *Metallomics* **14**, mfac016 (2022).

227. A. Pernthaler, A. E. Dekas, C. T. Brown, S. K. Goffredi, T. Embaye, V. J. Orphan, Diverse syntrophic partnerships from deep-sea methane vents revealed by direct cell capture and metagenomics. *Proc. Natl. Acad. Sci. U. S. A.* **105**, 7052–7057 (2008).

228. M. J. McInerney, J. R. Sieber, R. P. Gunsalus, Syntrophy in anaerobic global carbon cycles. *Curr. Opin. Biotechnol.* **20**, 623–632 (2009).

229. D. A. Sverjensky, N. Lee, The Great Oxidation Event and Mineral Diversification. *Elements* **6**, 31–36 (2010).

230. C. H. Crosby, J. V. Bailey, M. Sharma, Fossil evidence of iron-oxidizing chemolithotrophy linked to phosphogenesis in the wake of the Great Oxidation Event. *Geology* **42**, 1015–1018 (2014).

231. L. J. Alcott, B. J. W. Mills, A. Bekker, S. W. Poulton, Earth's Great Oxidation Event facilitated by the rise of sedimentary phosphorus recycling. *Nat. Geosci.* **15**, 210–215 (2022).

232. C. Wandersman, P. Delepelaire, Bacterial iron sources: from siderophores to hemophores. *Annu Rev Microbiol* **58**, 611–647 (2004).

233. M. Hofmann, G. Retamal-Morales, D. Tischler, Metal binding ability of microbial natural metal chelators and potential applications. *Nat. Prod. Rep.* **37**, 1262–1283 (2020).

234. K. Vijayaraghavan, Y.-S. Yun, Bacterial biosorbents and biosorption. *Biotechnol Adv* **26**, 266–291 (2008).

235. P. H. Santschi, Marine colloids, agents of the self-cleansing capacity of aquatic systems: Historical perspective and new discoveries. *Marine Chemistry* **207**, 124–135 (2018).

236. G. M. Gadd, Metals, minerals and microbes: geomicrobiology and bioremediation. *Microbiology* **156**, 609–643 (2010).

237. S. Bellenberg, M. Díaz, N. Noël, W. Sand, A. Poetsch, N. Guiliani, M. Vera, Biofilm formation, communication and interactions of leaching bacteria during colonization of pyrite and sulfur surfaces. *Res Microbiol* **165**, 773–781 (2014).

238. C. S. Cockell, P. van Calsteren, J. F. W. Mosselmans, I. A. Franchi, I. Gilmour, L. Kelly, K. Olsson-Francis, D. Johnson, Microbial endolithic colonization and the geochemical environment in young seafloor basalts. *Chemical Geology* **279**, 17–30 (2010).

239. C. Gaylarde, B. Little, Biodeterioration of stone and metal - Fundamental microbial cycling processes with spatial and temporal scale differences. *Sci Total Environ* **823**, 153193 (2022).

240. E. S. Boyd, A. D. Anbar, S. Miller, T. L. Hamilton, M. Lavin, J. W. Peters, A late methanogen origin for molybdenum-dependent nitrogenase: A late methanogen origin for Mo-nitrogenase. *Geobiology* **9**, 221–232 (2011).

241. S. E. McGlynn, E. S. Boyd, J. W. Peters, V. J. Orphan, Classifying the metal dependence of uncharacterized nitrogenases. *Front. Microbiol.* **3**, 419 (2012).

242. J. B. Glass, F. Wolfe-Simon, A. D. Anbar, Coevolution of metal availability and nitrogen assimilation in cyanobacteria and algae. *Geobiology* **7**, 100–123 (2009).

243. L. L. Demina, S. V. Galkin, "Factors Controlling the Trace Metal Distribution in Hydrothermal Vent Organisms" in *Trace Metal Biogeochemistry and Ecology of Deep-Sea Hydrothermal Vent Systems*, L. L. Demina, S. V. Galkin, Eds. (Springer International Publishing, Cham, 2016), pp. 123–141.

244. L. D. Nothdurft, G. E. Webb, N. A. Buster, C. W. Holmes, J. E. Sorauf, J. T. Kloprogge, Brucite microbialites in living coral skeletons: Indicators of extreme microenvironments in shallow-marine settings. *Geology* **33**, 169–172 (2005).

245. A. L. M. Chun, A. Mosayyebi, A. Butt, D. Carugo, M. Salta, Early biofilm and streamer formation is mediated by wall shear stress and surface wettability: A multifactorial microfluidic study. *Microbiologyopen* **11**, e1310 (2022).

246. P. Stoodley, I. Dodds, J. D. Boyle, H. M. Lappin-Scott, Influence of hydrodynamics and nutrients on biofilm structure. *J. Appl. Microbiol.* **85 Suppl 1**, 19S-28S (1998).

247. Y. Politi, D. R. Batchelor, P. Zaslansky, B. F. Chmelka, J. C. Weaver, I. Sagi, S. Weiner, L. Addadi, Role of magnesium ion in the stabilization of biogenic amorphous calcium carbonate: A Structure−Function investigation. *Chem. Mater.* **22**, 161–166 (2010).

248. J. McCutcheon, I. M. Power, J. Shuster, A. L. Harrison, G. M. Dipple, G. Southam, Carbon Sequestration in Biogenic Magnesite and Other Magnesium Carbonate Minerals. *Environ. Sci. Technol.* **53**, 3225–3237 (2019).

249. B. Tesson, C. Gaillard, V. Martin-Jézéquel, Brucite formation mediated by the diatom Phaeodactylum tricornutum. *Mar. Chem.* **109**, 60–76 (2008).

250. X. Qiu, Y. Yao, H. Wang, Y. Duan, Live microbial cells adsorb Mg2+ more effectively than lifeless organic matter. *Front. Earth Sci.* **12**, 160–169 (2018).

251. M. E. Sanz-Montero, Ó. Cabestrero, M. Sánchez-Román, Microbial Mg-rich Carbonates in an Extreme Alkaline Lake (Las Eras, Central Spain). *Front. Microbiol.* **10**, 148 (2019).

252. A. S. Templeton, E. T. Ellison, Formation and loss of metastable brucite: does Fe(II)-bearing brucite support microbial activity in serpentinizing ecosystems? *Philos. Trans. A Math. Phys. Eng. Sci.* **378**, 20180423 (2020).

253. C. F. Estrada, D. A. Sverjensky, M. Pelletier, A. Razafitianamaharavo, R. M. Hazen, Interaction between l-aspartate and the brucite [Mg(OH)2]–water interface. *Geochim. Cosmochim. Acta* **155**, 172–186 (2015).

254. T. Fornaro, J. R. Brucato, C. Feuillie, D. A. Sverjensky, R. M. Hazen, R. Brunetto, M. D'Amore, V. Barone, Binding of Nucleic Acid Components to the Serpentinite-Hosted Hydrothermal Mineral Brucite. *Astrobiology* **18**, 989–1007 (2018).

255. J. Hövelmann, C. V. Putnis, L. G. Benning, Metal Sequestration through Coupled Dissolution–Precipitation at the Brucite–Water Interface. *Minerals* **8**, 346 (2018).

256. L. J. Liermann, A. S. Barnes, B. E. Kalinowski, X. Zhou, S. L. Brantley, Microenvironments of pH in biofilms grown on dissolving silicate surfaces. *Chemical Geology* **171**, 1–16 (2000).

257. P. J. Modreski, R. Aumente-Modreski, Fluorescent Minerals. *Rocks & Minerals* **71**, 14–22 (1996).

258. B. Tian, Y. Hua, Carotenoid biosynthesis in extremophilic Deinococcus-Thermus bacteria. *Trends Microbiol.* **18**, 512–520 (2010).

259. F. Mandelli, M. B. Couger, D. A. A. Paixão, C. B. Machado, C. M. Carnielli, J. A. Aricetti, I. Polikarpov, R. Prade, C. Caldana, A. F. Paes Leme, A. Z. Mercadante, D. M. Riaño-Pachón, F. M. Squina, Thermal adaptation strategies of the extremophile bacterium Thermus filiformis based on multi-omics analysis. *Extremophiles* **21**, 775–788 (2017).

260. R. Seto, S. Takaichi, T. Kurihara, R. Kishi, M. Honda, S. Takenaka, Y. Tsukatani, M. T. Madigan, Z.-Y. Wang-Otomo, Y. Kimura, Lycopene-Family Carotenoids Confer Thermostability on Photocomplexes from a New Thermophilic Purple Bacterium. *Biochemistry* **59**, 2351–2358 (2020).

261. E. Khalikova, S. Somersalo, T. Korpela, "Metabolites Produced by Alkaliphiles with Potential Biotechnological Applications" in *Alkaliphiles in Biotechnology*, G. Mamo, B. Mattiasson, Eds. (Springer International Publishing, Cham, 2020), pp. 157–193.

262. D. Smrzka, J. Zwicker, W. Bach, D. Feng, T. Himmler, D. Chen, J. Peckmann, The behavior of trace elements in seawater, sedimentary pore water, and their incorporation into carbonate minerals: a review. *Facies* **65**, 41 (2019).

263. T. H. Tran, K. Kato, H. Wada, K. Fujioka, H. Matsuzaki, Processes involved in calcite and aragonite precipitation during carbonate chimney formation on Conical Seamount, Mariana Forearc: Evidence from geochemistry and carbon, oxygen, and strontium isotopes. *Journal of Geochemical Exploration* **137**, 55–64 (2014).

264. J.-M. Brazier, V. Mavromatis (Βασίλειος Μαυρομάτης), Effect of growth rate on nickel and cobalt incorporation in aragonite. *Chem. Geol.* **600**, 120863 (2022).

265. E. K. Moore, J. Hao, A. Prabhu, H. Zhong, B. I. Jelen, M. Meyer, R. M. Hazen, P. G. Falkowski, Geological and chemical factors that impacted the biological utilization of cobalt in the Archean eon. *J. Geophys. Res. Biogeosci.* **123**, 743–759 (2018).

266. M. J. Russell, Cobalt: A must-have element for life and livelihood, *Proceedings of the National Academy of Sciences of the United States of America*. **119** (2022). https://doi.org/10.1073/pnas.2121307119.

267. R. A. Festa, D. J. Thiele, Copper: an essential metal in biology. *Curr. Biol.* **21**, R877-83 (2011).

268. A.-C. M. Toes, M. H. Daleke, J. G. Kuenen, G. Muyzer, Expression of copA and cusA in Shewanella during copper stress. *Microbiology* **154**, 2709–2718 (2008).

269. S. Chillappagari, M. Miethke, H. Trip, O. P. Kuipers, M. A. Marahiel, Copper acquisition is mediated by YcnJ and regulated by YcnK and CsoR in Bacillus subtilis. *J. Bacteriol.* **191**, 2362–2370 (2009).

270. N. Chin, J. Frey, C.-F. Chang, Y.-F. Chang, Identification of a locus involved in the utilization of iron byActinobacillus pleuropneumoniae. *FEMS Microbiol. Lett.* **143**, 1–6 (1996).

271. C. K. Y. Lau, H. Ishida, Z. Liu, H. J. Vogel, Solution structure of Escherichia coli FeoA and its potential role in bacterial ferrous iron transport. *J. Bacteriol.* **195**, 46–55 (2013).

272. D. R. Lovley, Microbial Fe(III) reduction in subsurface environments. *FEMS Microbiol. Rev.* **20**, 305–313 (1997).

273. J. M. Byrne, N. Klueglein, C. Pearce, K. M. Rosso, E. Appel, A. Kappler, Redox cycling of Fe(II) and Fe(III) in magnetite by Fe-metabolizing bacteria. *Science* **347**, 1473–1476 (2015).

274. X.-N. Wang, G.-X. Sun, X.-M. Li, T. A. Clarke, Y.-G. Zhu, Electron shuttle-mediated microbial Fe(III) reduction under alkaline conditions. *J. Soils Sediments* **18**, 159–168 (2018).

275. S. D. Midgley, J. O. Taylor, D. Fleitmann, R. Grau-Crespo, Molybdenum and sulfur incorporation as oxyanion substitutional impurities in calcium carbonate minerals: A computational investigation. *Chem. Geol.* **553**, 119796 (2020).

276. J. A. Hernandez, S. J. George, L. M. Rubio, Molybdenum trafficking for nitrogen fixation. *Biochemistry* **48**, 9711–9721 (2009).

277. S. Burén, E. Jiménez-Vicente, C. Echavarri-Erasun, L. M. Rubio, Biosynthesis of nitrogenase cofactors. *Chem. Rev.* **120**, 4921–4968 (2020).

278. L. Demtröder, F. Narberhaus, B. Masepohl, Coordinated regulation of nitrogen fixation and molybdate transport by molybdenum: Molybdenum regulation of nitrogen fixation. *Mol. Microbiol.* **111**, 17–30 (2019).

279. Y. Dilek, H. Furnes, Ophiolites and Their Origins. *Elements* **10**, 93–100 (2014).

280. C. Oze, C. Skinner, A. W. Schroth, R. G. Coleman, Growing up green on serpentine soils: Biogeochemistry of serpentine vegetation in the Central Coast Range of California. *Appl. Geochem.* **23**, 3391–3403 (2008).

281. J. Kierczak, A. Pietranik, A. Pędziwiatr, Ultramafic geoecosystems as a natural source of Ni, Cr, and Co to the environment: A review. *Sci Total Environ* **755**, 142620 (2021).

282. J.-L. Vigneresse, C. Ballouard, X. Liu, A. Richard, Toward a global conceptual model for metal enrichment in felsic, mafic-ultramafic, and alkaline-carbonatitic magmas. *Ore Geology Reviews* **129**, 103925 (2021).

283. K. U. Brady, A. R. Kruckeberg, H. D. Bradshaw Jr, Evolutionary Ecology of Plant Adaptation to Serpentine Soils. *Annual Review of Ecology, Evolution, and Systematics* **36**, 243–266 (2005).

284. A. Mengoni, R. Barzanti, C. Gonnelli, R. Gabbrielli, M. Bazzicalupo, Characterization of nickel-resistant bacteria isolated from serpentine soil. *Environ. Microbiol.* **3**, 691–698 (2001).

285. A. Pal, G. Wauters, A. K. Paul, Nickel tolerance and accumulation by bacteria from rhizosphere of nickel hyperaccumulators in serpentine soil ecosystem of Andaman, India. *Plant Soil* **293**, 37–48 (2007).

286. W. Aboudrar, C. Schwartz, J. L. Morel, A. Boularbah, Effect of nickel-resistant rhizosphere bacteria on the uptake of nickel by the hyperaccumulator Noccaea caerulescens under controlled conditions. *J. Soils Sediments* **13**, 501–507 (2013).

287. S. Lopez, X. Goux, G. Echevarria, M. Calusinska, J. L. Morel, E. Benizri, Community diversity and potential functions of rhizosphere-associated bacteria of nickel hyperaccumulators found in Albania. *Sci Total Environ* **654**, 237–249 (2019).

288. S. Suzuki, S. Ishii, A. Wu, A. Cheung, A. Tenney, G. Wanger, J. G. Kuenen, K. H. Nealson, Microbial diversity in The Cedars, an ultrabasic, ultrareducing, and low salinity serpentinizing ecosystem. *Proc. Natl. Acad. Sci. U. S. A.* **110**, 15336–15341 (2013).

289. H. M. Miller, J. M. Matter, P. Kelemen, E. T. Ellison, M. E. Conrad, N. Fierer, T. Ruchala, M. Tominaga, A. S. Templeton, Modern water/rock reactions in Oman hyperalkaline peridotite aquifers and implications for microbial habitability. *Geochim. Cosmochim. Acta* **179**, 217–241 (2016).

290. K. I. Twing, W. J. Brazelton, M. D. Y. Kubo, A. J. Hyer, D. Cardace, T. M. Hoehler, T. M. McCollom, M. O. Schrenk, Serpentinization-Influenced Groundwater Harbors Extremely Low Diversity Microbial Communities Adapted to High pH. *Front. Microbiol.* **8**, 308 (2017).

291. K. Gravuer, A. Eskelinen, J. B. Winbourne, S. P. Harrison, Vulnerability and resistance in the spatial heterogeneity of soil microbial communities under resource additions. *Proc. Natl. Acad. Sci. U. S. A.* **117**, 7263–7270 (2020).

292. D. O. Burge, C. F. Salk, Climatic niche shifts in the serpentine soil flora of California. *J. Veg. Sci.* **25**, 873–884 (2014).

293. K. Suda, Y. Ueno, M. Yoshizaki, H. Nakamura, K. Kurokawa, E. Nishiyama, K. Yoshino, Y. Hongoh, K. Kawachi, S. Omori, K. Yamada, N. Yoshida, S. Maruyama, Origin of methane in serpentinite-hosted hydrothermal systems: The CH4–H2–H2O hydrogen isotope systematics of the Hakuba Happo hot spring. *Earth and Planetary Science Letters* **386**, 112–125 (2014).

294. M. O. Schrenk, "5. Life in serpentinite hosted alkaline springs" in *Life at Vents and Seeps*, J. Kallmeyer, Ed. (De Gruyter, Berlin, Boston, 2017), pp. 107–138.

295. E. Kazakou, P. G. Dimitrakopoulos, A. J. M. Baker, R. D. Reeves, A. Y. Troumbis, Hypotheses, mechanisms and trade-offs of tolerance and adaptation to serpentine soils: from species to ecosystem level. *Biol. Rev. Camb. Philos. Soc.* **83**, 495–508 (2008).

296. A. Gordon, C. B. Lipman, WHY ARE SERPENTINE AND OTHER MAGNESIAN SOILS INFERTILE? *Soil Science* **22**, 291 (1926).

297. E. O. Jordan, I. S. Falk, *The Newer Knowledge of Bacteriology and Immunology, by Eighty-Two Contributors; Edited by Edwin O. Jordan and I.S. Falk* (The University of Chicago Press, Chicago, 1928).

298. M. Héry, L. Philippot, E. Mériaux, F. Poly, X. Le Roux, E. Navarro, Nickel mine spoils revegetation attempts: effect of pioneer plants on two functional bacterial communities involved in the N-cycle. *Environ. Microbiol.* **7**, 486–498 (2005).

299. K. Battenberg, J. A. Wren, J. Hillman, J. Edwards, L. Huang, A. M. Berry, The influence of the host plant is the major ecological determinant of the presence of nitrogen-fixing root nodule symbiont cluster II Frankia species in soil. *Appl. Environ. Microbiol.* **83** (2017).

300. H. L. Banciu, D. Y. Sorokin, "Adaptation in Haloalkaliphiles and Natronophilic Bacteria" in *Cellular Origin, Life in Extreme Habitats and Astrobiology* (Springer Netherlands, Dordrecht, 2013), pp. 121–178.

301. A. Serra-Cardona, D. Canadell, J. Ariño, Coordinate responses to alkaline pH stress in budding yeast. *Microb. Cell* **2**, 182–196 (2015).

302. B. A. Hungate, E. A. Holland, R. B. Jackson, F. S. Chapin III, H. A. Mooney, C. B. Field, The fate of carbon in grasslands under carbon dioxide enrichment. *Nature* **388**, 576–579 (1997).

303. K. Gravuer, A. Eskelinen, Nutrient and rainfall additions shift phylogenetically estimated traits of soil microbial communities. *Front. Microbiol.* **8**, 1271 (2017).

304. E. Bonifacio, G. Falsone, M. Catoni, Influence of serpentine abundance on the vertical distribution of available elements in soils. *Plant Soil* **368**, 493–506 (2013).

305. S. Guillot, K. Hattori, Serpentinites Special Issue. *Elements (Que.)* **9** (2013).

306. S. M. Jowitt, B. A. McNulty, Battery and Energy Metals: Future Drivers of the Minerals Industry? *SEG Discovery*, 11–18 (2021).

307. M. Louvel, B. Etschmann, Q. Guan, D. Testemale, J. Brugger, Carbonate complexation enhances hydrothermal transport of rare earth elements in alkaline fluids. *Nat. Commun.* **13**, 1456 (2022).

308. D.-R. Qi, T.-G. Lan, Q. Shu, Y. Feng, S.-H. Zhou, Nickel enrichment during lateritization of ophiolitic ultramafic rocks: A case study from the Kelurahan Pondidrha laterite profile in Sulawesi, Indonesia. *Ore Geol. Rev.* **170**, 106140 (2024).

309. C. R. M. Butt, D. Cluzel, Nickel Laterite Ore Deposits: Weathered Serpentinites. *Elements* **9**, 123–128 (2013).

310. P. K. Das, B. P. Das, P. Dash, Chromite mining pollution, environmental impact, toxicity and phytoremediation: a review. *Environ. Chem. Lett.* **19**, 1369–1381 (2021).

311. P. Bilong, P.-D. Ndjigui, R. Temdjim, E. Sababa, Geochemistry of peridotite and granite xenoliths during the early stage of weathering in the Nyos volcanic region (NW Cameroon): Implications for PGE exploration. *Geochemistry* **71**, 77–86 (2011).

312. S. Ishtiyaq, H. Kumar, M. Varun, B. Kumar, M. S. Paul, "Heavy metal toxicity and antioxidative response in plants: An overview" in *Plants Under Metal and Metalloid Stress* (Springer Singapore, Singapore, 2018), pp. 77–106.

313. M. Lago-Vila, D. Arenas-Lago, A. Rodríguez-Seijo, M. L. Andrade Couce, F. A. Vega, Cobalt, chromium and nickel contents in soils and plants from a serpentinite quarry. *Solid Earth* **6**, 323–335 (2015).

314. C. Oze, S. Fendorf, D. K. Bird, R. G. Coleman, Chromium geochemistry in serpentinized ultramafic rocks and serpentine soils from the Franciscan complex of California. *Am. J. Sci.* **304**, 67–101 (2004).

315. K. H. Gayer, A. B. Garrett, The solubility of cobalt hydroxide, co$(OH)_2$, in solutions of hydrochloric acid and sodium hydroxide at 25°. *J. Am. Chem. Soc.* **72**, 3921–3923 (1950).

316. S. S. Porter, P. L. Chang, C. A. Conow, J. P. Dunham, M. L. Friesen, Association mapping reveals novel serpentine adaptation gene clusters in a population of symbiotic Mesorhizobium. *ISME J.* **11**, 248–262 (2017).

317. S. Isnard, L. L'Huillier, A. L. D. Paul, J. Munzinger, B. Fogliani, G. Echevarria, P. D. Erskine, V. Gei, T. Jaffré, A. van der Ent, Novel insights into the hyperaccumulation syndrome in Pycnandra (Sapotaceae). *Front. Plant Sci.* **11**, 559059 (2020).

318. G. Haferburg, E. Kothe, Microbes and metals: interactions in the environment: Microbes and metals: interactions in the environment. *J. Basic Microbiol.* **47**, 453–467 (2007).

319. D. Cardace, T. Hoehler, T. McCollom, M. Schrenk, D. Carnevale, M. Kubo, K. Twing, Establishment of the Coast Range ophiolite microbial observatory (CROMO): drilling objectives and preliminary outcomes. *Sci. Drill.* **16**, 45–55 (2013).

320. M. C. Sabuda, L. I. Putman, T. M. Hoehler, M. D. Kubo, W. J. Brazelton, D. Cardace, M. O. Schrenk, Biogeochemical gradients in a serpentinization-influenced aquifer: Implications for gas exchange between the subsurface and atmosphere. *J. Geophys. Res. Biogeosci.* **126** (2021).

321. E. Ortiz, M. Tominaga, D. Cardace, M. O. Schrenk, T. M. Hoehler, M. D. Kubo, D. F. Rucker, Geophysical characterization of serpentinite hosted hydrogeology at the McLaughlin natural reserve, coast range ophiolite. *Geochem. Geophys. Geosyst.* **19**, 114–131 (2018).

322. S. M. Huse, D. B. Mark Welch, A. Voorhis, A. Shipunova, H. G. Morrison, A. M. Eren, M. L. Sogin, VAMPS: a website for visualization and analysis of microbial population structures. *BMC Bioinformatics* **15** (2014).

323. P. D. Schloss, S. L. Westcott, T. Ryabin, J. R. Hall, M. Hartmann, E. B. Hollister, R. A. Lesniewski, B. B. Oakley, D. H. Parks, C. J. Robinson, J. W. Sahl, B. Stres, G. G. Thallinger, D. J. Van Horn, C. F. Weber, Introducing mothur: open-source, platform-independent, community-supported software for describing and comparing microbial communities. *Appl. Environ. Microbiol.* **75**, 7537–7541 (2009).

324. S. Boisvert, F. Raymond, E. Godzaridis, F. Laviolette, J. Corbeil, Ray Meta: scalable de novo metagenome assembly and profiling. *Genome Biol.* **13**, R122 (2012).

325. I. Gregor, J. Dröge, M. Schirmer, C. Quince, A. C. McHardy, PhyloPythiaS+: a self-training method for the rapid reconstruction of low-ranking taxonomic bins from metagenomes. *PeerJ* **4**, e1603 (2016).

326. T. Seemann, Prokka: rapid prokaryotic genome annotation. *Bioinformatics* **30**, 2068–2069 (2014).

327. S. Anders, P. T. Pyl, W. Huber, HTSeq--a Python framework to work with high-throughput sequencing data. *Bioinformatics* **31**, 166–169 (2015).

328. S. Kumar, S. Ghosh, S. Mukherjee, S. Sarkar, Chromium and nickel migration study through fine grained soil. *J. Hazard. Mater.* **170**, 1192–1196 (2009).

329. J. M. Morrison, M. B. Goldhaber, L. Lee, J. M. Holloway, R. B. Wanty, R. E. Wolf, J. F. Ranville, A regional-scale study of chromium and nickel in soils of northern California, USA. *Appl. Geochem.* **24**, 1500–1511 (2009).

330. M. Ito, M. Morino, T. A. Krulwich, Mrp antiporters have important roles in diverse bacteria and Archaea. *Front. Microbiol.* **8**, 2325 (2017).

331. J. M. Morrison, M. B. Goldhaber, C. T. Mills, G. N. Breit, R. L. Hooper, J. M. Holloway, S. F. Diehl, J. F. Ranville, Weathering and transport of chromium and nickel from serpentinite in the Coast Range ophiolite to the Sacramento Valley, California, USA. *Appl. Geochem.* **61**, 72–86 (2015).

332. S. Corvec, Clinical and Biological Features of Cutibacterium (Formerly Propionibacterium) avidum, an Underrecognized Microorganism. *Clin. Microbiol. Rev.* **31** (2018).

333. E. Pérez-Valera, M. Kyselková, E. Ahmed, F. X. J. Sladecek, M. Goberna, D. Elhottová, Native soil microorganisms hinder the soil enrichment with antibiotic resistance genes following manure applications. *Sci. Rep.* **9**, 6760 (2019).

334. M. Paniagua-López, M. Vela-Cano, D. Correa-Galeote, F. Martín-Peinado, F. J. M. Garzón, C. Pozo, J. González-López, M. S. Aragón, Soil remediation approach and bacterial community structure in a long-term contaminated soil by a mining spill (Aznalcóllar, Spain). *Science of The Total Environment* **777**, 145128 (2021).

335. H.-Z. Li, K. Yang, H. Liao, S. B. Lassen, J.-Q. Su, X. Zhang, L. Cui, Y.-G. Zhu, Active antibiotic resistome in soils unraveled by single-cell isotope probing and targeted metagenomics. *Proc. Natl. Acad. Sci. U. S. A.* **119**, e2201473119 (2022).

336. N. Lenchi, W. N. E. H. Ahmedi, M. Llirós, Simultaneous removal of crude oil and heavy metals by highly adapted bacterial strain Cutibacterium sp. NL2 isolated from Algerian oilfield. *Int. Microbiol.* **27**, 615–630 (2024).

337. S. Congeevaram, S. Dhanarani, J. Park, M. Dexilin, K. Thamaraiselvi, Biosorption of chromium and nickel by heavy metal resistant fungal and bacterial isolates. *J. Hazard. Mater.* **146**, 270–277 (2007).

338. S. Sher, S. Z. Hussain, A. Rehman, Phenotypic and genomic analysis of multiple heavy metal-resistant Micrococcus luteus strain AS2 isolated from industrial waste water and its potential use in arsenic bioremediation. *Appl. Microbiol. Biotechnol.* **104**, 2243–2254 (2020).

339. I. Arroyo-Herrera, B. Román-Ponce, R. Bustamante-Brito, J. Guevara-Luna, E. Y. Tapia-García, V. Larios-Serrato, N. Zhang, P. Estrada-de Los Santos, E. T. Wang, M. S. Vásquez-Murrieta, Arsenic and chromium resistance mechanisms in the Micrococcus luteus group. *Pedosphere* **33**, 600–611 (2023).

340. C. Chen, Q. Zheng, Y.-N. Wang, X.-J. Yan, L.-K. Hao, X. Du, N. Jiao, Stakelama pacifica gen. nov., sp. nov., a new member of the family Sphingomonadaceae isolated from the Pacific Ocean. *Int. J. Syst. Evol. Microbiol.* **60**, 2857–2861 (2010).

341. Q. Li, P. You, Q. Hu, B. Leng, J. Wang, J. Chen, S. Wan, B. Wang, C. Yuan, R. Zhou, K. Ouyang, Effects of co-contamination of heavy metals and total petroleum hydrocarbons on soil bacterial community and function network reconstitution. *Ecotoxicol Environ Saf* **204**, 111083 (2020).

342. W.-J. Gong, Z.-F. Niu, X.-R. Wang, H.-P. Zhao, How the Soil Microbial Communities and Activities Respond to Long-Term Heavy Metal Contamination in Electroplating Contaminated Site. *Microorganisms* **9** (2021).

343. S. Oh, D. Choi, Microbial Community Enhances Biodegradation of Bisphenol A Through Selection of Sphingomonadaceae. *Microb. Ecol.* **77**, 631–639 (2019).

344. A. Legatzki, G. Grass, A. Anton, C. Rensing, D. H. Nies, Interplay of the Czc system and two P-type ATPases in conferring metal resistance to Ralstonia metallidurans. *J. Bacteriol.* **185**, 4354–4361 (2003).

345. A. Stahl, D. Pletzer, A. Mehmood, M. S. Ullrich, Marinobacter adhaerens HP15 harbors two CzcCBA efflux pumps involved in zinc detoxification. *Antonie Van Leeuwenhoek* **108**, 649–658 (2015).

346. S. F. Alquethamy, F. G. Adams, R. Maharjan, N. N. Delgado, M. Zang, K. Ganio, J. C. Paton, K. A. Hassan, I. T. Paulsen, C. A. McDevitt, A. K. Cain, B. A. Eijkelkamp, The Molecular Basis of Acinetobacter baumannii Cadmium Toxicity and Resistance. *Appl. Environ. Microbiol.* **87**, e0171821 (2021).

347. G. Grass, B. Fan, B. P. Rosen, K. Lemke, H. G. Schlegel, C. Rensing, NreB from Achromobacter xylosoxidans 31A Is a nickel-induced transporter conferring nickel resistance. *J. Bacteriol.* **183**, 2803–2807 (2001).

348. A. Rodrigue, G. Effantin, M.-A. Mandrand-Berthelot, Identification of rcnA (yohM), a nickel and cobalt resistance gene in Escherichia coli. *J. Bacteriol.* **187**, 2912–2916 (2005).

349. J. L. Rowe, G. L. Starnes, P. T. Chivers, Complex transcriptional control links NikABCDE-dependent nickel transport with hydrogenase expression in Escherichia coli. *J. Bacteriol.* **187**, 6317–6323 (2005).

350. A. Margaryan, H. Panosyan, N. Birkeland, A. Trchounian, Heavy metal accumulation and the expression of the copA and nikA genes in Bacillus subtilis AG4 isolated fromthe Sotk Gold Mine in Armenia. *Biolog J Armenia* **3**, 51–57 (2013).

351. B. Sharma, P. Shukla, A comparative analysis of heavy metal bioaccumulation and functional gene annotation towards multiple metal resistant potential by Ochrobactrum intermedium BPS-20 and Ochrobactrum ciceri BPS-26. *Bioresour Technol* **320**, 124330 (2021).

352. T. Eitinger, J. Suhr, L. Moore, J. A. C. Smith, Secondary transporters for nickel and cobalt ions: theme and variations. *Biometals* **18**, 399–405 (2005).

353. E. Raux, A. Lanois, F. Levillayer, M. J. Warren, E. Brody, A. Rambach, C. Thermes, Salmonella typhimurium cobalamin (vitamin B12) biosynthetic genes: functional studies in S. typhimurium and Escherichia coli. *J. Bacteriol.* **178**, 753–767 (1996).

354. E. Raux, C. Thermes, P. Heathcote, A. Rambach, M. J. Warren, A role for Salmonella typhimurium cbiK in cobalamin (vitamin B12) and siroheme biosynthesis. *J. Bacteriol.* **179**, 3202–3212 (1997).

355. S. A. L. Lobo, A. A. Brindley, C. V. Romão, H. K. Leech, M. J. Warren, L. M. Saraiva, Two distinct roles for two functional cobaltochelatases (CbiK) in Desulfovibrio vulgaris hildenborough. *Biochemistry* **47**, 5851–5857 (2008).

356. S. Siche, O. Neubauer, P. Hebbeln, T. Eitinger, A bipartite S unit of an ECF-type cobalt transporter. *Res. Microbiol.* **161**, 824–829 (2010).

357. P. Chandrangsu, C. Rensing, J. D. Helmann, Metal homeostasis and resistance in bacteria. *Nat. Rev. Microbiol.* **15**, 338–350 (2017).

358. M. Bala Krishna Prasad, A. L. Ramanathan, S. K. Shrivastav, Anshumali, R. Saxena, Metal fractionation studies in surfacial and core sediments in the Achankovil River Basin in India. *Environ. Monit. Assess.* **121**, 77–102 (2006).

359. C. Oze, D. K. Bird, S. Fendorf, Genesis of hexavalent chromium from natural sources in soil and groundwater. *Proc. Natl. Acad. Sci. U. S. A.* **104**, 6544–6549 (2007).

360. A. U. Rajapaksha, M. Vithanage, C. Oze, W. M. A. T. Bandara, R. Weerasooriya, Nickel and manganese release in serpentine soil from the Ussangoda Ultramafic Complex, Sri Lanka. *Geoderma* **189–190**, 1–9 (2012).

361. S. Begum, M. T. Shah, S. Muhammad, S. Khan, Role of mafic and ultramafic rocks in drinking water quality and its potential health risk assessment, Northern Pakistan. *J. Water Health* **13**, 1130–1142 (2015).

362. A. El-Naggar, N. Ahmed, A. Mosa, N. K. Niazi, B. Yousaf, A. Sharma, B. Sarkar, Y. Cai, S. X. Chang, Nickel in soil and water: Sources, biogeochemistry, and remediation using biochar. *J. Hazard. Mater.* **419**, 126421 (2021).

363. K. B. Muchowska, S. J. Varma, E. Chevallot-Beroux, L. Lethuillier-Karl, G. Li, J. Moran, Metals promote sequences of the reverse Krebs cycle. *Nat. Ecol. Evol.* **1**, 1716–1721 (2017).

364. A. Aithal, S. Dagar, S. Rajamani, Metals in prebiotic catalysis: A possible evolutionary pathway for the emergence of metalloproteins. *ACS Omega* **8**, 5197–5208 (2023).

APPENDIX

Table A.1 - Here, the individual correlated ASVs are tabulated with their correlation score, p-value and q-value, as well as their taxonomic assignment. Each ASV was assigned a correlated mineral ARA for aragonite, BRU for brucite or CAL for calcite.

Amplicon	Correlated Mineral	Correlation Score	p-value	q-value	Domain	Phylum	Class	Order	Family	Genus
ASV 28789	ARA	0.75	3.61E-04	3.20E-03	Bacteria	Acidobacteria	Thermoanaerobaculia	Thermoanaerobaculales	Thermoanaerobaculaceae	Subgroup_10
ASV 13595	ARA	0.61	6.70E-03	4.77E-02	Bacteria	Actinobacteria	Acidimicrobiia	Microtrichales	Microtrichaceae	Sva0996_marine_group
ASV 5261	ARA	0.65	3.77E-03	2.82E-02	Bacteria	Bacteroidetes	Bacteroidia	Chitinophagales	Saprospiraceae	NA
ASV 108	ARA	-0.64	3.85E-03	2.88E-02	Bacteria	Chloroflexi	Dehalococcoidia	MSBL5	NA	NA
ASV 1415	ARA	0.61	6.90E-03	4.90E-02	Bacteria	Proteobacteria	Alphaproteobacteria	Caulobacterales	Hyphomonadaceae	Robiginitomaculum
ASV 25891	ARA	0.63	4.67E-03	3.43E-02	Bacteria	Proteobacteria	Deltaproteobacteria	NA	NA	NA
ASV 17903	ARA	-0.67	2.46E-03	1.90E-02	Bacteria	Proteobacteria	Gammaproteobacteria	Betaproteobacteriales	Burkholderiaceae	Burkholderia-Caballeronia-Paraburkholderia
ASV 21391	ARA	0.63	4.93E-03	3.60E-02	Bacteria	Proteobacteria	Gammaproteobacteria	NA	NA	NA
ASV 28789	BRU	-0.70	1.15E-03	9.40E-03	Bacteria	Acidobacteria	Thermoanaerobaculia	Thermoanaerobaculales	Thermoanaerobaculaceae	Subgroup_10
ASV 13595	BRU	-0.63	4.82E-03	3.53E-02	Bacteria	Actinobacteria	Acidimicrobiia	Microtrichales	Microtrichaceae	Sva0996_marine_group
ASV 15855	BRU	0.66	2.77E-03	2.12E-02	Bacteria	Bacteroidetes	Bacteroidia	Chitinophagales	Saprospiraceae	Lewinella
ASV 108	BRU	0.66	3.08E-03	2.34E-02	Bacteria	Chloroflexi	Dehalococcoidia	MSBL5	NA	NA
ASV 32052	BRU	0.62	6.49E-03	4.64E-02	Bacteria	NA	NA	NA	NA	NA
ASV 22681	BRU	0.61	6.67E-03	4.75E-02	Bacteria	Patescibacteria	Parcubacteria	NA	NA	NA
ASV 32666	BRU	-0.62	6.06E-03	4.36E-02	Bacteria	Proteobacteria	Alphaproteobacteria	Parvibaculales	PS1_clade	NA
ASV 25891	BRU	-0.62	5.85E-03	4.22E-02	Bacteria	Proteobacteria	Deltaproteobacteria	NA	NA	NA
ASV 21391	BRU	-0.62	6.09E-03	4.38E-02	Bacteria	Proteobacteria	Gammaproteobacteria	NA	NA	NA
ASV 24292	BRU	-0.63	5.09E-03	3.71E-02	Bacteria	Proteobacteria	Gammaproteobacteria	NA	NA	NA
ASV 19933	CAL	0.66	2.71E-03	2.08E-02	Archaea	Euryarchaeota	Methanomicrobia	ANME-1	ANME-1b	NA
ASV 29510	CAL	0.64	4.09E-03	3.04E-02	Archaea	Euryarchaeota	Methanomicrobia	ANME-1	ANME-1b	NA
ASV 10892	CAL	0.64	4.56E-03	3.35E-02	Archaea	Euryarchaeota	Methanomicrobia	ANME-1	ANME-1b	NA
ASV 13742	CAL	0.65	3.76E-03	2.81E-02	Archaea	Thaumarchaeota	Nitrososphaeria	Nitrosopumilales	Nitrosopumilaceae	Candidatus_Nitrosopumilus
ASV 797	CAL	0.66	2.64E-03	2.03E-02	Bacteria	Acetothermia	Acetothermiia	NA	NA	NA
ASV 21271	CAL	0.62	5.68E-03	4.11E-02	Bacteria	Acidobacteria	Thermoanaerobaculia	Thermoanaerobaculales	Thermoanaerobaculaceae	Subgroup_10
ASV 15578	CAL	0.62	6.49E-03	4.64E-02	Bacteria	Actinobacteria	Acidimicrobiia	Microtrichales	Microtrichaceae	Sva0996_marine_group
ASV 18469	CAL	0.64	4.36E-03	3.22E-02	Bacteria	Actinobacteria	WCHB1-81	NA	NA	NA
ASV 3001	CAL	0.69	1.57E-03	1.25E-02	Bacteria	Aegiribacteria	NA	NA	NA	NA
ASV 8726	CAL	0.65	3.70E-03	2.77E-02	Bacteria	Bacteroidetes	Bacteroidia	Cytophagales	Cyclobacteriaceae	NA
ASV 513	CAL	0.61	6.68E-03	4.76E-02	Bacteria	Bacteroidetes	Bacteroidia	Sphingobacteriales	Lentimicrobiaceae	NA
ASV 3440	CAL	0.76	2.78E-04	2.51E-03	Bacteria	BHI80-139	NA	NA	NA	NA
ASV 30518	CAL	0.75	3.12E-04	2.80E-03	Bacteria	BHI80-139	NA	NA	NA	NA
ASV 539	CAL	0.72	7.97E-04	6.67E-03	Bacteria	BHI80-139	NA	NA	NA	NA
ASV 10478	CAL	0.68	1.88E-03	1.48E-02	Bacteria	BHI80-139	NA	NA	NA	NA
ASV 20452	CAL	0.66	3.08E-03	2.35E-02	Bacteria	BHI80-139	NA	NA	NA	NA
ASV 5750	CAL	0.65	3.73E-03	2.79E-02	Bacteria	BHI80-139	NA	NA	NA	NA
ASV 33679	CAL	0.74	5.06E-04	4.38E-03	Bacteria	Chloroflexi	Dehalococcoidia	DscP2	NA	NA
ASV 105	CAL	0.67	2.47E-03	1.91E-02	Bacteria	Chloroflexi	Dehalococcoidia	DscP2	NA	NA
ASV 24103	CAL	0.61	7.02E-03	4.98E-02	Bacteria	Chloroflexi	Dehalococcoidia	DscP2	NA	NA
ASV 14862	CAL	0.70	1.18E-03	9.58E-03	Bacteria	Chloroflexi	Dehalococcoidia	MSBL5	NA	NA
ASV 19987	CAL	0.65	3.29E-03	2.49E-02	Bacteria	Chloroflexi	Dehalococcoidia	MSBL5	NA	NA
ASV 522	CAL	0.65	3.62E-03	2.72E-02	Bacteria	Chloroflexi	Dehalococcoidia	MSBL5	NA	NA
ASV 10484	CAL	0.82	3.62E-05	3.67E-04	Bacteria	Epsilonbacteraeota	Campylobacteria	Campylobacterales	Sulfurovaceae	Sulfurovum
ASV 6587	CAL	0.62	6.46E-03	4.62E-02	Bacteria	Epsilonbacteraeota	Campylobacteria	Campylobacterales	Thiovulaceae	Sulfurimonas
ASV 26049	CAL	0.66	2.86E-03	2.19E-02	Bacteria	Firmicutes	Clostridia	Clostridia_Incertae_Sedis	Unknown_Family	Candidatus_Desulforudis
ASV 31233	CAL	0.62	5.90E-03	4.25E-02	Bacteria	Firmicutes	Clostridia	Clostridiales	Christensenellaceae	NA
ASV 26214	CAL	0.69	1.58E-03	1.26E-02	Bacteria	Firmicutes	Clostridia	NA	NA	NA
ASV 24530	CAL	0.63	5.00E-03	3.66E-02	Bacteria	Firmicutes	NA	NA	NA	NA
ASV 1017	CAL	0.79	8.38E-05	8.11E-04	Bacteria	NA	NA	NA	NA	NA
ASV 32546	CAL	0.68	1.76E-03	1.40E-02	Bacteria	NA	NA	NA	NA	NA
ASV 10851	CAL	0.68	2.02E-03	1.58E-02	Bacteria	NA	NA	NA	NA	NA
ASV 13090	CAL	0.68	2.05E-03	1.61E-02	Bacteria	NA	NA	NA	NA	NA
ASV 22650	CAL	0.67	2.14E-03	1.67E-02	Bacteria	NA	NA	NA	NA	NA
ASV 20990	CAL	0.67	2.34E-03	1.81E-02	Bacteria	NA	NA	NA	NA	NA
ASV 20333	CAL	0.65	3.33E-03	2.52E-02	Bacteria	NA	NA	NA	NA	NA
ASV 11904	CAL	0.64	4.33E-03	3.21E-02	Bacteria	NA	NA	NA	NA	NA
ASV 30323	CAL	0.63	5.19E-03	3.78E-02	Bacteria	NA	NA	NA	NA	NA
ASV 555	CAL	0.63	5.29E-03	3.85E-02	Bacteria	NA	NA	NA	NA	NA
ASV 19956	CAL	0.62	6.16E-03	4.42E-02	Bacteria	NA	NA	NA	NA	NA
ASV 20970	CAL	0.66	3.08E-03	2.34E-02	Bacteria	Omnitrophicaeota	NA	NA	NA	NA
ASV 32257	CAL	0.64	4.06E-03	3.02E-02	Bacteria	Patescibacteria	Parcubacteria	NA	NA	NA
ASV 8382	CAL	0.63	5.26E-03	3.83E-02	Bacteria	Patescibacteria	Parcubacteria	NA	NA	NA
ASV 17333	CAL	0.64	4.59E-03	3.37E-02	Bacteria	Planctomycetes	OM190	NA	NA	NA
ASV 19471	CAL	0.61	6.85E-03	4.87E-02	Bacteria	Planctomycetes	Planctomycetacia	Pirellulales	Pirellulaceae	Bythopirellula
ASV 6532	CAL	0.73	6.01E-04	5.13E-03	Bacteria	Planctomycetes	Planctomycetacia	Pirellulales	Pirellulaceae	Pir4_lineage
ASV 31941	CAL	0.62	6.33E-03	4.53E-02	Bacteria	Planctomycetes	Planctomycetacia	Planctomycetales	Gimesiaceae	NA
ASV 24669	CAL	0.67	2.42E-03	1.87E-02	Bacteria	Proteobacteria	Alphaproteobacteria	Caulobacterales	Hyphomonadaceae	Euryhalocaulis
ASV 21852	CAL	0.62	5.65E-03	4.09E-02	Bacteria	Proteobacteria	Alphaproteobacteria	NA	NA	NA
ASV 31393	CAL	0.77	2.05E-04	1.89E-03	Bacteria	Proteobacteria	Alphaproteobacteria	Parvibaculales	PS1_clade	NA
ASV 10683	CAL	0.64	3.87E-03	2.89E-02	Bacteria	Proteobacteria	Alphaproteobacteria	Parvibaculales	PS1_clade	NA
ASV 20932	CAL	0.68	1.76E-03	1.39E-02	Bacteria	Proteobacteria	Alphaproteobacteria	Rhizobiales	Hyphomicrobiaceae	Filomicrobium
ASV 18267	CAL	0.68	1.83E-03	1.45E-02	Bacteria	Proteobacteria	Alphaproteobacteria	Rhizobiales	Hyphomicrobiaceae	Filomicrobium
ASV 9631	CAL	0.64	4.53E-03	3.34E-02	Bacteria	Proteobacteria	Alphaproteobacteria	Rhizobiales	Hyphomicrobiaceae	Filomicrobium
ASV 18913	CAL	0.65	3.25E-03	2.46E-02	Bacteria	Proteobacteria	Alphaproteobacteria	Rhizobiales	NA	NA
ASV 31302	CAL	0.68	1.79E-03	1.41E-02	Bacteria	Proteobacteria	Alphaproteobacteria	Tistrellales	Geminicoccaceae	NA
ASV 28779	CAL	0.66	2.87E-03	2.19E-02	Bacteria	Proteobacteria	Deltaproteobacteria	Desulfobacterales	Desulfobacteraceae	NA
ASV 26422	CAL	0.77	1.60E-04	1.49E-03	Bacteria	Proteobacteria	Deltaproteobacteria	Desulfobacterales	Desulfobulbaceae	Desulfurivibrio
ASV 24164	CAL	0.74	4.17E-04	3.66E-03	Bacteria	Proteobacteria	Deltaproteobacteria	Myxococcales	Haliangiaceae	Haliangium
ASV 21756	CAL	0.64	4.21E-03	3.12E-02	Bacteria	Proteobacteria	Deltaproteobacteria	NB1-j	NA	NA
ASV 29412	CAL	0.62	5.84E-03	4.22E-02	Bacteria	Proteobacteria	Gammaproteobacteria	Alteromonadales	Colwelliaceae	Colwellia
ASV 2287	CAL	0.74	4.96E-04	4.30E-03	Bacteria	Proteobacteria	Gammaproteobacteria	B2M28	NA	NA
ASV 15784	CAL	0.62	5.72E-03	4.13E-02	Bacteria	Proteobacteria	Gammaproteobacteria	B2M28	NA	NA
ASV 8249	CAL	0.62	5.94E-03	4.28E-02	Bacteria	Proteobacteria	Gammaproteobacteria	B2M28	NA	NA
ASV 7535	CAL	0.62	6.19E-03	4.44E-02	Bacteria	Proteobacteria	Gammaproteobacteria	B2M28	NA	NA
ASV 22415	CAL	0.65	3.47E-03	2.62E-02	Bacteria	Proteobacteria	Gammaproteobacteria	Ectothiorhodospirales	Ectothiorhodospiraceae	Thiogranum
ASV 18257	CAL	0.62	5.73E-03	4.14E-02	Bacteria	Proteobacteria	Gammaproteobacteria	NA	NA	NA
ASV 11555	CAL	0.66	2.71E-03	2.08E-02	Bacteria	Proteobacteria	Gammaproteobacteria	Steroidobacterales	Woeseiaceae	Woeseia

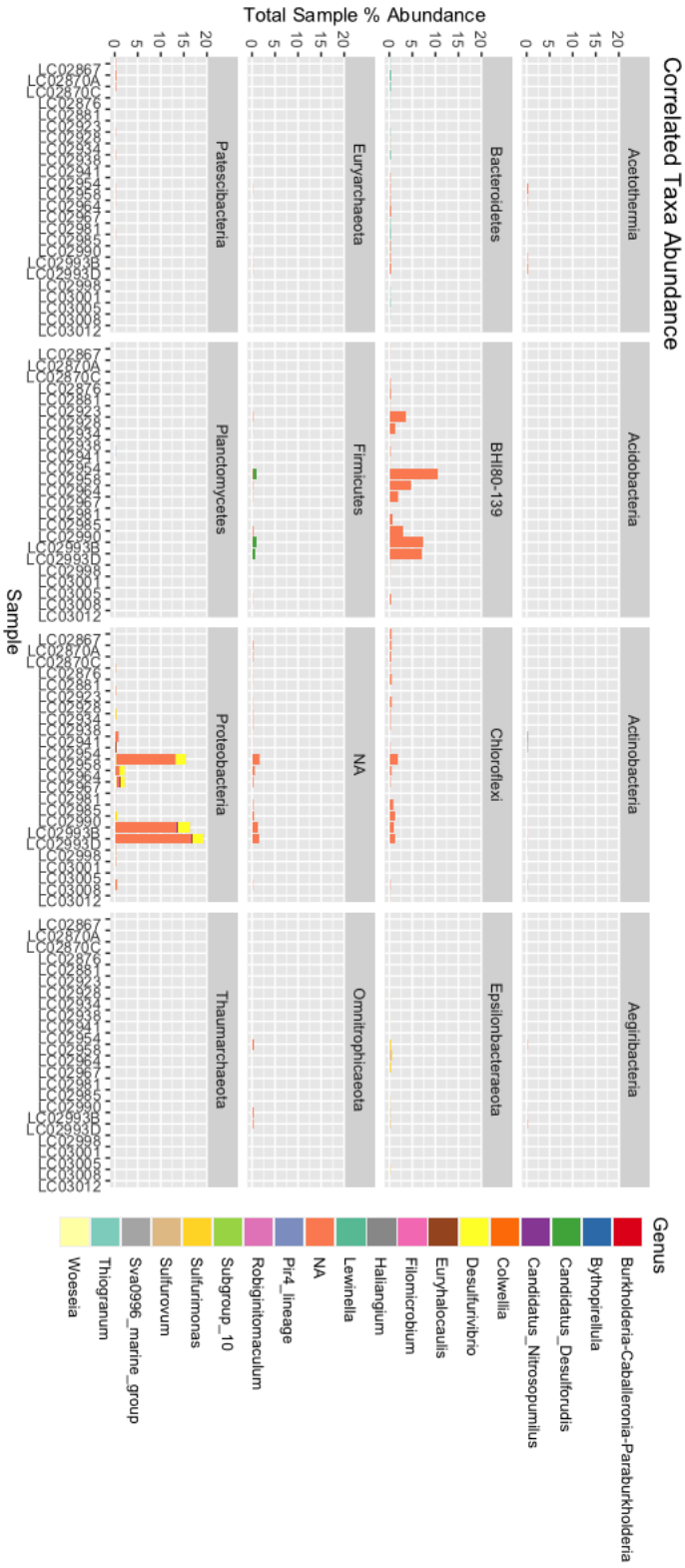

Figure A.1 - Stacked bar plot showing the abundance of ASV genera in each sample, faceted by their respective phyla. Some of the correlated ASVs constitute over 15% of the total sample reads, making them significantly abundant community members.

Table A.2 - An accounting of mineral and elemental concentrations through all CROMO cores as measured by ICP-MS.

Sample ID	Au	Ag	As	Ba	Be	Br	Co	Cr	Cs	Hf	Hg	Ir	Rb	Sb	Sc	Se	Sr	Ta	Th	U	V	W	Y	Zn	Zr	La	Ce	Nd	Sm	Eu	Tb	Yb	Lu	Bi	Cd	Cu	Mo	Ni	Pb
QV7	<1	1.7	1	17	<1	5.3	103	2680	<0.2	<0.2	<1	<1	<10	<0.1	6	<0.5	22	<0.3	<0.1	<0.1	29	<1	<1	40	4	0.43	3	<1	0.13	<0.2	<0.1	<0.05	<0.01	<2	<0.5	29	<2	2000	<5
QV18	4	<0.5	2	141	<1	0.8	132	2760	<0.2	<0.2	<1	<1	<10	<0.1	10.7	<0.5	225	<0.3	<0.1	<0.1	68	<1	3	45	5	1.73	5	<1	0.39	<0.2	<0.1	0.7	0.05	<2	<0.5	13	<2	2050	<5
QV18_2	5	<0.5	8	217	<1	<0.5	78.9	1550	<0.2	1.2	<1	<1	<10	0.1	11.9	<0.5	431	<0.3	1.6	<0.1	96	<1	7	63	39	4.43	10	<1	1.3	0.3	<0.1	0.91	0.1	<2	<0.5	38	<2	1200	<5
QV21	<1	<0.5	5	91	<1	0.9	102	2410	<0.2	<0.2	<1	<1	<10	<0.1	10.9	<0.5	118	<0.3	<0.1	0.2	54	<1	1	44	3	0.76	<1	<1	0.13	<0.2	<0.1	0.14	0.03	<2	<0.5	25	<2	1830	<5
QV25	<1	<0.5	11	299	1	<0.5	47.5	641	<0.2	1.6	<1	<1	<10	0.3	12.8	<0.5	687	<0.3	2.5	0.8	111	<1	10	67	69	7.56	16	11	2.2	0.2	<0.1	1.4	0.1	<2	<0.5	32	<2	691	<5
QV30	10	<0.5	18	399	2	<0.5	23.1	120	3	3.8	<1	<1	40	0.7	21.3	<0.5	257	<0.3	5.2	0.4	225	<1	21	129	118	17.1	43	10	4.67	1	<0.1	2.88	0.23	<2	<0.5	95	<2	78	9
QV30_2	45	<0.5	13	488	2	<0.5	30.4	137	9	3.9	<1	<1	100	0.6	18.6	<0.5	222	<0.3	6.9	2.3	218	<1	18	143	121	18.5	45	18	4.15	0.8	<0.1	2.81	0.28	<2	<0.5	97	<2	113	10
QV42	4	<0.5	6	15	<1	18.1	132	2520	<0.2	<0.2	<1	<1	<10	<0.1	6.03	<0.5	19	<0.3	<0.1	<0.1	19	<1	<1	35	<2	<0.05	<1	<1	<0.01	<0.2	<0.1	<0.05	<0.01	<2	<0.5	4	<2	2260	<5
CSW_1R	25	<0.5	11	386	1	1.1	25.3	356	2	3.8	<1	<1	60	0.9	15.6	<0.5	153	<0.3	3.8	1	131	<1	16	79	121	12.1	25	6	3.11	0.7	<0.1	2.18	0.19	<2	<0.5	49	<2	192	5
CSW_10R	6	<0.5	6	47	<1	<0.5	84.1	1630	<0.2	1.6	<1	<1	<10	<0.1	15.8	<0.5	129	<0.3	2	0.4	129	<1	11	71	46	5.19	13	<1	1.95	0.3	0.2	1.34	0.1	<2	<0.5	46	<2	1230	<5
CSW_10R_2	<1	<0.5	14	40	<1	<0.5	128	1520	<0.2	0.2	<1	<1	<10	<0.1	22.1	<0.5	133	<0.3	<0.1	<0.1	200	<1	7	57	18	0.97	5	<1	0.78	<0.2	<0.1	0.91	0.04	<2	<0.5	70	<2	2070	<5
CSW_14R	<1	<0.5	<1	28	<1	2.9	118	2220	3	<0.2	2	<1	<10	<0.1	10.3	<0.5	40	<0.3	<0.1	<0.1	44	<1	1	36	3	<0.05	<1	<1	0.13	<0.2	<0.1	<0.05	0.06	<2	<0.5	18	<2	1690	<5

Sample ID	Tom Description	SiO2 wt%	Al2O3 wt%	Fe2O3(T) wt%	MnO wt%	MgO wt%	CaO wt%	Na2O wt%	K2O wt%	TiO2 wt%	P2O5 wt%	Cr2O3 wt%	S wt%	LOI wt%	Total wt%	
QV7	Pure serpentine	39.6	0.8	7.31	0.091	37.81	0.13	0.05	0.03	0.028	0.01	0.268	0.085	13.87	99.72	Serpentine
QV18	Mostly saponite (?), trace clinochlore (?), no serp	41.7	2.97	7.42	0.172	32.39	1.14	0.48	0.02	0.072	0.01	0.276	0.103	13.56	99.94	Saponite (?),
		41.08	6.6	8.48	0.154	25.49	1.81	1.18	0.12	0.34	0.09	0.155	0.069	14.14	99.48	Saponite (?),
QV21	Nearly pure serpentine, minor unknown (saponite?)	39.91	2.29	7.97	0.156	32.93	1.46	0.23	0.03	0.058	<0.01	0.241	0.072	14.29	99.32	Serpentine, n
QV25	Mostly saponite (?), trace clinochlore (?), no serp	42.21	8.06	7.74	0.134	20.2	2.5	2.04	0.15	0.41	0.12	0.0641	0.062	15.69	99.25	Need to chec
QV30	Quartz, albite, trace unknown phyllosilicates	56.38	15.95	8.09	0.14	4.69	1.96	3.89	2.49	0.759	0.24	0.012	0.177	5.78	100.4	Quartz, albit
		56.28	15.7	7.27	0.141	3.6	1.67	3.09	3.28	0.719	0.2	0.0137	0.225	6.45	98.39	Quartz, albit
QV42	Pure serpentine	39.35	0.43	6.23	0.082	38.93	0.07	0.05	<0.01	0.005	<0.01	0.252	0.012	14.3	99.47	Serpentine
CSW_1R	Mostly quartz, minor albite, unknown phyllosilicate, trace serp	63.28	12.83	6.19	0.048	3.26	1.61	2.03	1.13	0.585	0.05	0.0356	0.031	9.03	100	Mostly quartz
CSW_10R	Unknown phyllosilicate_2, chlorite	43.78	6.89	8.49	0.144	25.36	4.59	0.71	0.02	0.408	0.09	0.163	0.04	10	100.5	Unknown Phy
		42.46	7.25	9.41	0.127	23.97	5.06	0.87	0.03	0.453	0.03	0.152	0.145	10.58	100.2	Unknown Phy
CSW_14R	Pure serpentine	40.65	1.74	7.67	0.096	36.36	0.21	0.13	0.02	0.032	<0.01	0.222	0.626	13.08	99.99	Serpentine

Table A.3 – An accounting of CROMO well fluid measurements, focusing on Cr and Ni concentrations and relative well depth and characteristic information.

Well	Well_Cluster	Depth_Cluster	Well_Depth_m	Temp	pH	Cond_mS	DO_mgL	ORP_mV	DIC_uM	Cr_ppb	Ni_ppb	HS_um
CSW1.1	CSW	Medium	19.5	16.28	12.07	3.807	0.16	-279.5	654.65	130	526	3.54
CSW1.2	CSW	Shallow	19.2	16.32	8.72	4.603	0.41	-124	1513.54	16.3	95.3	8.5
CSW1.3	CSW	Medium	23.2	14.73	10.47	4.615	0.13	-286.4	121.68	17.2	132	4.2
CSW1.4	CSW	Shallow	8.8	19.3	7.71	1.988	2.74	181.3	4564.11	133	546	<1.0
CSW1.5	CSW	Deep	27.4	16.04	9.78	4.777	0.42	-202.7	505.58	18.9	79.5	1.41
CSWold	CSW	Deep	76.2	17.7	9.61	11.001	0.98	-165.4	54.55	139	589	<1.0
N08A	N08	Deep	39.6	16.45	10.82	5.891	0.23	-218.2	35.33	138	629	3.7
N08B	N08	Medium	26.2	18.04	10.19	3.047	0.15	-117.5	89.90	20.8	79.8	<1.0
N08C	N08	Shallow	13.7	16.12	7.22	1.388	0.11	30.7	1129.57	128	567	<1.0
QV1.1	QV	Medium	23	16.67	11.44	3.378	0.15	-203.9	57.01	16.7	154	<1.0
QV1.2	QV	Shallow	14.9	16.88	9.31	3.002	0.22	-149.5	804.16	364	533	<1.0
QV1.3	QV	Deep	34.6	16.37	9.79	4.759	0.22	-208.7	210.81	131	542	<1.0

Table A.4- Counts of relevant metal responsive genes in all wells in CROMO, in addition to the MAG(s) of interest where they have been detected.

Kegg ID	Gene	Description	MAG Detected	SCRO0823	SCRO0822	SCRO4924	SCRO4919	CR12Mar_GSW14AB	SCRO4914	SCRO4915	SCRO4916	CR12Aug_GSW13AC	CR11L_GSW11 NovA	CR12Aug_GSW13A	CR11Aug_GSWVolI	CR12Aug_MCo	CR12Aug_QV12A	CR12Aug_QV11A	CR12Oct_QV11A	CR12Jun_QV11	CR11J_08_AugC
K15726	czcA/cusA/cnrA	heavy metal efflux system	-	1.82	3.14	2.33	7.66	10.49	1.23	4.47	0.55	0.00	0.50	6.86	9.73	1.37	1.66	0.34	0.00	0.10	26.97
K15727	czcB/cusB/cnrB	heavy metal efflux system	Serpentinomonas	0.42	1.15	1.46	2.92	432.17	0.99	0.70	0.24	1.64	23.19	252.29	202.22	220.36	346.61	380.72	264.81	278.00	195.96
K15725	czcC/cusC/cnrC	heavy metal efflux system	Serpentinomonas	44.53	40.12	37.45	29.56	173.00	44.73	52.68	28.97	252.89	383.45	248.00	209.21	183.97	74.70	194.68	259.48	267.56	371.47
K15264	czcD/cusD/cnrD	heavy metal efflux system	Serpentinomonas	0.89	1.46	0.52	4.79	0.94	0.78	1.16	1.57	0.33	0.16	24.38	89.15	134.61	2.51	72.18	128.41	118.64	29.57
K07793	nreB/nreB	putative Ni resistance protein	Tuerpetra	95.94	94.63	19.53	60.87	0.00	38.82	81.59	10.07	21.17	0.00	22.19	2.58	0.00	5.52	71.51	96.43	11.54	164.12
K19264	cbiK	prokaryotic cobalt chelation and cobalamin	-	nd	nd	nd	nd	158.22	nd	nd	nd	151.98	137.69	163.16	193.66	157.04	161.92	71.51	94.49	94.49	164.12
K19915	cbiL	prokaryotic cobalt chelation and cobalamin	some Desthiobacter	nd	nd	nd	nd	0.00	nd	nd	nd	0.00	0.00	0.00	3.24	1.55	4.15	0.00	0.00	0.00	4.08
K02009	cbiN	CoalNi transport protein	some Desthiobacter	0.00	0.28	0.00	0.00	2.45	0.00	0.00	0.26	0.58	0.00	166.71	0.15	0.17	5.29	0.22	0.09	0.08	0.00
K19564	nikA/cntA	Ni potential driven transporter	some Desthiobacter	0.11	1.21	1.61	0.00	233.80	2.45	3.84	6.69	1209.27	387.14	442.54	286.42	189.89	625.79	620.19	659.51	708.86	0.00
K09899	hlyC	Mg/Co exporter	ALL	314.25	293.36	282.33	317.84	4.48	296.51	288.52	283.61	1.47	0.00	4.03	22.07	0.00	1.03	33.97	49.20	45.85	32.29
K02059	ABC.FE.S	Ni-peptide transporter system, substrate binding protein	ALL	1873.42	1279.86	733.29	1372.62	6.21	1409.24	1648.21	1658.71	0.00	0.00	0.00	58.40	18.57	68.40	25.26	7.39	22.60	46.27
K07241	hoaN/nikA	Ni/Co transporter family protein	-	nd	nd	nd	nd	28.19	nd	nd	nd	1.42	37.66	131.18	136.60	19.28	4.29	42.76	40.09	39.45	46.27
K08970	rcnA	Ni/Co potential cornbinet transporter	-	0.00	0.08	0.00	0.60	0.00	0.00	0.00	0.00	0.00	0.00	0.00	0.00	0.00	0.00	0.00	0.00	0.00	0.00
K07240	cntA	chromate transporter	ALL	515.07	494.60	483.41	523.27	151.40	481.54	460.65	448.91	385.83	357.91	730.76	383.77	76.96	245.70	536.69	514.67	531.19	281.80

Kegg ID	Gene	Description	MAG Detection	CR12Mar_QV11C	CR12Aug_QV11C	CR12Aug_QV11A	CR12Mar_Blab	CR11_08_AugCR11Jul_QV11_08_Aug	CR12Aug_QV12A	CR12Aug_SA	CSWVolJ_Dec13_uni	QV12_Aug13_uni	QV12_Dec13_uni	QV11_Aug13_uni	QV11_Mar13_uni	N08B_Dec13_uni	N08B_Aug13_uni	N08B_Mar13_uni
K15726	czcA/cusA/cnrA	heavy metal efflux system	-	0.10	6.09	17.76	41.36	95.37	12.84	0.82	0.98	4.65	2.94	0.00	0.00	1.93	0.00	0.00	0.00	0.00	0.00
K15727	czcB/cusB/cnrB	heavy metal efflux system	Serpentinomonas	268.95	61.14	502.15	184.97	142.62	144.46	56.89	132.30	213.10	47.98	156.46	162.35	84.68	46.26	225.31	97.41	0.00	0.00
K15725	czcC/cusC/cnrC	heavy metal efflux system	Serpentinomonas	296.43	192.46	255.27	286.18	262.95	263.31	301.15	183.99	226.22	173.11	101.14	103.86	35.21	66.32	13.43	94.66	81.75	7.36
K15264	czcD/cusD/cnrD	heavy metal efflux system	Serpentinomonas	87.71	11.65	9.33	18.63	9.43	11.26	20.51	23.50	61.64	6.66	2.20	0.79	85.98	0.00	0.55	0.00	7.36	7.36
K07793	nreB/nreB	putative Ni resistance protein	Tuerpetra	0.00	19.70	5.19	6.50	3.51	5.39	9.73	0.30	8.69	1.98	140.70	0.43	0.00	8.53	36.54	2.17	1.93	1.93
K19264	cbiK	prokaryotic cobalt chelation and cobalamin	-	60.82	133.50	21.70	23.57	23.23	20.68	11.27	18.69	259.59	25.79	151.11	11.58	10.97	6.84	64.52	15.97	15.54	15.54
K19915	cbiL	prokaryotic cobalt chelation and cobalamin	some Desthiobacter	0.00	1.50	0.46	0.57	0.00	0.10	0.24	1.66	0.90	0.00	0.00	1.00	0.00	0.00	0.80	0.00	0.00	0.00
K02009	cbiN	CoalNi transport protein	some Desthiobacter	0.08	1.18	3.01	0.11	5.30	0.19	0.11	0.00	1.44	0.00	11.75	7.23	0.00	181.00	0.00	8.25	8.20	8.20
K19564	nikA/cntA	Ni potential driven transporter	some Desthiobacter	703.01	748.24	384.61	576.71	479.71	582.58	594.00	294.00	182.92	386.36	78.89	114.32	82.56	113.49	112.04	185.86	116.99	116.99
K09899	hlyC	Mg/Co exporter	ALL	31.86	13.91	13.16	73.52	54.91	48.16	99.12	24.09	23.41	74.97	0.85	6.06	6.62	0.00	5.32	19.76	7.98	7.98
K02035	ABC.FE.S	Ni-peptide transporter system, substrate binding protein	ALL	4.14	0.92	8.62	1.30	15.14	4.96	2.96	1.84	29.42	5.66	3.41	0.37	0.00	0.00	0.00	0.00	1.22	1.22
K07241	hoaN/nikA	Ni/Co transporter family protein	-	42.57	17.73	45.97	13.60	5.15	7.38	15.69	23.07	4.79	0.00	3.53	0.12	0.59	0.00	10.05	0.00	23.12	0.00
K08970	rcnA	Ni/Co potential cornbinet transporter	-	0.00	0.00	0.00	0.61	0.00	0.38	0.72	0.00	0.00	0.00	0.00	0.00	0.00	0.00	0.00	0.00	0.00	0.00
K07240	cntA	chromate transporter	ALL	519.12	277.39	231.82	374.62	383.66	482.84	472.56	129.20	242.36	33.56	64.01	56.63	276.27	239.41	27.11	12.18	78.98	78.98